The forced vibrations of a cylinder at low Reynolds number flow, an investigation of the non-lock-in and lock-in regions

Konstantinos Angelopoulos

A thesis submitted in partial fulfilment of the requirements
for the degree of Doctor of Philosophy to:
College of Engineering, Design and Physical Sciences Brunel University

Thesis Supervisors

Prof. Hamid Bahai

Dr Jan Wissink

This work is dedicated to my family who supported me by all means.

My father Prof. Angelos Angelopoulos

My mother Adamantia Angelopoulou

My brother Dimitrios Angelopoulos

Abstract

The present thesis is examining the forced vibrations of a circular cylinder in the low Reynolds number flow of 200. A numerical study is performed that employs an already existing algorithm developed by (Breuer 1998) and enhanced with the characteristic of the cylinder's motion by (MadaniKermani 2014) who employed the moving frame of reference method of (L. Li, Sherwin et al. 2002).

The algorithm was extensively assessed for the benchmark studies of flow around a stationary circular cylinder. A new observation was made on the effect of the aspect ratio of the computational cells in the mid region of the wake. The studies so far are emphasizing on the characteristic of a dense mesh, with a small aspect ratio, in the high divergence areas in the near region of the cylinder surface, neglecting the effect of the regions away from the surface. The present study on a stationary circular cylinder flow, proved that the aspect ratio of the distant cells has a significant effect on the St number and the force coefficients.

The main study of the thesis emphasizes on the lock-in region where the wake oscillates in unison with the harmonic motion of the cylinder. The study makes a new observation on the qualitative and quantitative description of the lock-in conditions. In particular, it reveals two regions of resonance and non-resonance lock-in. Despite the fact that the lock-in is achieved, when the frequency ratio is in the first part of the region away from the unity ratio, the forces are not greatly magnified. As the ratio approaches the unity the forces experience a resonance that reaches the highest value after the unity.

Furthermore, the adaptation time of the flow to the motion of the cylinder is examined and extends the results of (Anagnostopoulos 2000) to the full extent of the lock-in and the non-lock-in regions. More precisely the flow strives to reach a steady state when it is in the lock-in region rather in the non-lock in cases it reaches the steady state faster. It is postulated that the adaptation time depends on both the numerical and the physical adaptation.

Moreover, the force coefficients characteristic of sinusoidal behaviour in the lock-in region is attempted to be approximated by a Newton polynomial that is built by making use of the divided differences method. The amplitude of the forces is approximated by a third degree Netwon polynomial built from the results of the present thesis simulations. The use of an approximation is providing faster results ignoring the need for a full resolution of the Navier-Stokes equation.

Acknowledgements

The present study has been performed the last 7 years encountering several difficulties (mainly computational resources) but also gaining a lot of knowledge. The cooperation with my supervisors Prof Hamid Bahai and Dr Jan Wissink has been crucial for my studies. They allowed me to work on my own and research on a variety of topics without any constraints; when I was derailed and lost in the sea of knowledge, they were offering their experience with very accurate and essential comments, guiding me to the completion of the present thesis.

A major part of this research has been conducted in the parallel processing system (Hellas Grid) back in my country. Dr Dimitris Dellis with a benevolent selfless gesture offered help when everything was doomed to fail due to lack of computational resources. He offered his expertise and made things possible for the simulations.

Very special thanks to my colleague Dr SeyedHossein Madanikermani who offered his knowledge on CFD and coding capabilities to help me finalise the thesis, things would have been different without his kind and crucial intervention.

Finally, I would like to thank Dr Jeremy Daniel, who we did not listen when he was giving us the warnings on the computational capabilities of the parallel system. Dr Daniel exhausted all his expertise and time, fighting with us to run the simulations and supported us in acquiring a new parallel system.

Contents

List of Symbols

The presentation is in alphabetical order following the first column.

Symbol	Representation	Dimension	SI Unit	Description
a	acceleration	$\frac{L}{T^2}$	$\frac{m}{s^2}$	acceleration
A	number	-	-	Stretch factor
A_e	Amplitude	L	m	Excitation amplitude, ViV, FoV
A_L	Amplitude	L	m	Lift force amplitude
A_r	Ratio	-	dimensionless	Excitation Amplitude/diameter
A_{CL}	Amplitude	L	m	amplitude of lift coefficient
A_{CD}	Amplitude	L	m	amplitude of drag coefficient
B_r	Ratio	-	dimensionless	Fluid Domain width /diameter
C	Coefficient		dimensionless	Structural Damping
C_P	Coefficient		dimensionless	Pressure
C_{bp}	Coefficient		dimensionless	Base Pressure
C_L	Coefficient		dimensionless	Lift force
C_D	Coefficient		dimensionless	Drag force
C_{Lrms}	Coefficient		dimensionless	Round mean squared values of lift coefficient
$\bar{C_D}$	Coefficient			Mean drag coefficient
C_E	Coefficient			Energy exchange between cylinder and fluid
$C_{L1,L2,\ldots,Lk}$	Coefficient			Fourier coefficients of the lift force
t	Time	T	s	Natural or computational time
D	Length	L	m	Cylinder's diameter
d_f	Length	L	m	wake width
d_V	Length	L	m	alternate row vortices distance
d_{V_c}	Length			

F	Force	$\frac{ML}{T^2}$	N	Force
F_D	Force	$\frac{ML}{T^2}$	N	Fluid Drag force
F_L	Force	$\frac{ML}{T^2}$	N	Fluid Lift force
f_{CL}	frequency	$\frac{1}{T}$	$\frac{1}{S}$	Frequency of lift coefficient
f_{CD}	frequency	$\frac{1}{T}$	$\frac{1}{S}$	Frequency of drag coefficient
F_{Dp}	Force	$\frac{ML}{T^2}$	N	Pressure drag force
F_{Lp}	Force	$\frac{ML}{T^2}$	N	Pressure lift force
F_{Df}	Force	$\frac{ML}{T^2}$	N	Friction drag force
F_{Lf}				Friction lift force
f_n	Frequency	$\frac{1}{T}$	$\frac{1}{S}$	Structural eigen-frequency also referred as natural frequency
f_r	Ratio			Frequency ratio $\frac{f_e}{f_{vs}}$
f_e	Frequency			Excitation frequency ViV, FoV
f_{vs}	Frequency			Vortex shedding frequency $\neq St$
$grad\varphi$	Operator			Gradient of a scalar field
H	Length	L	m	Width of the computational flow domain
k	Constant			Spring constant
K	Circulation			Fluid circulation
L	Length	L	m	Cylinder's span-wise length
L_r	ratio	-	dimensionless	Wavelength ratio
λ_e	length	L	m	wavelength
l_f	Length	L	m	Vortex formation length
l_V	Length	L		Same row vortices distance
l_b	Length			closed wake vesicle
m	Mass	M	kg	mass
m_a	Mass	M	kg	Fluid added mass
m^*	Ratio		dimensionless	Mass ratio ViV, FoV
p	Force	$\frac{M}{LT^2}$	N	fluid pressure
P_∞	Force	$\frac{M}{LT^2}$	Pascal	Fluid pressure at a point in the far field

P_θ	Force	$\frac{M}{LT^2}$	Pascal	Fluid pressure at a point on the surface of the cylinder
Re	Reynolds number		dimensionless	$\frac{\text{Inertia force}}{\text{viscous force}}$
r_a	ratio	-	-	Aspect ratio of a control volume
St	Strouhal number		dimensionless	Strouhal number
St^*	parameter		dimensionless	Synchronized wake parameter
T_a	period	T	s	Transition period
T_e	period	T	s	Wave period
V_f	Velocity	$\frac{L}{T}$	$\frac{m}{s}$	local flow velocity
V_∞	Velocity	$\frac{L}{T}$	$\frac{m}{s}$	Undisturbed or free flow velocity
V_{def}	velocity	$\frac{L}{T}$	$\frac{m}{s}$	The deficit between wake and free flow inline velocity
V_r	Ratio		dimensionless	Reduced velocity
v_i	Vector component	$-$	$-$	Fluid velocity vector component
V_e	Velocity	$\frac{L}{T}$	$\frac{m}{s}$	Excitation velocity of the cylinder
v_i^*	Velocity	-	-	Normalized velocity
$\vec{V}(r,t)$	Vector field	3	$cardinality$	fluid velocity vector field
V_{CV}	Volume	L^3	m^3	Physical volume of the control volume
w_r	Ratio	$\frac{L}{L}$	dimensionless	Wake dimensions ratio
W_o	work	Joules	$N * m$	Work done by a force in one oscillation cycle
x_i	Length	L		Cartesian coordinates
x_{CV}	Length	L	m	Control volume dimension
y_{CV}	Length	L	m	Control volume dimension
Hellenic Symbols				
Δ_s	length	L	m	Surface cell radial length
θ	angle		Degrees/rads	clockwise angle between stagnation and a point on the surface of the cylinder
θ_S	angle	L	Degrees/rads	Separation point angle measured clockwise from the stagnation point
ν	viscosity	$\frac{M}{TL}$	$\frac{kg}{s \cdot m}$	Fluid viscosity

ρ	density	$\frac{M}{L^3}$	$\frac{kg}{m^3}$	Fluid density
τ	Friction			
Ω_{fluid}	set	Hausdorff 3	-	Fluid domain set
$\partial\Omega_{fluid}$	set boundary	Hausdorff 2	-	Fluid domain boundary
$\bar{\Omega}_{fluid}$	Closure of a set	Hausdorff 3	-	

List of Abbreviations

CFD	Computational Fluid Dynamics
ODE	Ordinary partial differential equation
FoV	Forced Vibrations
ViV	Vortex induced vibrations
CV	Control Volume
FFT	Fast Fourier Transform
FSI	Fluid Structure Interaction
r.m.s	root mean square

List of Figures

List of Tables

Introduction

It was known to ancient civilisations that sound can be produced by the wind blowing over a string. In 1878, Strouhal performed experiments concerning the Aeolian Tones produced by the vibrations of a wire in a wind flow. He showed that the frequency of the tones was proportional to the airflow velocity and the wire's diameter; his experimental studies concluded that when the frequency of the tone coincided with the wires natural frequency, the vibration's sound was greatly reinforced (Tsui 1982). Lord Rayleigh in 1879 investigated on the same topic with a violin string over a chimney draught (Rayleigh 1915); he observed that the vibration of the string due to the impact of the draught, was taking place in a plane perpendicular to the direction of the flow velocity. The studies of more than a hundred years ago, were already investigating the "*Fluid-Structure-Interaction*" phenomena that is the major topic of the present thesis and will be referred for the rest of the thesis with the acronym FSI. In 1908, Benard advanced the observations to a physical interpretation that exists since then and is the cornerstone to all the studies that followed in the field of hydrodynamics of flow around bluff bodies. Benard correlated the Aeolian tones with the formation of two parallel rows of equal spaced vortices in the wake of the cylinder (Tsui 1982). In 1911, Karman on the same field attempted to address the issue of the natural mechanism controlling the periodic vortex shedding and introduced his stability theory (Tsui 1982) that holds for low Re number laminar flows.

Structures liable to vibrations due to fluid flow are transmission lines (Barry, Zu et al. 2015), chimney stacks (Wong, Heathcock 1985), masts and towers (Koss, Melbourne 1995), suspension bridges (Keles 2015), pipelines (King 1977), oil platform columns(Blevins, Halkyard et al. 2001), bundles of cylinders (Liu, Feng et al. 2017) for nuclear power generation and in general various cylindrical or prism shaped structures. The prediction of vibrations of these structures is crucial for the benefit of the environment and the safety of the people working in such facilities.

In ocean engineering, cylindrical structures are used to link the well at the seabed to a floating platform or a ship. These structures have large aspect ratios, due to their length, making a full-scale numerical simulation a large and lengthy process. In real conditions, the structure is subjected to varying intensity flows or oscillatory wave flows that differ according to the depth and therefore along the length of the cylinder. The fatigue and the proper installation are the main concerns for a construction company that takes over such a work. Depending on the depth, supports and underwater stations may be used raising the cost and the complexity of the design. A mathematical model should engulf all the design factors, so it can be optimised and predict

properly the fatigue, satisfying the costs at the same time. So far, a full-scale structural model has not been numerically or experimentally studied, rather a partial study of sections, the interaction between specific structural components and the environment is performed to enhance the knowledge of such systems until computing power is high enough to overcome the magnitude of the size of the structure. The partial studies show totally different results than a full-scale study e.g. a long flexible cable has no resemblance in response with a short cylinder; nonetheless when a string is employed to represent a flexible cylinder the wake response, along the span of the cylinder presents similarities with the wake of a moving rigid short cylinder. The design of mechanical systems involving arrays of cylindrical structures, submerged stations and devices engulfs a plethora of issues; the paper of (Sengupta, Low et al. 2016) and references therein attempts to establish design criteria, parameters and strategies. As the structural analysis of a riser is not in the scope of this thesis, modelling of the structure will not be attempted; more information on the structural analysis and structural composition of a riser can be found in the thesis of Edmans(2013).

In the Figure 0-1 below, the common disturbances occurring in flows around cylindrical structures, that are also associated with the FSI phenomena, are presented.

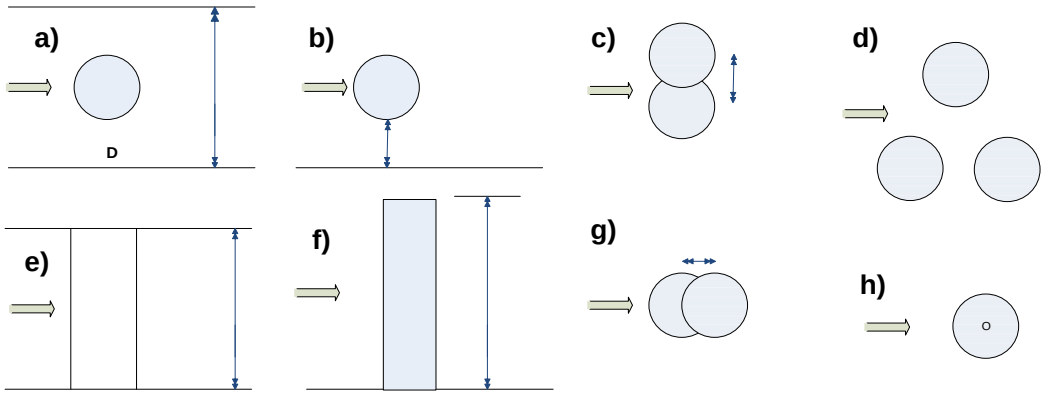

Figure 8-1 common disturbances of the flow field around a circular cylinder

Namely, these are a) the blockage effect, b) the wall proximity, c) the transverse motion of the cylinder, d) the existence of many bodies in the flow domain, e) the end conditions on the span wise direction, f) the cantilever case g) the inline motion of the cylinder, h) the axial span-wise motion; the present thesis investigates the case presented in the c) section of the Figure 0-1.

As conceptualised by Felippa, Park et al (2001), computational mechanics nowadays are concentrating on the "*three multis*"; namely the multiscale, the multi-physics and the multi-processing. Material models spanning a wide range of physical scales are the framework of multiscale simulations. The term multi-physics refers to the interaction of two or more physical

systems of different physical behaviour. Multiprocessing embodies the computational methods used to decompose and synchronise the different systems, so a unified model is constructed to simulate the behaviour of the overall system. The most common example of this "multi" discipline is the FSI. Applications in FSI, include scales from nanometres, as in micromachining (Ostasevicius, Jurenas et al. 2015), scales of automotive parts (Bathe, Zhang 2004), biomechanical systems e.g. heart valves (Mohammadi, Cartier et al. 2016), to scales of an aircraft (Goud, Kumar et al. 2014) or a bridge (Alfarra, Dinkler 2016).

Oil and gas industry shows great interest in the FSI phenomena mostly due to the use of long cylindrical structures that stretch to an ocean deep flow field. These structures being in a flow field form a wake; if vortex shedding is present then the structure is susceptible to vibrations due to the fluid forces caused by the vortex shedding, this phenomenon is named "Vortex Induced Vibration" and for the rest of the Thesis will be referred with the acronym ViV. The fatigue induced from the ViV phenomena can be dominant amongst the fatigue factors (Le Cunff, Biolley et al. 2002). If the analysis shows great ViV fatigue, then it is suggested that in the design process an Anti-ViV device should be utilised e.g. helical strakes on the span-wise direction of the cylinder. According to Le Cunff, Biolley et al (2002), three approaches are proposed to investigate numerically the FSI phenomena. In the first approach, the modal response of the structure to the vortex shedding is utilised to provide fast a lifetime estimate for the structure fatigue. In the second, the structural equation is resolved in time along with a fluid model, while the third approach is resolving the structural equation along with the full Navier Stokes equations.

In general, an FSI problem deals with the interaction of two mechanical systems, namely the fluid and the structure. So far, for each individual field various mathematical models have been developed and proved to represent accurately the physical properties of the material. A coupled system though is a system, where physically or computationally heterogeneous components interact dynamically; the interaction can be "*one-way*" if there is not any feedback or "*two-way*" if there is feedback between the individual systems (Felippa et al. 2001). The components are called physical when their mathematical model is described by field equations, such as in continuum theories of solids or fluids. (Felippa et al. 2001). The artificial components are usually the interfaces and the pseudo-representation of mechanical abilities that must be engulfed in the equations. The last components are created to allow the interaction between the substantially different physical fields, with data exchange, transfer or adaptation. The present thesis employs a pseudo-representation method where a component is added to the equations to represent the motion of the one of the two heterogenous systems.

As in a numerical solution of a single physical field, a two-field coupled system needs to be discretized in space and time; space partitioning can be algebraic or differential (Felippa et al.

2001). In the first case, the complete coupled system is spatially discretized first and then decomposed. In the second case the decomposition is performed first and each field is discretized separately. The time discretization depends on the method chosen for the FSI representation; to simulate a coupled system there are two fundamental approaches:

- **The monolithic or simultaneous treatment (direct).** The whole problem is treated as a monolithic entity and all components advance simultaneously in time.
- **The partitioned treatment (iterative).** The field models are computationally treated as isolated entities that are separately stepped in time.

For the FSI problems the following distinction can be made, as far as it concerns the nature of the problem, meaning the way the interaction occurs between the physical fields; if the structure is surrounded by the fluid field it is an exterior problem while in the opposite case, it is an interior problem (Le Tallec, Mouro 2001).

Furthermore, each modelling technique has a different way of treating the issues that arise during the numerical representation of an FSI problem. The mathematical model chosen for the description of the fluid behaviour plays the most decisive role in the approach of the FSI problem, as it is the most computationally expensive. Physically an FSI problem consists of the following stages

- The fluid applies loads on the structure
- The structure responds to the load with displacement of its boundaries
- The structural response changes the physical properties of the fluid near the structure

The transition to the numerical description of the problem leads to the following issues that should be considered. Initially, the fluid applies loads on the structure and numerically speaking the pressure loads must be transferred from the fluid mesh to the structural nodes. The nodes from a finite element description of the structure are traditionally less in number than those of a fluid numerical grid; consequently the boundaries between the domains do not coincide and gaps or overlaps may appear that create numerical discrepancies. The need of an interface is obligatory for the correct transfer of data between the two meshes, while an algorithm for the correct application of the loads to the equivalent structural nodes is necessary. For non-matching interfaces, to correctly exchange data, interpolation and projection algorithms should be used. General criteria for the correct data exchange algorithm can be summarised as follows (De Boer, Van Zuijlen et al. 2007);

- Global conservation of energy over the interface
- Global conservation of loads over the interface
- Accuracy

- Efficiency

If the data exchange is correct, the structure will deform and consequently this will disturb the fluid domain at the borders of the structure; the flow will adapt according to the structural response. A coupling method for an FSI problem mostly treats the two previous problems, namely the response of the structure and the flow adaptation. A useful review on the previous issues is given in the paper of (Degroote, Haelterman et al. 2010).

The systematic study of fluid loading on structures did not begin until the end of the 19th century. Following the Tay Bridge (Scotland) disaster in 1879, designers and engineers started refining their methods of estimating the wind loading and assessing its dynamic effect on the structures. The first phenomena involving cylindrical structures that physically occurred, not in an experimental controlled environment, were observed on transmission lines (Den Hartog 1932). Vibrations of the cables were caused by the Bernard-Karman street of vortices forming in the wake due to the wind flow. The flow induced vibrations of flexible cylinders have been experimentally investigated under two basic approaches; in the first approach, long wires have been towed in the sea and in the second short cylinders are allowed to vibrate or undergo forced vibrations (FoV) in a controlled flow environment of a flume or a wind tunnel. The periodic pressure distribution on the cylinder surface along with the shear stresses, naturally associated with the vortex shedding, exert fluctuating forces on the cylinder that will oscillate if it is not constrained. The first experiments conducted on the excitation phenomenon utilized the air as the fluid medium. In these experiments, only the transverse direction was affected, the absence of added mass due to very low air density did not affect the inline direction. The motion of the cylinder as a response to the flow was taking place on a perpendicular direction to the flow. Later, in water and oil experiments the fluctuating force exerted on the cylinder had components in both directions but as the transverse component was greater than the inline component by an order of magnitude(Naudascher 1987, Vandiver J.K., Jong J.-Y. 1987), the attention was concentrated mainly in the transverse direction. It was not until the 70s, when a disaster occurred on a sea pipeline due to inline vibrations (King, Prosser et al. 1973), that the systematic study of the longitudinal direction started taking place.

In the margins of ViV studies, FoV methods come into play offering an alternative methodology of examining the interaction i.e. ViV conditions can be replicated utilising FoV configurations. As it has been observed and will be explained through the literature review the phenomena appearing have been quantified to a degree and a reversed engineering methodology gives rise to the FoV studies and the one-way interaction of the cylinder's motion with the flow. It is concerned mainly with the topic of frequencies superimposed on the vortex shedding and the potential synchronicity between cylinder's motion and vortex shedding.

In the FSI studies due to the multidisciplinary nature of the problems encountered, there are many issues arising, making a categorization of methods a difficult task. It must be underlined that when an FSI problem is approached the traditional problems of numerical analysis already exist and now, due to the coupling process, new issues arise on top of the already existing ones.

The previous description of the first observations arising in numerical and mechanical studies introduce the reader to the general topic of the present thesis namely the FSI. The following chapter is initially referencing the basic studies of the flow around a stationary circular cylinder; the second part of the chapter presents a more detailed review of the phenomena and study methodologies appearing in the ViV and FoV studies. The third chapter briefly presents the main numerical methodologies employed for the solution of the flow field equations. The fifth chapter examines the results stemming from the numerical solution presented in the fourth chapter and attempts a comparison with previous studies. The sixth chapter presents the initial results of the FoV studies of the present thesis while the seventh chapter discusses and presents the new findings that add to the FoV studies.

1. Hydrodynamics of Flow around a Stationary Circular Cylinder

Figure 1-1 A Bernard-Karman vortex street (Van Dyke 1982)

When fluid flows around a bluff body, a region of disturbed flow is always formed. Despite the differences of fluid flows e.g. the flow medium, the shape of the immersed object and so on, similarities are observed in the fluid flow region at the rear part of the body, the wake. In the Figure 1-1 above, the wake region of the flow around a stationary circular cylinder is depicted; the cylinder's shape is preferred for the present thesis studies. According to Roshko's experiments (1954) with different shaped objects, the wakes of different bluff bodies are similar in structure; past studies have concluded that the characteristics of a flow can be expressed through relations between quantities such as Reynolds, Strouhal and many other dimensionless numbers depending on the phenomena studied in each case. Briefly, the flow evolution around a circular cylinder largely if not solely, depends on the phenomenon of flow separation. The separation attributes to the flow a multiple of fluid dynamics phenomena with the most distinctive being the vorticity, Figure 1-1, and turbulence.

The present chapter, that it is the first part of the literature review, is concentrating on the Re number regime physical characteristics along with the description of variables and phenomena of the flow around a stationary circular cylinder. It is mandatory to clarify the basic characteristics of the fluid flow around a circular cylinder before the review proceeds to the FSI studies. The FSI phenomena distort the physical characteristics of the flow around a stationary cylinder, but as it will be revealed in the second part of the literature review, the physical mechanisms producing the phenomena remain identical for both moving and stationary cases.

1.1 A fundamental description of the flow around a stationary circular cylinder

Commencing a basic description of the fluid flow around a circular cylinder the Figure 1-2 below depicts the four disturbed regions of the fluid flow topology (Zdravkovich 1997). Briefly, the incoming flow is decelerating at the "*stagnation"* point thus creating a region of retarded flow upstream of the stagnation point. Consequently, the flow is bifurcating to two boundary layers attached to the upper and lower quarters at the back of the cylinder. Two regions of displaced and accelerated flow are formed at the near side regions of the cylinder. Eventually the boundary layers detach from the surface of the cylinder, forming the shear layers and one wide downstream region of separated flow, the wake. The wake starts from the separation point spreading between the shear layers and ending at the outlet of the flow domain.

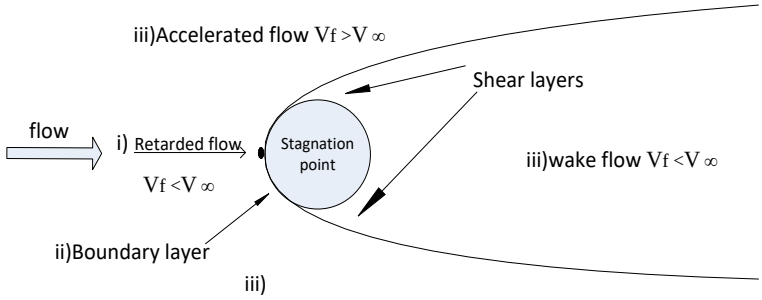

Figure 1-2 disturbed fluid flow regions around a circular cylinder, V_∞ is the free stream velocity, V_f is the local flow velocity

The flow around a circular cylinder can be laminar, transitional or turbulent depending on the flow instabilities and structures that develop in the aforementioned regions of Figure 1.2. The flow patterns develop as a successive spreading of vorticity from one region to the other, starting from the wake region and moving outwards to the shear layers and towards to the back of the cylinder in the boundary layers. The main parameter initially used to describe any state of flow with the characteristics of Figure 1-2, is the Reynolds number, a dimensionless number expressed as the ratio,

$$Re = \frac{DV_\infty}{\nu} \tag{1.1}$$

Where D is the diameter of the cylinder, V_∞ is the free flow velocity and ν the kinematic viscocity. The Re number is obtained through a non-dimensional analysis and can be considered as the ratio of inertial forces due to fluid motion and viscous forces due to the physical property of viscosity. The inertial forces are responsible for the convection of energy with motion, while the viscous forces are responsible for the diffusion of energy. The Re number can also be regarded as the ratio of the convection process to the diffusion process and as such provides a measure to quantify the mechanism of the hydrodynamics of the flow around a circular cylinder.

The value of Re for flow around a circular cylinder, ranges from less than one, up to one hundred for thin fibres in liquids, from a few hundreds to some thousands for wires and cables in wind, and from a few million for chimney stacks to hundreds of millions for cooling towers, space rockets and large geophysical flows. It must be stretched that the limits of the Re number regimes cannot be absolute and may differ from study to study; so when attempting a description, precision is sought for demonstration purposes only. Finally, the vastness of the studies and results makes impossible the full coverage of phenomena, although Zdravkovich (1997) attempted to gather all the available information in his books that are a valuable source of knowledge on the flow around cylinders.

1.2 Reynolds number flow regimes

For Re<5 there is no separation occurring, all the regions around the cylinder remain laminar. This region is also known as the “creeping flow” regime and it is dominated by the viscous forces. As Re number increases the magnitude of viscous forces decreases until separation occurs at the end of the range Re≅40. The separated shear layers coincide further downstream at the confluence point or free stagnation point; this point is located in the wake and not on the surface of the cylinder. A fixed pair of symmetric closed vortices of opposite sign attached to the cylinder appears in the near wake region between the shear layers, visually creating a vesicle (closed wake regime). Along the boundary of this closed region there is no flux of mass or convective motion; the pair of vortices is purely fed by diffusion with circulation coming from the separating boundary layer(Gerrard 1978). As the Re number increases, the length of the closed vesicle (or bubble) l_b, the transverse distance of the vortex centres $d_{V_c}$and the separation angle θ_S increase.

The closed cavity of vortices is the threshold of the flow phenomena appearing in the low Reynolds number regime and its decisive role is unfolded in the next paragraph.

As the Re number increases in the region of 30<Re<60 (periodic wake regime), Camichel, Dupin et al (1927) first observed the initiation of a near wake instability where a transverse oscillation of the closed vesicle trail occurs; when the l_b reaches a length close to 2D, it becomes unstable. It is observed that the trail instability does not affect the position of the stagnation or the separation point (Thom 1933). Secondary separations of the free shear layers occur along with the trail oscillation preventing the shear layers to meet at the confluence point; this also leads to the formation of the gathers in the shear layer area which are early flow formations of high divergence of velocity; the term *early* refers to the time before the vortex shedding where high divergence of the velocity usually occurs. The length of the vesicle starts decreasing as Re number increases (Gerrard 1978, Nishioka, Sato 1978) and a combination of fluid motions leads to vortex shedding; a more thorough description of the roll up and shedding of vortices was sketched by (Gerrard 1966) and will be briefly described in the next paragraph of the present chapter. Kovasznay (1949) concluded that for the region 40<Re<160, the vortex shedding is forming from this trail instability, so eddies appear further downstream rather than in the immediate region of the cylinder surface; this is a fundamental difference between low Re (up to ~150) and higher Reynolds number flows. Furthermore, the span-wise structure of the vortex street was under debate for many years. Kovasznay for Re=56 concluded that the laminar periodic wake is two dimensional. Roshko (1954) noticed that for Re=80, a slanted mode of the eddy filaments appears therefore the vortex shedding is a three-dimensional phenomenon. Philips (1956) postulates that in the range 40<Re<80 the wake is truly two dimensional while in the range of 80<Re<100 the wake is sensitive to disturbances and may become three dimensional. Many experiments were conducted with contradicting results until Berger and Wille (1972) suggested that, the slantwise shedding depends on the span-wise end-conditions effects. Slaouti and Gerrard (1981), similarly concluded that the three-dimensional effects strongly depend on the flow at each end of the cylinder. Williamson (1989), examined the effect of the end plates angle on the vortex shedding. and assigned the plate's angle a definite characteristic for the three-dimensionality of the phenomenon, the slanted mode disappears at a specific angle rendering the wake two dimensional. Williamson (1989) observed that the two modes, parallel and slantwise could not co-exist as they result from different boundary conditions. Turbulence does not appear in this Re region since vortices die out before becoming turbulent due to viscosity. Roshko (1954) classified the 40<Re<150 as the stable range due to the absence of turbulence while Ferguson (1965) employed the terminology *"incipient"* and *"pure"* Karman Range for the Re number regions 40 to 90 and 90 to 300 respectively.

For the region of 150<Re<400 (wake transition regime), the flow is characterized by the random initiation and growth of three dimensional irregularities which eventually lead to turbulence in the wake region. These irregularities randomly appear as distortions on the span-wise direction of the eddy filaments (Hama 1957, Gerrard 1978). Gerrard named the irregularities as "*fingers*" as they were pointing towards the cylinder and considered them as a typical feature of the transition into turbulence in the wake region. The "*fingers*" appear in the range 150<Re<160 and disappear in the range 300<Re<400. These flow structures sole do not produce a turbulent eddy; in the region 150< Re< 250 two main fluid motions contribute to the initiation of turbulence. Firstly, the vortices attract free stream laminar flow further downstream in the wake region. Secondly, the "*fingers"* add to the last interaction a disturbance that initiates irregularities at the outer isolines of the vortex filaments; therefore in this region the vortices have a laminar core and turbulent circumference (Bloor 1964, Bloor, Gerrard 1966), experimental proof in the paper (Cantwell, Coles 1983). On the contrary, for the 250< Re<400 region, entirely turbulent eddies are formed as transition into turbulence starts taking place in the separated shear layers that roll up thus forming fully irregular eddies.

In the Re region of 400<Re<1.1k a similar phenomenon to that of Re= 40 closed vesicle trail instability, marks the onset of transition into turbulence in the shear layer region (Lower Transition into Shear Layer regime). The wake axis symmetry and the in phase appearance of the two trail waves, one on each shear layer, reveal that their origin is not related to the vortex shedding but to the boundary layer and can be noticed as undulations of the free shear layers stemming from the separation points (Roshko 1954, Bloor 1964, Gerrard 1978). As Re number increases the period of the trail waves decreases and along with the pressure from the free stream flow causes the free shear layers to stabilise, postponing transition and elongating the formation region (Bloor 1964). In this range, as the vortices contain already turbulent fluid they diffuse fast (Roshko 1954)

For the 1.1k<Re<20k-40k (intermediate Transition to Shear Layers) regime a chain of small eddies is formed along the free shear layers which eventually roll up to a large two-dimensional irregular eddy which sheds downstream (Couregelongue 1929). Linke (1931) noticed a significant shortening of the formation region as the Re number increases in this region. The shortening is accompanied by a widening of the turbulent shear layers (Bloor, Gerrard 1966) and eventually, one motion counters the other leaving the vortex strength unaltered. In this range, the vortices travel further in the far wake where they break into smaller eddies rather than disintegrating in the near wake.

In the region 20k-40k<Re<100k-200k (upper Transition into Shear Layer) the length of the formation region stops decreasing at around Re=50k and the two-dimensional transitional eddies

disappear. The near wake is now highly three-dimensional since the free shear layers roll unevenly along the span of the cylinder and produce fully turbulent eddies (Zdravkovich 1997). The formation region is now of short constant length and produces a wide near wake that displaces the free shear layers accelerating the stream in the immediate region around the shear layers. The overall effect is postponing the spreading of turbulence in the shear layers. Main features of this regime are the modulation and out of phase variation of flow variables e.g. velocity fluctuations, Toebes (1968) postulates that only an average St frequency can be defined in this Re number region.

Increasing the Re number, in the region 100k-200k<Re<300k-340k (pre-critical regime) the stabilising effect caused by the shear layers diminishes. There is a gradual displacement of separation points downstream along with the Re number. The wake is getting narrower due to the free shear layers moving towards the wake central axis (Fage, Johansen 1928) The Strouhal number remains invariable; the distance between the shear layers gets shorter accompanied by an increase of the formation length which negates the narrowing effect and therefore the shedding frequency is not altered (P. Bearman 1969).

In the narrow region of 300k-340k<Re<380k-400k, the phenomenon where a single laminar separation bubble formed on the one side of the cylinder causing an asymmetric flow appears (single bubble regime). Eisner (1925) concluded that on the other side transition to turbulence occurs. The formation of the single bubble may take place on either side but when it is formed it does not change side (Eisner 1925). The single bubble existence affects the shear layers whose distance is reduced even more, causing a jump of the St to a higher value of 0.32. Relf and Simmons (1924)) noticed that the increase in the shedding frequency is accompanied by a decrease in the drag coefficient; the phenomenon of the jump of the Strouhal frequency accompanied by the decrease of the drag coefficient is also known as "*drag crisis*".

For higher Re in the region 380k-400k<Re<500k-1M, the asymmetric flow due to the single laminar bubble is disrupted by a second bubble formation at the opposite side of the cylinder. Bearman (1969), after the second separation bubble was formed, measured a well-defined periodic frequency signifying the re-establishment of vortex shedding and marking the end of the "*drag crisis*". For Re number up to 3.5M-6M (post critical), the vortex shedding ceases due to the highly three-dimensional transition of turbulence in the shear layers. Although, Roshko (1961), Cincotta et al (1966), Loiseau and Szechenyi (1974) and Schewe (1983) have noticed a re-appearance of vortex shedding at this range of high Re numbers.

Finally, the state of flow for 6M<Re is characterised by turbulence appearing in all the flow regions namely wake, shear and boundary layers. The transition starts moving upstream from the boundary layers towards the stagnation point. Roshko (1961) suggested that since all the flow

regions are fully turbulent it is unlikely that there will be any further transitions. Experimental applications are difficult and expensive for this range of Re numbers as high Reynolds numbers can be achieved by increasing the velocity of the free stream or the size of the cylinder; the latter is limited by the size of the tunnels and the former by compressibility and cavitation effects. Knowledge in this range is restricted to large scale observations of geophysical flows.

The present study is examining Reynolds numbers in the steady or periodic wake regime i.e. $40 \leq Re \leq 200$. In particular, the present algorithm is evaluated with the objective of reproducing the flow characteristics of the Re numbers equal to 80,100,120 and 200.

1.3 Vortex Shedding and the geometrical characteristics of the wake

When flow separation does not occur, the vorticity generated at the surface of the cylinder is confined to the thin layer immediately over the surface. The layer follows the cylinder contour and diffuses in the stream at the opposite of the stagnation point the confluence point; this is the general flow state for very low Reynolds numbers. At some point, separation occurs due to the backwards motion at the confluence point. Essentially, from the boundary layer theory, the friction on the cylinder's wall and the advent pressure at the rear side of the cylinder are the parameters responsible for the formation of vortices. Due to the friction forces on the wall of a bluff body, the fluid particles are decelerated forming a thin layer around the body, the boundary layer. The velocity of the fluid particles moving in the boundary layer varies from zero, in the immediate region above the wall, to the free flow velocity at the outer side of the layer. A particle moving in the boundary layer remains under the influence of the same pressure field as that of the outer layer; the friction forces consume the kinetic energy of the particles, that now cannot overcome the adverse pressure gradient at the downstream side of the cylinder's wall and eventually come to rest (Prandtl 1961). The adverse pressure forces the particle to move in the opposite direction obstructing the particles that follow. The particles accumulate and cause the thickening of the boundary layer; the reversed motion eventually causes the boundary layer to detach from the surface at the separation point, where the streamline intersects the wall at a definite angle. This yields the condition that the velocity gradient normal to the wall vanishes (Schlichting, Gersten 2003). The combination of the reversed motion with the separation is the origin of the vortex formation. Recalling from the Reynolds number regime description of the previous section, the closed vesicle that forms in the wake region at around Re=40, starts getting unstable; as the Re number increases the amplitude of the trail oscillation starts increasing while

the wavelength is decreasing; this action eventually leads to vortex shedding and is explained in the next paragraph.

The shedding mechanism is described by Gerrard (1966) in a simplified sketch, where one of the stationary vortices of the wake bubble elongates, its circulation attracts fluid from the shear layer of the opposite side that eventually cuts off the vorticity feeding of the vortex that sheds in the wake. Gerrard signifies that an important moment in the vortex shedding cycle, is when the concentration of vorticity in the near wake first splits into the portion that remains attached to the cylinder and the portion that is cut off and shed; the strength of the vortex is reduced by ten per cent after being shed (Fage, Johansen 1928). At very low Re number, the vortex shedding frequency is determined by how long time it takes for a vortex to develop and escape the influence of high shear stresses. As the Re number increases the viscous shear stresses decrease, making easier the slitting of the vorticity, reducing the formation time of the vortex and leading to a higher shedding frequency (Green, Gerrard 1993). Two modes of vortex shedding are observed, namely the low speed (Kovasznay 1949) and the high-speed mode(Gerrard 1966). In the former case, which prevails in the low Re number regimes, the formation is due to the wake bubble trail instability. In the latter case, turbulent eddies develop in a stationary position, much closer to the cylinder surface stemming from the shear layers (O. M. Griffin 1971). Roshko's measurements (1954) demonstrated that there is no smooth transition from low to high-speed mode. Williamson (1989) confirmed Roshko and revealed two discontinuities in the St-Re number relationship. The first discontinuity is around the Re number equal to 170 and the second in the region $225 < Re < 270$.

Furthermore, Karman's stability theory postulates that the lateral distance between the rows of the vortices d_V and the longitudinal spacing of the consecutive vortices l_V on the same row, are constants. This stability criterion is based on an inviscid fluid and does not actually hold for non-zero viscosity flow. Every vortex has a core of finite radius; its centre is the point of zero velocity, maximum vorticity and minimum local pressure. In experiment, the points of zero velocity maximum vorticity do not coincide; as the vortex is shedding the point of maximum vorticity remains unchanged in relation to the symmetry axis of the wake rather the point of zero velocity moves away (Schaefer, Eskinazi 1959, Roshko 1954). The Karman's criterion holds only for the region of the wake close to the cylinder; the distance ratio $w_r = \frac{d_v}{l_v}$, rapidly increases downstream due to the increase of $d_v$while $l_v$decreases very little. The distance from the rear side of the cylinder to the position of the centre of the vortex when it is shed, is the length of the formation region l_f and has been investigated by Green (1993). The end of the formation region is in the wake and has been described in studies in three ways,

- the point of the minimum mean pressure (O. M. Griffin 1971)
- the point with the maximum velocity fluctuation (Bloor, Gerrard 1966)
- the point where the transverse spacing of vortices is minimum and the point of maximum downstream velocity fluctuation (Schaefer, Eskinazi 1959, P. Bearman 1965)

A regular pattern of vortices which shed anti-symmetrically from each side of the cylinder with clockwise and counter-clockwise circulation, form the Karman-Benard vortex street. The vortex shedding frequency when non-dimensionalized with the V_f and the cylinder diameter D can be regarded as a function of Re number and is called the Strouhal number.

$$St = \frac{1}{Re} \tag{1.2}$$

The vortex shedding first appears around the Re number equal to 40 with the shedding frequency being approximately equal to 0.1. The St then gradually increases as Re number increases and at around Re=300 it obtains the value of 0.2 and throughout the subcritical regime it remains constant at this value. The St number experiences a sudden jump at Re equal to 3.5×10^5 and maintains a high value of around 0.5 for a large part of the supercritical region and then it decreases again for higher Re numbers. Lord Rayleigh first suggested that a frequency parameter could be expressed in terms of Taylor's expansion involving a viscosity parameter (C. Williamson, Brown 1998). Roshko developed a two-term truncated series relation between St and Re numbers for the range of Re number excluding the transition regime (Roshko (1954)),

$$St = 0.212\left(1 - \frac{21.2}{Re}\right), \text{for Re} < 180 \tag{1.3}$$

$$St = 0.212(1 - \frac{12.7}{Re}, \text{for } 300 < \text{Re} < 2000) \tag{1.4}$$

These approximations were widely used since then, while more recently Williamson and Brown proposed an expansion involving the square root of Re and a three-term truncated series (C. Williamson, Brown 1998)

$$\text{St} = 0.2731 - 1.1129/\sqrt{Re} + 0.4821/\text{Re} \tag{1.5}$$

A summary of similar to the equations (1.3-1.5) empirical functions which are more Reynolds number range specific, is presented is the Table (1-1) of the following page (Norberg 2003).

Further information on the formulas and the curve fits containing the Re number or the square root can be found in the paper of (Posdziech, Grundmann 2007).

Table 1-1Reynolds- Strouhal number relationship approximation functions (Norberg 2003)

Re number range	**St approximation function**
$47 - 190$	$0.2663 - 1.019/\sqrt{Re}$
$165 - 260$	$-0.089 + \frac{22.9}{Re} + 7.8 \times 10^{-4} \times Re$
$260 - 325$	0.2016
$325 - 1.6 \times 10^3$	$0.2139 - 4.0/Re$
$1.6 \times 10^3 - 1.5 \times 10^5$	$0.1853 + 0.0261 \times e^{-0.9 \times \log(\frac{Re}{1.6} \times 10^3)}$
$1.5 \times 10^5 - 3.4 \times 10^5$	$0.1848 + 8.6 \times 10^{-4} \times (\frac{Re}{1.5} \times 10^5)^{4.6}$

1.4 Hydrodynamic Forces

The flow around a cylinder will exert a resultant force produced by viscous friction along the surface of the cylinder and an unsymmetrical pressure distribution on the upstream and downstream side of the cylinder. The total force can be decomposed into two vector components namely the drag in the flow direction and the lift on the transverse to the flow direction. The fluid forces can be obtained by integrating the total stress around the surface of the cylinder. The total stress consists of two components the pressure and the friction. If p is the total pressure exerted on the cylinder surface and τ the friction or wall shear stress on the cylinder surface, then the inline force component or drag is,

$$F_D = \int_0^{2\pi} (p\ cos\theta\ + \tau\ sin\theta)\ r\ d\theta \tag{1.6}$$

The force component on the transverse to the flow direction the lift force is defined in the next page,

$$F_L = \int_0^{2\pi} (p\ sin\theta\ + \tau\ cos\theta)\ r\ d\theta \tag{1.7}$$

For the steady regime Re numbers, all the components are fluctuating at a steady frequency and constant amplitude(Bishop, Hassan 1964). When the symmetry of the low Re breaks ($Re \cong 40$), due to the trail instability, vortices start shedding downstream. The pressure distribution around the cylinder undergoes a periodic change in concert to the vortex shedding. According to the Gerrard's mechanism described earlier, when one of the vortices is shed, in the region that was occupied at the rear half side of the cylinder suction occurs until the next vortex is formed and shed. The lift force oscillates around a zero mean at the vortex shedding frequency. The drag oscillates around a non-zero mean at twice the vortex shedding frequency. The difference is due to the fact that, the vortices are shedding on the inline direction, therefore the alternate shedding of vortices has no effect on the drag force vector direction, as it does on the lift. The alternate shedding is changing the forces magnitude on the same direction with the drag force therefore the non-zero mean value as there is a vortex always forming on one side of the cylinder, while the fluctuation occurs at double the lift's frequency that changes around zero mean due to the symmetry of the alternate vortex shedding.

The observations of Cincotta, Jones et al (1966) and Schewe (1983) have shown that the lift force on a cylinder at rest exhibits a nearly perfect harmonic oscillator behaviour, it can be postulated that the lift force is the solution of the following linear harmonic motion equation (Berger 1988),

$$\ddot{F}_L + (2\pi\ St)^2 F_L = 0 \tag{1.8}$$

1.5 Summary

The present chapter is the first part of the literature review, The Reynolds number regime was described along with the flow characteristics. The fluid flow concepts namely the flow separation, the vortex formation and eventually the vortex shedding were described in detail. The St-Re number relationship was underlined as it provides a fundamental description in any attempt to quantify the flow around a circular cylinder. The vortex street in the stationary cases is the classic Benard-Karman street that is the most common flow structure for the low Reynolds numbers.

The aforementioned phenomena and characteristics of the fluid flow through the Re number range, have been integrated into one fundamental theory based on the studies and results of the flow around circular cylinders. Zdravkovich (1997) attempted to gather all the information in his books and it is recommended to any researcher to study these books before any attempt to study phenomena in this field.

The stationary cases variables and coefficients in the FSI cases undergo a change that follows a wake pattern that is altered due to the interaction. The St-Re relationship does not hold in the ViV and FoV cases as it will be described in the next chapter. Finally, the forces exerted on a circular cylinder and Berger's equation are of major interest; in the FSI studies the forces are following a model equation that ceases to be linear. The present thesis investigates the potential of a linear equation for the same description of the fluid force.

The second chapter of the literature review attempts to define a framework of the major FSI studies presenting the methodologies of reviewing the results, the effect on the flow patterns, forces and new relations between the parameters that appear. Many new phenomena occur due to the motion of the cylinder, although the fundamental concepts mentioned in the first part of the literature review retain their eventuality. It is now of great interest to obtain a similar theory on the flow description around a cylinder subjected to flow induced or forced vibration; Zdravkovich is continuing extending the assembly of studies to a third tome engulfing the FSI studies, that is not yet published. The following chapter presents a brief description of basic results and studies in FSI, ViV and FoV.

2 A Review of Studies in ViV and FoV

The motion of a freely or forced vibrating cylinder can lead to significant modifications of the wake flow geometry in comparison to the stationary case for a constant Re number. The St frequency continues to exist along with new frequencies that appear due to the motion or ceases to exist replaced by the vibration's frequency. The FSI investigates the relation between variables of the different components of the coupled system and attempts to model the combined behaviour of a cylinder responding to the fluid flow forces and in turn the wake's response to the motion induced. In the stationary cases, the cylinder is not but a wall boundary condition; in the moving cases, apart from being a dynamic boundary condition the boundary also carries energy that is exchanged with the fluid.

In a flow around a moving cylinder, the Reynolds number affects the system as it does in a stationary case, the viscous effects determine the vortex-shedding phenomenon. The ViV or FoV vortex-shedding phenomena are due to a mechanism identical to that of the stationary case phenomena i.e. the effect of the cylinder's motion on the splitting mechanism of the vortices, as described by Gerrard (1966), is responsible for any alterations in the flow patterns. Although , low Re numbers ViV exhibit a low cylinder response amplitude while the higher Re numbers show significantly higher response amplitude (Anagnostopoulos, Bearman 1992); the influence of Re number on FSI phenomena has also been demonstrated in the following papers of (Govardhan, Williamson 2006, Klamo, Leonard et al. 2005).

Physically, the motion of the cylinder does not allow for a similarity between flows of different mediums i.e. gas and fluid. Gabbai and Benaroya (2005) signify the difference between the natural frequency of the cylinder in the air and in the water medium. The latter includes added mass effects that change the natural frequency of the structure that do not exist in the air medium cases i.e. the ratio of the mass of fluid medium displaced m_a to the mass of the structure m is substantially greater in the water than in the air medium (P. W. Bearman 1984). Differences between the onset of ViV in the air and the water medium also appear due to the differences in the energy balance and transfer between the different mediums and the cylinder (King 1977). Wootton, Warner et al (1972) observed that different wake instabilities occur in the water and the

air medium. Bishop and Hassan(1964) also observed that the phase between the fluid force and the cylinder's motion in the air was different to that of the water medium case.

The interpretation and categorization of FSI phenomena is further complicated as Sarpkaya (2004) signifies the difference between the excitation and driving roles of an FSI phenomenon. An excitation phenomenon occurs even when the interaction mechanism between flow and the cylinder's motion is unclear but nonetheless the vortex shedding does excite the cylinder; the vortex shedding frequency is interrelated to the structural response or forced motion at all times (Bishop, Hassan 1964). The driving ability is obtained when the motion dictates the vortex shedding i.e. the wake oscillates in unison with the cylinder at a single frequency and the lock-in phenomenon occurs (Sarpkaya 2004).

Moreover, recalling from the stationary cylinder flow, it is the steady state that has to be achieved so any phenomena can be observed. In F.S.I. studies the terminology of steady state is more intricate. Steady state is achieved from the moment periodicity persistently appears in a fluid variable or coefficient's time-series. Sarpkaya's observation, mentioned in the previous paragraph, assists to define the periodicity of the steady state of an FSI phenomenon. In the exciting role, the vortex shedding naturally imposes a periodicity, the motion disrupts the vortex shedding and the steady state refers to the periodicity stemming from a combination of sinusoidal time series, while in the driving role, the steady state periodicity stems from a pure sinusoid time series due to the synchronisation of wake and cylinder's motion, that now oscillate in unison.

The description commences with the ViV studies and the transcendence to the FoV studies will follow in the second part of the presents chapter.

2.1 Initial observations of the ViV studies

Recalling from the introduction, the Aeolian vibrations of cables were the first phenomena observed and are due to the fluid forces exciting the structure. The vibrations are becoming more intense as the St frequency of the flow approaches the natural frequency of the structure f_n. The fluid-structure coupling can be characterized by the dimensionless number in equation (2.1) below, also known as the reduced velocity,

$$V_r = \frac{V_\infty}{f_n D_C} \tag{2.1}$$

where V_∞ is the undisturbed free flow velocity, f_n the eigenfrequency of the structure and D_C the cylinder's diameter. In effect, the V_r is the velocity when the vibrations due to the flow start taking place (Scruton, Flint 1964).The lock-in phenomenon occurs when f_n and St are close as values that corresponds to the equation (2.2) below

$$V_r = \frac{1}{St} \tag{2.2}$$

Apart from the lock-in condition of equation (2.2) it has been observed that for V_r values less than 10 there is a strong interaction between the cylinder and the near wake. In experiments, at the initiation of the cylinder vibration, when the wind speed is such so the vortex shedding frequency is different than the cylinder's natural frequency, both the cylinders amplitude and the amplitude of the fluctuating pressure exerted on the surface of the cylinder experience a beat phenomenon (Ferguson 1965, Ferguson, Parkinson 1967, Feng 1968, Bishop, Hassan 1964). The frequency of the beating component is roughly the difference between the fluctuating pressure frequency and the oscillation frequency; the phenomenon is due to the co-existence of the two different frequencies and it can be regarded as a constant effort of the vortex frequency to catch up with the cylinder's oscillation frequency (Feng 1968). At this stage, the amplitude of the fluctuating pressure has similar magnitude to the stationary case. As the wind increases, a range of frequencies is detected for which the vortex shedding frequency is captured by the cylinder's oscillation frequency, the beat pattern disappears; at this stage the maximum amplitude of ViV oscillation occurs and the amplitude of the fluctuating pressure is almost doubled (Ferguson 1965, Ferguson, Parkinson 1967, Feng 1968). Further increase of the wind speed, as it approaches the value for which lock-in occurs in the middle of the frequency range where the equation (2.2) holds, before the actual resonant speed, the pressure amplitude reduces abruptly almost to one third of the previous value when the beating disappears (Ferguson 1965, Ferguson, Parkinson 1967, Feng 1968). The range of frequencies that the beat stops and the force amplitude increases is the resonance region. The resonance region is called lock-in in FSI as not only resonant phenomena occur but the total system of the fluid and the structure acts in resonance locked in one frequency. The lock-in region can be described by non-dimensionalized parameters that consist of variables from both the structural and the fluid system, the most common will be referenced later on in paragraph 2.1.3.

Moreover, emphasizing on the characteristics of the induced motion of a freely oscillating rigid body, an empirical relationship that holds for different Re and structural characteristics has been observed (Khalak, Williamson 1996, Hover, Techet et al. 1998). In cylinder experiments on the

upper lock-in branch give rise to low amplitudes ViV for low V_r, while for the lower branch low amplitudes are observed for large values of V_r.

While augmenting or reducing the oscillation frequency, de-synchronization values can also be achieved that differ very little from the limits of the synchronization values; on the transition to these limit frequencies, hysteresis and switch phenomena occur (Berger 1967). Hysteresis can be observed in the time history of variables; the maximum of a variable takes place at different time instances for increasing or decreasing the independent parameter. It originates from the fluid part of the system and not from the structural part i.e. it is not the structural response of the cylinder that leads to this hysteretic behaviour (Parkinson 1989, Brika, Laneville 1993); rather it corresponds to an induced phase shift between the lift force and the cylinder's motion frequency. Staubli(1983) concluded that the hysteresis effects are due to a nonlinearity between the fluid force and the amplitude of the vibration. Switch is the phenomenon appearing when; while increasing or decreasing the independent parameter the measured variable is '*choosing*' a different branch of values to demonstrate. A useful review on the ViV phenomena occurring can be found in the paper (C. H. Williamson 2011).

2.1.1 Shear flow ViV

It is customary in stationary cases to examine the result of a shear flow around a circular cylinder; a linear or non-linear velocity profile is imposed at the inlet. The shear flow for low Re numbers affects mainly the mean lift force as the shear brakes the flow symmetry around the cylinder; the vortex shedding frequency and the mean drag remain almost constant or slightly decrease with increasing the shear rate (Kang 2006).

In ViV the shear parameter affects the V_r, the range of which widens as the shear parameter is increasing(Gsell, Bourguet et al. 2017). For Re equal to 100, low values of shear in the region of $[0,0.2]$ and low response amplitude cases the vortex shedding frequency and patterns are comparable to the uniform current cases; what changes is the forces frequency ratio. In the uniform flow around a cylinder, the forces frequency ratio is 2:1; the shear alters the ratio to unity while a negative mean lift force appears(Gsell et al. 2017). For higher shear values in the region $[0.2,0.3]$, the flow is characterized by unsteadiness in the wake region, asymmetric patterns appear. The vortex shedding frequency is decreasing with the shear, while the mean drag force is significantly reduced. For the higher values of shear the flow becomes steady as far as it concerns the patterns(Gsell et al. 2017). For the high response amplitudes cases, increasing the shear parameter in the region $[0,0.2]$ does not present significant changes in the flow, the system

behaviour is similar to that of a uniform current; the effect appears in the response trajectory that is an ellipsoidal rather than a traditional figure eight response.

More information on shear flow ViV can be obtained in the aforementioned citations of the present paragraph and the papers of (Bourguet, Karniadakis et al. 2011, Huang, Chen et al. 2012, Sidarta, Lambrakos et al. 2006) and references therein.

2.1.2 Three dimensional VIV

In the context of long flexible cylinders in shear flow, the lock-in condition can be defined locally. For each spanwise position, the lock-in condition is established when the local vortex shedding frequency coincides with the local cross-flow vibration frequency. In the absence of such synchronization, the condition is referred to as non-lock-in. The spanwise region which includes all the locally locked-in positions is referred to as the lock-in region and the rest of the span as the non-lock-in region. Lucor, Imas et al (2001) observed the effect of linear and exponential shear flow on ViV of large aspect ratio cylinders; the main difference was that the linear shear induced a standing wave response along the spanwise direction while the exponential shear induced a mixed travelling-standing wave response. The linear shear flow led to a low single mode response (Sidarta et al. 2006) while the exponential shear led to high multimode response. Recently Fernandes, Mirzaeisefat et al (2014) advanced the observations of the ViV for long risers. They noticed that the span-wise motion due to an extraneous source can cause self-oscillations of the cylinder that induce ViV phenomena.

2.1.3 Forces exerted on a moving circular cylinder

The aforementioned phenomena occurring in ViV studies are engulfed in the realm of non-linear mechanics. Bishop and Hassan (1964) were the first to observe that the wake's response to the cylinder's forced oscillation was similar to that of a non-linear oscillator system; the forces exerted on an oscillating cylinder are such as might have been imposed by a non-linear self-excited fluid oscillator. The idea of the wake oscillator triggered the research for a theoretical model for the prediction of ViV phenomena. Predicting the amplitude of ViV, using forces from a flow field, would be desirable for the hydro/aero-elasticity applications and sets the base for FoV studies. Hartlen and Currie (1970) following Bishop and Hassan, developed a model for the description of the FSI. The elastically mounted cylinder is modelled in the equation (2.3) as a

second order, linear, damped oscillator on which the instantaneous value of the fluctuating lift coefficient is imposed

$$m\ddot{y} + c\dot{y} + ky = \frac{1}{2}\rho V_f{}^2 D L C_L \tag{2.3}$$

The lift coefficient is modelled by a nonlinear Van der Pol's equation (2.4),

$$\ddot{C_L} + \left(-a\,St\,\dot{C_L} + \frac{\gamma}{St}\left(\dot{C_L}\right)^3\right) + St\,C_L = \beta\dot{y} \tag{2.4}$$

where y is the position of the structure, m the mass, c the damping and k the stiffness parameters, D the diameter and L the length of the structure, β is a linear coupling coefficient, St the Strouhal circular frequency, ρ the density of the fluid, V_f the free flow velocity and a, γ the non-linear coefficients. According to Naudascher and Rockwell (2012), the $\alpha, \beta\ and\ \gamma$ parameters in the model of Hartlen and Currie are independent of the fluid motion and rely on the geometry and roughness of the flow boundaries.

As mentioned earlier in the experimental description of an FSI system, there is a self-limiting behaviour that does not allow for further increase of the pressure on the cylinder, which is an ability of the Van der Pol's equation. Studies are examining the behaviour of the system 2.3-2.4, examples of the dimensionless coefficients appearing in this context are presented in table 2-1 below.

Table 2-1 non-dimensional parameters employed in the ViV studies (Khalak, Williamson 1999)

Ratio	**Symbol**	**Formula**
Mass	m^*	$m/\pi\rho D^2\,L/4$
Damping	ζ	$\frac{c}{2\sqrt{k(m+m_A)}}$
Velocity	V_r	$\frac{V_{fl}}{f_N D}$

Studies on the V_r versus A^* plane can be found in the papers of (Feng 1968, Brika, Laneville 1993, Khalak, Williamson 1999, Govardhan, Williamson 2000), the mass and damping coefficients can be found in the studies of (O. Griffin 1980, Skop, Balasubramanian 1997, Vandiver 2012).

The proposed lift oscillator characteristics and coefficients of equation (2.4) are deduced from existing experimental data of ViV configurations. Le Cunff, Biolley et al (2002) underline that the approach utilising the equations (2.3), (2.4), does not provide a full flow field analysis but is rather phenomenological i.e. it concentrates on the fluid force as it is felt by the structure and examines the response. The advantage of the model stems from the fact that the ODE system of equations (2.3) and (2.4) is resolved faster in a computational sense than the full flow field. A summary of experimentally based models for the vortex shedding forces on oscillating cylinders can be found in the paper of Blevins (2009).

Through the studies, it was precarious to say that forced vibration studies can lead to ViV prediction for reasons that will be revealed later in the chapter. There have been several investigations dedicated to the non-similarity between the ViV and FoV results. Although empirical models have been developed based on similarities mainly with the Van der Pol (Sarpkaya 2004) or Duffing oscillator models (Srinil, Zanganeh 2012). Recently, Morse and Williamson (2006) successfully argued that if the experimental conditions for the free and forced vibration systems are precisely matching, then the lock-in phenomena occurring are in a very close agreement. On the other hand, not all the forced vibrations results could represent a free vibration case and this distinction will be emphasized in a dedicated paragraph later in this chapter.

2.1.4 The lock-in state

In structural vibrations, it is during the resonance state when big displacements and forces occur; in FSI studies the resonant behaviour of a system that consists of two different material mechanical systems, is called lock-in. During the lock-in resonance occurs for the structure while the wake follows the resonance motion. Although, there is a difference as far as it concerns the resonance state in the structural vibrations and in FSI. Traditionally, if a structural eigenfrequency is reached due to external fluid forces, resonance is expected to occur at one particular value of the force imposed externally. The previous speculation is not entirely true in FSI, it has been noticed that when the response of the structural system to the fluid forces approaches the eigenfrequency of the cylinder, there follows a range of V_r where lock-in occurs. The range depends on both structural and fluid characteristics while for all the values of the range resonance-like behaviour occurs. In the schematic of Figure 2-1 in the next page, two different perspectives can be observed, in either experimental or simulation studies, with the distinctness of how the lock-in region is approached.

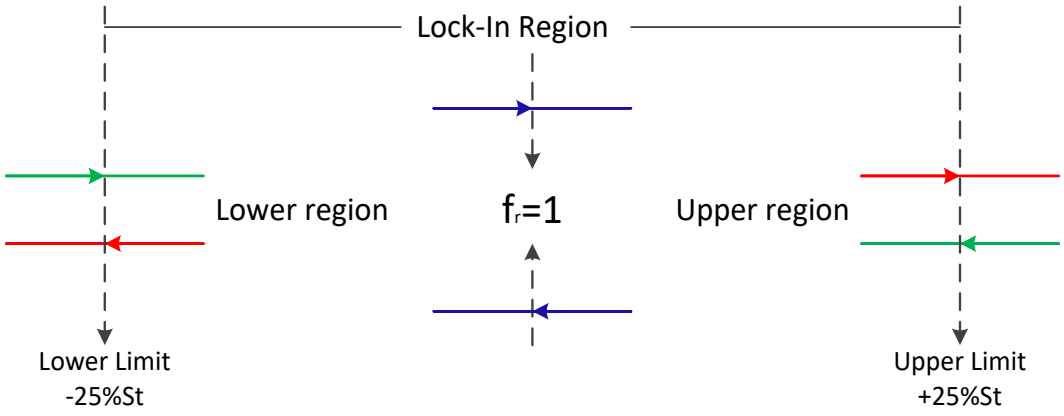

Figure 2-1 lock-in region approach methodologies, $\boldsymbol{f_r = \frac{f_e}{f_{vs}}}$

It has been observed that the synchronization region is around the unity, defining a neighbourhood of a radius approximately $\pm 25\%$ (Koopmann 1967) or $\pm$ 30% (Brown 1959) of the St number. The blue arrows signify that the tuning of the frequency takes place in the immediate region of the Strouhal frequency (O. M. Griffin 1971), rather the red (signifying exit) and green (signifying entry) arrows are placed on the limit values of the lock-in region (Koopmann 1967). The phenomena are appearing throughout the extent of the entire region, including the immediate regions of the range's limits. If the synchronization region is around the Strouhal frequency it is called "primary synchronization" region, while regions around multiples of the Strouhal frequency i.e. super-harmonic or sub-harmonic excitations have been observed presenting similar phenomena and are under study (Staubli 1983, Ongoren, Rockwell 1988).

Variations of the results occur for decreasing (blue arrows pointing left) or increasing values of the f_r(blue arrows pointing right). This phenomenon does not appear in the stationary cases where tuning the Re number value, moving up or down on the Re number axis, leads on the same graph of the St function of the Re number. Tuning the excitation frequency depends on the direction (left or right arrows) and has different results i.e. hysteresis and switch effects appear.

Enlarging on the description of the Figure 2-1, researchers are concentrating on the phenomena appearing on either the upper or the lower region, on the transition from one region to the other and in and out of the synchronization region. Anagnostopoulos (2000) observed that the forces are modulated due to the motion and present an increased amplitude when the frequency is below the lower limit of the lock-in region. He also observed that there is a transient period until the forces reach a steady state. Karniadakis and Triantafyllou (1989)defined a '*receptivity*' region in the immediate region outside the lock-in limits that presents resonant behaviour. For the lower lock-in region, the results between studies are usually in good agreement and repetitive enough to be conclusive; the lower limit is in general always at the 25-30% of the St frequency. When the excitation frequency exceeds the vortex shedding frequency, upper region in the Figure 2-1,

the flow is not purely periodic rather a quasiperiodic pattern appears. This fact is creating a discrepancy between studies and a clear upper boundary cannot be observed.

The lock-in frequency range naturally also depends on the amplitude of the vibration. There exists a threshold value of $A_e = 10\%$D so the wake gets radically affected by the motion (Koopmann 1967). Koopmann also observed that the threshold amplitude value is increasing as the deviation of the oscillation frequency from the Strouhal frequency is increasing. In ViV studies with water medium, the response amplitude in the lock-in range rarely exceeds the half of the cylinder diameter (Tsui 1982, Sainsbury, King 1971), on the contrary the response in air can be several diameters (Den Hartog 1932). Studies in FoV have also shown that the range of lock-in frequencies increases with the amplitude of the forced vibration.

Furthermore, between experimental and computational studies there is a difference on how the limits of the lock-in region are defined. In the experiments the lock-in boundary is determined from the fluid velocity traces (Honji, Taneda 1968), rather in computational studies it is defined by the hydrodynamic forces or the velocity traces if it is more exact in comparison to the experiments (Anagnostopoulos 2000). Anagnostopoulos also observed that in the upper region the oscillation amplitude has to be higher than the experimental value in order for the synchronization to occur. In the lower region there is an agreement of values between experimental and computational studies (Honji, Taneda 1968).

For the primary synchronization region of a single cylinder in fluid flow, two cases are initially examined, the transverse direction and the longitudinal direction vibration. In the first case the lock-in is observed around the Strouhal frequency rather in the latter the lock-in is observed around double the Strouhal frequency (Tanida, Okajima et al. 1973). Vibrations on the span wise direction is a by-product of the cross-flow vibrations (Le Cunff et al. 2002). A ViV configuration would employ a cylinder attached to a system of springs that would allow the cylinder to move on one direction only or two-dimensional motion from a more complicated mechanical system, rather FoV would force the vibration path of a ViV result and would examine the response of the wake. In lock-in ViV cases the motion path flow induced flow can be approximated by the following equations

$$y(t) = A_e sin(f_e t) \tag{2.5}$$

$$F_L = F_0 sin(f_e t + \varphi) \tag{2.6}$$

where the $y(t)$ is the cylinders displacement function, A_e is the excited amplitude of the cylinder, ω_e is the excited frequency of the cylinder, t is time, F_L is the lift force exerted on the cylinder, F_0 is the amplitude of the fluid force, and φ the phase difference The phase difference is a crucial variable in the FoV studies and is strongly connected to the energy exchanged between cylinder and fluid; the sign of the energy in particular, is of crucial importance. It must be underlined that in the ViV lock-in case both of the equations 2.5 and 2.6 hold at the same time. In FoV, the 'e' letter in the lower script is employed and it refers to the forced excitation amplitude and not to the response's excited amplitude. Furthermore, there is a fundamental difference between the two mechanical systems of ViV and FoV; the vortex induced motion of the cylinder occurs as a response to the perturbation of the natural instability of the wake, whereas the forced motion perturbs the natural instability causing a response of the wake (Carberry, Sheridan et al. 2005).

The forced vibrations fundamental studies and considerations will be presented in the following paragraphs. The FoV is the greater topic of the present thesis that utilises the 2.6 equation for the fluid force imposed on the flow to imitate the motion of the cylinder; the whole method will be presented in the 4th Chapter of methodology.

2.2 The Forced Vibrations

Forced vibration studies present interesting results independently of the ViV studies. Oscillating the cylinder can trigger vortex shedding for Re numbers below 47 (Baranyi 2009). For the range $40 \leq \mathrm{Re} \leq 80$, vortex shedding can be suppressed (Wehrmann 1965, Berger 1967) rendering the wake stable at Re numbers 20% higher than the stationary case (Roussopoulos 1993). For the unsteady region over Re=180 the motion of the cylinder can expand the two dimensionality of the wake up to the Re number of 300 (Nobari, Naderan 2006), 350 (O. M. Griffin 1971), 400 (Peppa, Kaiktsis et al. 2015). The motion of the cylinder can also trigger break down of the vortices into turbulence (O. M. Griffin 1971).Tanida, Okajima and Watanabe (1973) noticed that there are periods when the fluctuating lift vanishes completely, leading to the conclusion that for the specific oscillation parametrical configuration, inline harmonic oscillation in the lock-in range can supress vortex shedding.

In the FoV studies the equations (2.5), (2.6) of the last page hold, with $f_e^2 = {}^{k}/_{m}$ being the imposed excitation frequency of the structural system that either is subjected to a force (2.6) and results in the displacement of (2.5) or it is forced to be displaced as in (2.5) and the fluid force

exerted on it is that of the (2.6). Two assumptions are made when employing equations (2.5) and (2.6) for an FoV study the first is that the motion of the cylinder and the force are sinusoidal functions of time with the same frequency. The second is that the fluid force leads the motion by a constant phase angle. Numerically speaking the motion can be carried by the boundary values of the primitive variables or their fluxes, by employing a moving frame of reference or by including the motion in a force term in the fluid flow equations. In FoV the response of the one of the two mechanical components is considered given, and the response of the second is predicted. From a hydrodynamic point of view, the FoV studies research on the vortex patterns, the exerted fluid forces and their relation to the prescribed motion of the cylinder. In the present study the equation 2.5 is employed and the response of the flow is sought.

2.2.1 Forces exerted on a rigid cylinder in translational motion

A rigid body of volume ΔV per unit span, bounded by a closed surface S is translating in an incompressible viscous fluid of uniform density ρ_0, with velocity $U(t)$; the fluid is at rest at infinity.

The fluid force exerted on the cylinder can be expressed in terms of the moment of the vorticity distribution over the entire fluid space

$$\mathrm{F} = -\sigma\rho_0 \frac{\partial}{\partial \mathrm{t}} \int_{\mathrm{V_{cell}}} \mathrm{r} \wedge \omega \, \mathrm{dV} + \rho_0 \Delta \frac{\partial \mathrm{U}}{\partial \mathrm{t}} \tag{2.7}$$

where σ is the impulse of the flow i.e. the instantaneous fluid force effect to setup a flow with vortex shedding, ω is the vorticity within the fluid domain including the vorticity on the cylinder wall boundary S, r is the vorticity radius from the centre of the vortex; on the right-hand side the second term is the rate of change of momentum of the displaced fluid (Howe 1989, Lighthill 1986), while ω is the vorticity over the whole of the domain including any bound vorticity. Wu (1981) examined the impulse parameter that is ½ and 1, for three-dimensional and two-dimensional flows correspondingly.

It is also convenient to express the fluid force as the sum of three terms (Howe 1989); the inertia force due to the added mass, the vector sum of the normal surface stresses and the skin friction caused by the surface shear stresses. In the same order, the sum of the terms form the equation for the inline force yields

$$F_i = -A_{ij}\frac{\partial U_j}{\partial t} + \rho_0 \int \nabla X_i \cdot (\omega \otimes v_{rel})\, dV + \mu \oint (\omega \otimes \nabla X_i) dS \tag{2.8}$$

where A_{ij} is the fluid added mass tensor for translational motion of the cylinder, X_i is the velocity potential of the irrotational flow about the body, v_{rel} is the relative to the motion of the cylinder, flow velocity. The bound vorticity does not contribute to the volume integral of equation (2.7) as it is parallel to the surface S; its effect appears only on the skin friction, the third term of equation (2.7) (Howe 1989). Morison et al. (1950) decomposed the wave drag force exerted on a cylinder as follows,

$$F_D(t) = \frac{1}{2}\rho C_d D|U|U + \rho C_m \frac{\pi D^2}{4}\frac{dU}{dt} \tag{2.9}$$

where F_D is the inline force component, D is the diameter of the cylinder, C_d and C_m are the cycle averaged drag and added mass coefficients accordingly, ρ is the fluid density and U is the fluid velocity. Observing the equations (2.6) and (2.7) the one term difference stems from the fact that the model of Morrison assigns a shared contribution of the vorticity field to the inertia and drag coefficient. Lighthill similarly to (Morison et al. 1950) deduced an equation for the lift fluid force component. The decomposition of equation (2.7) originates in Kelvin's theorem and the assumption that the motion of the unbounded external fluid may be expressed as a linear sum of potential flow and residual vortex motion. Sarpkaya (2001) based on experimental observations and Fourier analysis concluded on the following form which employs a third term proportional to the acceleration of flow,

$$C_F = -C_d|cos\omega t|cos\omega t + C_m^*\frac{\pi^2}{K}sin\omega t - \frac{(C_m^* - C_m)\pi^2}{K}sin\omega t \tag{2.10}$$

Sarpkaya (2001) argues that the decomposition of equation (2.10) and similar models are semi-empirical and do not perform equally well through the whole range of Keulegan-Carpenter and Re numbers; the viscous drag force and the inviscid inertia force in equation (2.10) are incorrectly assumed to act independently. Sarpkaya argument concerns the effect of the creation, convection and diffusion of vorticity on the drag and the inertia component. Bishop and Hassan also postulate that there exist forces acting on the cylinder that affect the inertia force generated on the cylinder. The inertia force is also affected by the motion. The second term of equation (2.8) cannot be quantified separately for the drag or the inertia force, which justifies the argument but does not negate the result equation of 2.10 that holds for low KC numbers and high compressibility.

Staubli (1983), performed spectral analysis on the experimental results of the lift force in a crossflow vibration that produced a similar to the Morison-Lighthill decomposition; two peaks of

frequencies appeared, one was the vortex shedding frequency and the other was the oscillation frequency, the former is diminishing when the oscillation frequency approaches the Strouhal frequency and eventually disappears signifying a lock-in state. It is generally admitted that the total force on a moving cylinder (Lighthill 1986, C. Williamson, Govardhan 2008) can be decomposed into two terms as follows

$$\vec{F}_{total} = \vec{F}_{vor} + \vec{F}_{I} = -\rho \frac{d}{dt} \int_{V_{cell}} \vec{r} \otimes \overrightarrow{\omega_a} \, dV + \rho \frac{d}{dt} \int_{V_b} V_{osc} \, dV \tag{2.11}$$

Where $\vec{F}_{total}$, $\vec{F}_{vor}$ and $\vec{F}_{I}$ are the total force, vortex and inertia component forces accordingly; ρ is the density of the fluid, $\vec{r}$ is the position vector with reference to the vortex axis, the tensor product of the diameter vector on a vortex surface with the angular velocity $\overrightarrow{\omega_a}$; the vector resulting from the outer product is the velocity of the fluid on the vortex sheet. The vorticity vector $\vec{\omega}_a$ symbol subscript refers to the term 'additional vorticity' and is the vorticity over the whole domain excluding the part of the vorticity attached to the boundary in a form of a vortex sheet (Lighthill 1986, Govardhan, Williamson 2000); this is the vorticity calculated with instantaneous velocities excluding the mean velocities, that is revealing only the wake vorticity in the stationary cases excluding the vorticity in the boundary layers.

When the system is in the lock-in state, the total lift force exerted on the cylinder can be approximated (T. L. Morse 2009) by the formula,

$$C_L(t) \cong C_L \sin(2\pi f_e t + \varphi_{lift}) \tag{2.12}$$

The potential force coefficient can be calculated by the formula (2.13) (Govardhan, Williamson 2000),

$$C_{potential} = 2\pi^3 \frac{y(t)/D}{(U^*/f^*)^2} \tag{2.13}$$

The added mass force is then always in phase with the cylinder's motion, rather the vortex force and consequently the total force are in phase difference with the motion. The vortex force coefficient can be calculated by subtracting the potential coefficient from the total force coefficient,

$$C_{vortex}(t) = C_{total}(t) - C_{potential}(t) \tag{2.14}$$

where φ_{lift} is the phase difference of the lift force with the cylinder's displacement, f_e the excitation frequency and C_L is the total lift force coefficient. The vortex lift force can also be expressed as follows in the next page,

$$C_{Lvortex}(t) \cong C_{Lvortex}\sin(2\pi f_e t + \varphi_{liftvortex}) \tag{2.15}$$

In equations (2.12) and (2.15) C_L and $C_{Lvortex}$ are correspondingly the amplitude of the lift and the vortex force while the φ_{lift} and $\varphi_{liftvortex}$ are the phases of the coefficients with the cylinder's displacement.

The phase angle, between the two components and the cylinder's motion characteristics, is the quantity largely associated with the effect of the motion on the flow quantities. ViV and FoV studies are mainly concentrating on this phase relation between forces and motion which is inherently related to the hysteresis and switch phenomena accompanying the lock-in region. The breakdown of the total fluid force to the $C_{Lvortex}$and $C_{potential}$ components is related to the transition between shedding modes as the added mass component is always in phase with the motion, thus any change in the flow patterns is reflected in the variation of the vortex component (T. Morse, Williamson 2009). Carberry et al (2003), enhance the idea of studying the wake states of a cylinder undergoing controlled oscillations considering the simultaneous behaviour of both vortex and total force.

2.2.2 The Williamson- Roshko map

As mentioned earlier the St-Re number relationship is not sufficient to provide a representation of the ViV or FoV phenomena, there exist more frequencies due to the interaction of the wake and the cylinder's motion and the appearance of the hysteresis and switch phenomena is disrupting the continuity of the results. In the FoV studies an amplitude- frequency plane is set and it is preferred to map on it all the induced phenomena according to the oscillation characteristics,

$$A_r = \frac{A_e}{D} \tag{2.16}$$

$$L_r = \frac{V_e T_e}{D} = \frac{\lambda_e}{D} \tag{2.17}$$

$$f_r = \frac{f_e}{St} \tag{2.18}$$

In the current thesis the equations (2.16) and (2.18) are employed. Different approaches can be sought which are presented in the following paragraphs. Each approach is examining a different characteristic of the interaction on the amplitude-frequency plane. Namely the most important are the fluid forces magnitude, their phase with the cylinder's motion and the energy exchange between fluid and structure. The use of the amplitude-frequency plane for the representation of the vortex patterns according to the oscillation characteristics was introduced by Koopmann(1967) and later used Griffin and Ramberg (1976) who placed on the map a review of the locked-in inline oscillations vortex patterns, for various Re numbers that had appeared in the research.

Williamson and Roshko (1988) similarly studied the vortex patterns appearing in the wake of an oscillating cylinder onto the amplitude-wavelength plane for $300 < \mathrm{Re} < 1000$. They categorised the vortex patterns as follows; the symbol S refers to a "*singlet*" or a single vortex, the letter P refers to a pair of opposite sign vortices, the letter C refers to a coalescence of small vortices which eventually form one large vortex further downstream in a similar to Benard-Karman street. Furthermore, they related the oscillation's characteristics with the wake patterns; the acceleration of the body induces a further roll-up of the two shear layers i.e. in excess to the primary vortex formation roll up, that increases the total number of the vorticity regions around the cylinder. The extra vorticity regions are of the same sign as the primary vortex shed from the same side; below a critical wavelength, the same sign vorticity regions merge eventually developing a Benard-Karman street, while above that threshold wavelength the new vorticity regions grow stronger independently of the primary vortices, and the pairing of the opposite vorticity regions takes place (2P mode). It is understood that the acceleration of the cylinder excites the shear layers roll up and the amplitude affects the growth of the new vorticity produced.

Ponta and Aref (2005) in an attempt to quantify the effect of motion on the pattern and the transition from one to another determined the family of limit lines between the amplitude-frequency plane regions. The limit lines between the patterns were based on a theoretical observation made by admitting a mechanism that would engulf the splitting mechanism of the vortex shedding in relation to the oscillation characteristics, see Figure (2-2) of the next page. In explain, the limit lines, in general, follow a trend and form two families of lines, one circumferential and one radial forming like that circular disk fragments on the (A_r, f_r) plane. On the interior of each fragment the S, *P*, *C* patterns or combinations of them corresponding to the oscillation characteristics are assigned as observed on the Williamson and Roshko map (1988). Observing the Figure (2-2), in the C-segment of the trajectory the motion of the cylinder abruptly

changes direction, the rapid change in the angle of inflow interrupts the current shedding process that is attempting to recover in the next oscillation segment R.

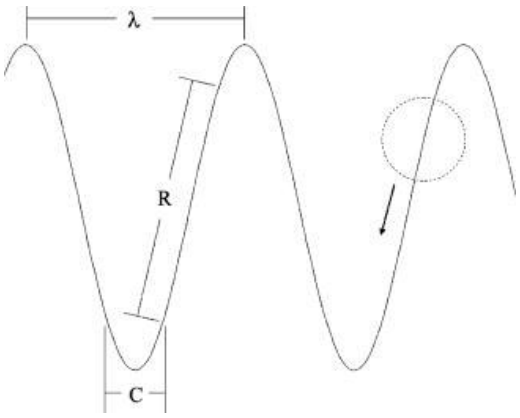

Figure 2-2 Harmonic motion of a cylinder. Forced trajectory segments C and R, λ is the wavelength of the sinusoidal motion (Ponta, Aref 2005)

The motion on the R- segment affects differently since there is no abrupt change but the acceleration of the cylinder as mentioned earlier excites further the shear layers, while the distance R that the cylinder is covering allows for the extra vorticity developed to form a new vortex that grows and sheds or gets absorbed by the already existing vorticity. Ponta and Aref (2005) postulated that the changes in the direction of the oscillatory motion are responsible for transcending from one (A_r, f_r) plane fragment to the other circumferentially rather alternating the speed results in transcending from one fragment to the other radially.

As mentioned earlier the splitting mechanism of the initially formed or primary vortices is affected by the cylinder's motion and thus different than the usual Benard-Karman Street patterns are produced. Ponta and Aref quantified the number of vortices produced each cycle based on the following hypothesis,

"*when the length of the rectilinear segment of the trajectory is comparable to an integer multiple of one-half of the distance travelled by a steadily translating cylinder in its natural shedding mode, then the wake patterns occurring have the same integer number of vortices shed each shedding cycle*".

Ponta and Aref deduced the equations for the circumferential and radial contours. The circumferential boundaries in the WR map are delineated under the empirical assumption that the length of the R-segment equals integer times $V_{fluid} \cdot T_{Shed}/2$; the equation that tracks the boundaries is then

$$\frac{\lambda_e}{D} \cdot St \cdot I_E\left(-\left(\frac{2 \cdot \pi \cdot A_e}{\lambda_e}\right)^2\right) = n \cdot \frac{\pi}{2}, n \in \mathbb{N} \tag{2.19}$$

Where λ_e is the excitation wavelength, A_e the excitation amplitude, n is the integer number representing the corresponding boundary and I_E is the elliptical integral employed for the calculation of the R-segment length.

Rather the radial boundaries stem from a different qualitative assumption based on the effect of the cylinder's motion on the period of vortex shedding; if the change of the shedding period exceeds a threshold percentage, which is small, the wake pattern changes.

Considering that the actual vortex shedding frequency can be measured by the velocity fluctuations in the wake rather than the force spectral analysis (as it is customary in stationary cases), the actual Reynolds number or peak Reynolds number $\widehat{\mathrm{Re}}$ as it completes one period of oscillation substantially deviates from the stationary case. The difference between the instantaneous vortex shedding period and its value at $\widehat{\mathrm{Re}}$ for the flow around the cylinder as it completes its oscillatory trajectory, relative to the oscillation period is,

$$\Delta_T = \frac{T_S - \widehat{T}_S}{T_e} = \frac{\frac{D}{V_f St} - \frac{D}{V_f \widehat{St}}}{\frac{\lambda_e}{V_f}} = \frac{\frac{1}{St} - \frac{1}{\widehat{St}}}{\frac{\lambda_e}{D}} \tag{2.20}$$

which produces the radial boundaries. Ponta and Aref underlined that in order to accurately define a relationship between the motion and the vortex shedding one would have to estimate the rate of strain acting on the primary vortices and develop a threshold criterion about whether the splitting is affected or the vortex escapes the effect of motion and continues downstream. Ponta and Aref studied the effect of the oscillation speed revealing that the non-constant oscillation speed affects the wake patterns and is responsible for the asymmetries appearing in the patterns; when they used a constant speed trajectory the asymmetric splitting which leads to P+S patterns did not occur.

Lam and Liu (2013) performed experiments with a circular cylinder undergoing large amplitudes of oscillation in a slow cross flow. They extended the W-R map when they observed two new patterns of vortex shedding; in the first case one pair of vortices is convected downstream each oscillation cycle and in the second two pairs are convected while two vortices remain attached to the cylinder.

2.2.3 Mode switch mechanism

Recalling from the fundamentals of flow around a circular cylinder and the vortex shedding mechanism as described by Gerrard (Gerrard 1966), the same splitting mechanism is equally

responsible for the phenomena occurring in the FoV and ViV studies. It is necessary to commence with the empirical definition of the lock-in state of the system consisting of an oscillating cylinder and the fluid flow by Williamson and Roshko (1988),

"*The trajectory wavelength is comparable with the distance a non-oscillating cylinder travels through the fluid in one cycle of vortex shedding*"

To understand the last sentence, one has to depict the experimental setup of a cylinder being towed in a tank of fluid, that is a traditional experimental method of flow around a circular cylinder. When the amplitude of an oscillating cylinder is nearly equal to the distance the stationary cylinder is towed, so to produce one cycle of vortex shedding then the vortex shedding is affected, and alternative wake patterns are produced. The term alternative refers to the different vortex patterns that will be described later in the present paragraph, but also includes the change of the vortex shape that may be compressed or grow, the vortex formation length, the formation time, the vortex strength and in general the total circulation in the fluid domain. The motion of the cylinder along with the vortex shedding process compete on which frequency will prevail, the flow is always attempting to recover the original vortex shedding process and when the cylinder oscillates at a frequency close to the Strouhal frequency then the vortex shedding obtains the oscillation frequency signifying the lock-in state.

In detail, the alteration of the wake topology is due to the switch in timing of vortex shedding (Zdravkovich 1982) and the alteration of the distribution of vorticity around the cylinder (Gu, Chyu et al. 1994). The former author observed that in the lower lock-in region ($f_r < 1$) the vortex formed on the one side of the cylinder sheds when the cylinder is at maximum amplitude on the opposite side rather for $f_r > 1$ the vortex shed on the same maximum amplitude side. Gu et al, experimentally observed the wake vorticity and streamlines of an oscillating cylinder in fluid flow for Re numbers of 185 and 5000, with oscillation characteristics of $A_r = 0.2$, and $0.8 < f_r < 1.2$; they addressed the issue of similarities occurring in the wake vortex structures of the two different Re number regimes when motion is introduced. They observed that the change of the vorticity topology, while increasing the excitation frequency, consists of two motions; the increase of the vorticity concentration and the vortex upstream movement. For the low Re while the frequency ratio is increased the large-scale vortices move closer to the cylinder reaching a point where they cannot move any closer, at that point two saddle points in the streamline patterns appears signifying a switch in the shedding pattern; Ongoren and Rockwell (1988) postulate that the vortex formation length reduction is a necessary condition for the switch to occur. Increasing the f_r results in an abrupt displacement of the primary vortex to the opposite shedding side. Ensemble averaging the vortex patterns of the higher Reynolds number Gu, Chyu et al.(1994) observed similar behaviour in the near wake. They observed that the vortex shedding after the side switch

is approximately a mirror image of the vortex shedding before the switch. The phase averaging was implemented to eliminate small scale Kelvin-Helmholtz vortices that co-exist with Karman vortices at high Reynolds numbers, the small-scale vortices are not persistent in their position for different oscillation cycles; rather the large-scale vortices were approximately maintaining their position but were distorted from one cycle of oscillation to the other. What needs to be underlined is that the two Reynolds numbers under study (Gu et al. 1994) have substantially different wake characteristics but nonetheless exhibit similar switch mechanisms when motion is introduced. For Re=185 Guilmineau and Queutey (2002) similarly to (Gu et al. 1994) observed that as the excitation frequency approaches the St frequency, the concentration of vorticity suddenly switches sides changing the topology of the patterns. Lu and Dalton (1996), observed that increasing the amplitude of oscillation reduces the value of f_r at which the switching occurs; while increasing the Re number at the same fixed amplitude has the same effect on the value of f_r where switching occurs. The last observation shows that the A_r and Re as dimensionless numbers have identical effect on the flow around a moving circular cylinder while Koopmann (1967) agrees that the frequencies of the lock-in region are both amplitude and Re number dependant.

Griffin (1971) introduced a '*synchronized wake*' parameter, for lock-in conditions and up to Re number equal to 350 that yields

$$St^* = (f_r)(1 + A_r)St \tag{2.21}$$

That relates the vortex shedding frequency to the oscillation characteristics and the St frequency.

2.2.4 Effect of motion on the wake geometry

Griffin studying the wake ratio of l_f over the wake width d_f, observed that at unity there is a breakdown of the wake into turbulence; Griffin (1971) suggests it is due to the proximity of the end of the formation region to the cylinder, influencing the interaction of the wake and the shear layers. The equation (2.22) is the relation of the wake distance ratio to the '*synchronised wake*' parameter (O. M. Griffin, Ramberg 1974), in the next page,

$$\frac{l_F}{d_F} = -3.2 - 3.3\ln(St^*) \tag{2.22}$$

As far as it concerns the vortex street geometry, the length of the segment between two consecutive vortices on the same side of the wake axis l_{vs} and the sum of lateral spacing from

the axis of two consecutive alternate side vortices $\mathrm{h_{vs}}$ experience variations due to the motion of the cylinder in comparison to the Benard-Karman street.

In general, the transverse FoV at the St frequency leads to a reduction of the $\mathrm{h_{vs}}$ and the l_{vs} remains unaltered (Koopmann 1967). For $Re = 106$, when the A_r is held constant, $\mathrm{h_{vs}}$ varies inversely with f_r, while for constant f_r it increases with the A_r; $\mathrm{h_{vs}}$ decreases with increasing the amplitude while it decreases for increasing amplitude (Anagnostopoulos 2000, O. M. Griffin, Ramberg 1974). Griffin and Votaw (1972), in their experimental investigations concluded that there is no change in $\mathrm{h_{vs}}$ when varying the amplitude of vibration; Anagnostopoulos (2000) in his numerical study concluded that, inside the lock-in region below the frequency ratio equal to one, the longitudinal spacing decreases as the amplitude increases in the region of 0.05D-0.4D, but a further increase to a value 0.5D leaves the longitudinal spacing unaltered.

For inline FoV, when the oscillation frequency is higher than twice the Strouhal frequency the longitudinal spacing reduces, rather if it is lower it increases (O. M. Griffin, Ramberg 1976). The transverse spacing of vortices can almost vanish for specific inline oscillation characteristics (O. M. Griffin, Ramberg 1974). The transverse spacing of vortices shows similar behaviour for inline and crossflow vibrations (O. M. Griffin, Ramberg 1976).

In the span-wise direction of the flow, significant modifications also occur due to the FoV (O. M. Griffin, Votaw 1972), for the Re numbers of 120-350. At a vibration frequency equal to the Strouhal frequency, while increasing the oscillation amplitude, a threshold value (around ten per cent of the diameter) is reached where there is a change in the mode of vortex filaments shedding; recall that in the stationary case the filaments are shedding at a slantwise direction (if no end plates are used). Koopmann (1967) for Re numbers of 100, 200, 300 observed that there is a value of the threshold amplitude for which the filaments suddenly align parallel to the cylinder which indicates a coherence of the separation points along the cylinder span-wise direction making the wake essentially two-dimensional and stable during the lock-in phenomenon.

Furthermore, Griffin and Ramberg (1974) also studied the age of vortices, the time to diffusion of the vortex to turbulence state (Re=144,190 and lock-in conditions). The age of vortices, after employing a Hamel-Oseen vortex model, increases with increasing the amplitude of the vibration, and decreases as the vibration frequency is increased. The rate of vorticity generation, of equation (2.23) below, is generally increasing in comparison to the stationary case (O. M. Griffin, Ramberg 1974)

$$\Lambda = \pi \mathrm{St}\left(\frac{f_e}{f_{vs}}\right)\left(\frac{K}{\pi U d}\right) \tag{2.23}$$

Where St is the Strouhal frequency, f_e is the FoV frequency, f_{vs} is the shedding frequency, K is the initial circulation before the motion, U is the free stream velocity, d is the cylinder's diameter. The Λ increases with the amplitude; in the upper lock-in region it can increase by 70% in comparison to the stationary case. Greater values of the synchronised St* of equation (2.21) of page 35 resulted in greater strength of the vortices. The changes observed in the geometrical characteristics correspond to the changes of the forces under lock-in conditions and are similar for both FoV and ViV conditions(O. M. Griffin, Ramberg 1974).

The induced street velocity varies directly with the frequency of the vibration; induced street velocity is the difference of the downstream wake velocity and the free stream velocity (Koopmann 1967). The downstream velocity is the product of the measured street wavelength and the corresponding shedding frequency; in the upper lock-in region the street velocity was higher than the stationary case value (Koopmann 1967).

The description so far is concentrating in the hydrodynamic characteristics. The energy exchanged during the interaction is important in the qualitative description of the phenomena, the phase difference of variables with the motion becomes a governing parameter. The main role of FoV is to represent a ViV phenomenon, the energy coefficient imposes limitations so the ViV can be reproduced.

2.2.5 The energy coefficient

As mentioned earlier researchers have postulated and to a degree have proved that the ViV interaction can be decoupled employing forced vibrations. It has been observed that the general flow characteristics i.e. wake structures and fluid forces exhibit the same behaviour with minor differences for a freely and a forced oscillating cylinder. It is the concept of energy transfer between the two mechanical systems that would determine the comparability of the two essentially different configurations (Carberry, Sheridan et al. 2001). For identical values of frequency oscillation and amplitudes as determined by a freely oscillating cylinder, the forced oscillation showed similar results, apart from the energy transfer which in contrary to the free case is negative, incorrectly suggesting that the cylinder would not oscillate at these parameters (Carberry et al. 2001). Studies on the energy transfer coefficient have shown that the forced oscillation is highly sensitive to the amplitude and frequency parameters determined by the ViV; a change of 1% would change the energy transfer by 25% (Leontini et al, 2006). Recall that there is an essential difference between the two mechanical systems of FoV and ViV, Blackburn and Henderson (1999) concluded that for the same reason the energy transfer is always positive for

ViV and unconstrained for forced vibrations. The energy transfer is the work done on the cylinder by the fluid over one cycle of oscillation and in dimensionless form (Blackburn, Henderson 1999) yields

$$E = \frac{2}{\rho U^2 D^2}\int_0^T \dot{y}F_l dt = \int_0^T \dot{a}C_L\, dt = \frac{1}{2}\oint C_L da + a dC_L \tag{2.24}$$

For transverse oscillations, the energy transfer varies with the component of the lift force which is out of phase with the displacement rather the in-phase inertia component does not affect the sign of the energy transfer (T. Morse, Williamson 2009). It has been demonstrated in (Carberry et al 2001) that the vortex force and the total lift force have equal out of phase vector components and the total energy transfer can be expressed in terms of either the vortex forces or the total forces, see equation (2.25) of the next page.

$$C_E \cong C_{Lvortex}\sin(\varphi_{liftvortex}) \cong C_L \sin(\varphi_{lift}) \tag{2.25}$$

The sustained motion of a freely oscillating system requires a net positive transfer from the fluid to the cylinder and will only occur when $0^o < \varphi_{lift} < 180^o$ or $0^o < \varphi_{liftvortex} < 180^o$; otherwise the energy transfer is negative i.e. from the cylinder to the fluid. The forced motion of the cylinder is not obeying this rule and both signs of energy transfer are possible.

Leontini et al(2006) in a similar manner to Williamson and Roshko superimposed a map of the wake modes on the (A_r, f_r) plane. The limit lines of the mode regions were defined by the energy transfer coefficient(Re=100,300).

At constant amplitude and variable frequency, in the lower lock-in region the energy transfer is small positive and relatively constant, at transition ($f_r = 1$) the energy coefficient is small and in the upper lock-in region the energy coefficient becomes negative (Carberry et al. 2005). Recalling from the introduction that in ViV small amplitudes of vibration occur (water medium), similarly for Re=100-180, $f_r < 1$, and $A_r < 0.6$ the energy transfer coefficient was positive thus representing a ViV state; rather for large amplitudes and increasing the f_r the energy transfer is always negative (Baranyi, Daróczy 2013). For Re=200, $f_r < 1$, and $A_r < 0.4$ Tang, Lu et al (2016) likewise observed that the energy coefficient is always positive, rather for large amplitudes $A_r > 0.6$ C_e is always negative. The change of sign depends on either the frequency or the amplitude ratio or both.

In connection to the forces behaviour during motion, the change of the sign of C_e corresponds to the change of energy transfer direction and the jump of phase difference to 180 degrees between

lift force and cylinder's displacement that is inherently connected to the change of vortex shedding modes; although it is not inherently connected to the same modes of vortex shedding see (Tang et al. 2016). In low mass-damping structures a small difference in phase angle of approximately two to four degrees can cause the system to change from positive to negative excitation (T. L. Morse, Williamson 2006).

2.2.6 Two degrees of freedom FoV

It follows that studies will expand to the two-dimensional motion of the cylinder with the oscillation trajectory having the shape of an ellipse, similar to a figure of eight or linear at an angle with the flow. In these studies due to the increased number of parameters that doubles as the motion is dictated by two sinusoidal motions transverse and inline, usually the frequency ratios for both cases are kept equal and constant and only the amplitude varies with and an amplitude ratio parameter

$$\varepsilon = {A_{inline}}/{A_{transverse}} \tag{2.26}$$

The two-dimensional trajectory studies have shown that if an inline component is introduced to the transverse motion, resulting in a 2D path, then a significant change in the shedding modes can occur resulting in more control parameters that can affect the wake as it is presented in (Jeon, Gharib 2001).

Peppa, Kaiktsis et al (2015) forced a cylinder to oscillate (figure of eight trajectory) in a flow of Re=400. They examined the effect of clockwise and counter clockwise motion of the cylinder on the dimensionality of the flow. For the counter clockwise case, they observed that forcing the cylinder at low amplitude (<0.2D) has a stabilising effect decreasing the three-dimensionality of the flow; the discrepancies between fluid flow forces between two and three-dimensional flow diminish. Rather for higher amplitudes (2.5D-3.0D) the wake becomes increasingly three-dimensional while the vortex shedding is significantly modified. Although the energy transfer coefficient remains positive for the entire range of amplitudes. For the clockwise case, the stabilising effect is stronger extending through the entire range of amplitudes, the values of forces coefficients are nearly equal for two and three-dimensional wake; the energy transfer coefficient is not always positive for the clockwise mode. The last result signifies that a clockwise response of the cylinder is less probable to occur in a ViV setting.

Baranyi and Daroczy (2013) measured the time mean and r.m.s values of the lift, drag and base pressure coefficients for an elliptical trajectory at Re=150. Baranyi observed that the r.m.s values of lift and the time mean of drag and pressure base coefficient are not affected by the amplitude ratio ε. while the time mean of lift and the r.m.s values of drag and base pressure are increasing with the ratio ε. The time mean and rms values are increased with the increase of the inline part of the trajectory amplitude. All time mean and rms values increase with the frequency ratio.

In the X-Y motion study of (Jeon, Gharib 2001) it is observed that the phase of the streamwise part of the two dimensional motion can control the sign of energy transfer. When only a transverse motion if occurring the 2P mode can be observed, while when introducing the inline motion the wake consists of single vortices shedding in a Benard-Karman street, signifying the effect of streamwise motion when it is combined with the transverse motion (Jeon, Gharib 2001).

The mean drag and the maximum lift increase with the amplitude of the transverse motion, while the amplitude of drag is not affected. The lock-in range of frequency ratios increases with the amplitude of the transverse motion (Karanth, Rankin et al. 1995).

2.2.7 FoV studies on the cross-section shape effect

Studies on various cross section shapes in ViV and FoV have also been performed. Ongoren and Rockwell (1988) performed FoV in a direction transverse to the flow for the range of Reynolds numbers $[584 - 1300]$ concluding that the threshold frequency for which there is a change in the shedding mode strongly depends on the cross section; a critical point is that there exist phenomena that do not appear in the case of fixed separation points (prism cross section) while they appear in cases of oscillating separation points (circular shapes). Cross-section studies on inline oscillating square cylinders can be found in the following papers (Troesch, Kim 1991, Tudball-Smith, Leontini et al. 2012), transverse oscillation of a square cylinder studies can be found in (Chauhan, Dutta et al. 2016, Ongoren, Rockwell 1988) while studies on triangular shape cylinders forced to oscillate transversely to the flow can be found in the paper of (Alawadhi 2013).

2.3 Summary

The present chapter introduced the reader to the FSI studies and in particular introduced the FoV concepts that stem from ViV observations. It was underlined that the fundamental mechanism of vortex shedding as explained by Gerrard hold in the moving cases as well. In general, the ViV and FoV studies attempt to understand the effect of motion on the vortex patterns appearing in the wake and the forces exerted on a moving circular cylinder. The new vorticity regions that appear will either be absorbed by the already existing vortices or will grow stronger into individual vortex patterns alternating the classic Benard-Karman street; S, P or C patterns appear while the fluid forces naturally depend on the new patterns thus presenting beating phenomena and a combination of sinusoids time-series, in contrast to the pure sinusoids that appear in the stationary cylinder cases.

The lift and the drag force can be analysed into two terms namely inertia (added mass) and vortex shedding forces. It is generally admitted that the lift coefficient time series obtain characteristics due to the motion of the cylinder that are non-linear. The lift force or the drag force can be described by a non-linear, non-homogeneous second degree differential equation namely the Van-Der Pol equation. The overall system employing the equation of the harmonic motion of the cylinder and the Van der pol equation can adequately describe the interaction between the fluid and the structure.

It was underlined that discrepancies in between FSI studies occur. A first discrepancy occurs for different fluid mediums e.g. air and water. In the stationary cases, the added mass was not appearing therefore the Re number can describe the same characteristics between the different fluid mediums; rather in the FSI cases where the interaction is allowed the added mass appears and plays an important role distinguishing the air from the water cases. Further discrepancies occur in the definition of the lock-in region; computational and experimental studies present different criteria and definitions for the onset of the lock-in.

The motion of the cylinder defines three regions on the amplitude frequency plane for constant Re number; namely the non-lock-in region, the receptivity region and the lock-in region. The last two regions present resonant, hysteresis and switch phenomena making more complex the description and categorisation of the cases. Moreover, the mechanisms of vortex shedding change according to the motion, there seems to be a resemblance of the mechanism responsible for the

switch of vortex shedding for high and low Reynolds numbers. It is important to be able to define the limits in between the three regions and the phenomena appearing.

Finally, due to the discrepancies the parameters employed to monitor an FSI case are changing into domains where both the fluid and the structural system can be represented. The Williamson Roshko map or the amplitude frequency plane is serving as the canvas where all the phenomena can be mapped and categorised. The energy map is also employed to define the two way interaction that holds in FoV and ViV cases with the distinction that the energy coefficient is always positive for ViV systems while in the FoV there is no restriction in the sign of the energy coefficient.

The current thesis attempts to investigate the three aforementioned regions on the frequency amplitude plane for a series of amplitudes and frequencies on a forced vibration setup. The relation between forces and motion is also examined leading to the speculation that the system describing the FSI system can be linear for the structural and the fluid behaviour as well. The transcendence from the non-lock-in to the lock-in regions is also described and is in accordance with the literature review presented in the present chapter. The Thesis is now advancing to the 3rd Chapter that presents the CFD and FSI methodologies employed in the present study.

3 DNS of the Navier-Stokes Equations, with a transverse oscillating force term

The Navier-Stokes equations are employed for the representation of fluid flow around a circular cylinder in a confined channel. The equations describe the conservation principles of mass and momentum.

Let $\Omega_{fluid} \subseteq \mathbb{R}_n$be an open and bounded by $\partial\Omega_{fluid}$, point set in three-dimensional Euclidean space, occupied by fluid. An Eulerian frame of reference is employed to describe the flow evolution in $\overline{\Omega}_{fluid}$ (closure of Ω_{fluid}); the velocity field $\vec{V}$ is defined as a function of position $r = (x_1, x_2, x_3)$ and time t that in Cartesian form yields,

$$\vec{V}(r,t) = \overrightarrow{\iota_1}\, v_1(x_1, x_2, x_3, t) + \overrightarrow{\iota_2}\, v_2(x_1, x_2, x_3, t) + \overrightarrow{\iota_3}\, v_3(x_1, x_2, x_3, t) \tag{3.1}$$

Where v_1, v_2, v_3 are the Cartesian velocity components which are functions of the position and time; $\overrightarrow{\iota_1}, \overrightarrow{\iota_2}, \overrightarrow{\iota_3}$ are the Cartesian basis vectors. Functions as the velocity and in general all functions $\mathcal{F} \in \Omega_{fluid}$ of space and time that describe any part of the flow are considered to be infinitely continuous or smooth $\mathcal{F} \in C^{\infty}(\overline{\Omega}_{fluid})$; the last argument is called smoothness convention i.e. velocity, density and other properties possess partial derivatives of all orders with respect to position and time.

The mass conservation or continuity equation implies that

$$\frac{\partial}{\partial t}\int_{\Omega} \rho d\Omega + \int_{S} \rho v \cdot \vec{n} dS = 0 \tag{3.2}$$

The momentum conservation equation is written as in the equation (3.3) of the next page

$$\frac{\partial}{\partial t}\int_{\Omega}\rho\vec{v}d\Omega+\int_{S}\rho\vec{v}\vec{v}\cdot\vec{n}dS=\int_{S}\overline{\mathrm{T}}\cdot\vec{n}dS+\int_{\Omega}\rho\vec{b}d\Omega \tag{3.3}$$

Finally, the energy equation is not resolved, as the flow is incompressible and the heat transfer is not examined. The first assumption made is that the fluid is considered to be Newtonian, thus the stress tensor in the first term of the right-hand side of equation (3.3) can be written in the form,

$$\overline{\mathrm{T}}=-\left(p+\frac{2}{3}\mu\nabla v\right)\bar{I}+2\mu\bar{D}, \tag{3.4}$$

where the I is the unit tensor and D is the deformation tensor that yields in the next page

$$\bar{D}=\frac{1}{2}[\nabla\vec{v}+(\nabla\vec{v})^{T}] \tag{3.5}$$

The second assumption is that the flow is considered to be incompressible and the rate of change of the fluid density is equal to zero. Under the second assumption and employing the continuity equation, the second term in the brackets of equation (3.4) vanishes, so the stress tensor is written in the following form

$$\overline{\mathrm{T}}=-p\bar{I}+2\mu\bar{D}, \tag{3.6}$$

Considering that the momentum equation is a vector equation, the final integral form of the Navier-Stokes equation employed in this thesis engulfs the following set of equations,

$$\int_{S}\rho\vec{v}\cdot\vec{n}dS=0 \tag{3.7}$$

$$\frac{\partial}{\partial t}\int_{\Omega}\rho v_i d\Omega+\int_{S}\rho v_i\vec{v}\cdot\vec{n}dS=\int_{S}t_i\cdot\vec{n}dS+\int_{\Omega}\rho b_i d\Omega,\quad where\ i=1,2,3 \tag{3.8}$$

Where

$$t_i=\mu\left(\frac{\partial v_i}{\partial x_j}+\frac{\partial v_j}{\partial x_i}\right)i_j-pi_i \tag{3.9}$$

The equations are non-linear due to the existence of the convective term, the second term of the left-hand side in equation (3.8). In the current algorithm the pressure term appearing at the right-

hand side of equation (3.9) and in turn in the surface integral, first term of the right-hand side of the equation (3.8), is considered a volumetric pressure force and through the use of Gauss theorem, the pressure gradient appears in the momentum equation as a volume integral; the final form is presented in paragraph 3.1 of the present chapter.

The equations are coupled via the velocity since a pressure term does not exist in the mass conservation equation and there is no evolution equation for the pressure. The coupling of the velocity and pressure is artificially achieved through the Poisson equation which will be explained in a separate paragraph. The only time derivative is that of the fluid velocity in the momentum equation and the flow is considered to be unsteady; the flow convergence is achieved when periodic flow occurs in the wake i.e. vortex shedding.

Traditionally fluid flow computational methods employ different computational and physical domains; the Navier-Stokes equations are transformed to accurately fit the physical domain e.g. generalised coordinates transformation, while the transformation is such so the physical space is mapped through a one-to-one correspondence to a uniform rectangular grid (computational domain) where the calculations easier to be performed. For a more detailed presentation of these methods, the reader could consult the book of Drikakis and Rider (2006) and other textbooks on CFD. In the present algorithm, the computational and the physical domains are identical, with no transformation of the equations to generalised coordinates except the derivatives in the stress tensor term; the finite volume principles are independent of the grid employed for the calculations.

The three-dimensional Navier-Stokes equations are fully resolved i.e. Direct Numerical Simulation for the primary variables of pressure and velocity of the fluid flow; no specific modelling occurs for any term or coefficient. The turbulence is explicitly resolved rather than modelled as in RANS or LES methods, thus including the very smallest scales of turbulence at the computational cost of such high-fidelity solution. The strength of DNS relies on its capacity to provide complete knowledge of the flow domain at all times unaffected by approximations; it can be considered as a numerical "*experiment*", producing results directly from the first principles(Coleman, Sandberg 2010). DNS is usually addressing turbulence characteristics, as such it is inherently unsteady and three dimensional and associated with the effect of viscosity on turbulence. The drawbacks of DNS are the high computational cost and the limitation of the maximum Re number that can be considered (Coleman, Sandberg 2010).

An FV method is preferred to discretize the flow domain which along with the strong conservation form of equation (3.7) and (3.8) inherently ensures the conservation of mass and momentum. The finite difference, interpolation or extrapolation and spectral methods are also employed for the approximation of scalars and derivatives occurring in the terms of the Navier-Stokes equations.

The equations are defined on a Cartesian grid built through the inverse transform of the coordinates. The inverse and direct transform can be observed in the Figure 3-1 below.

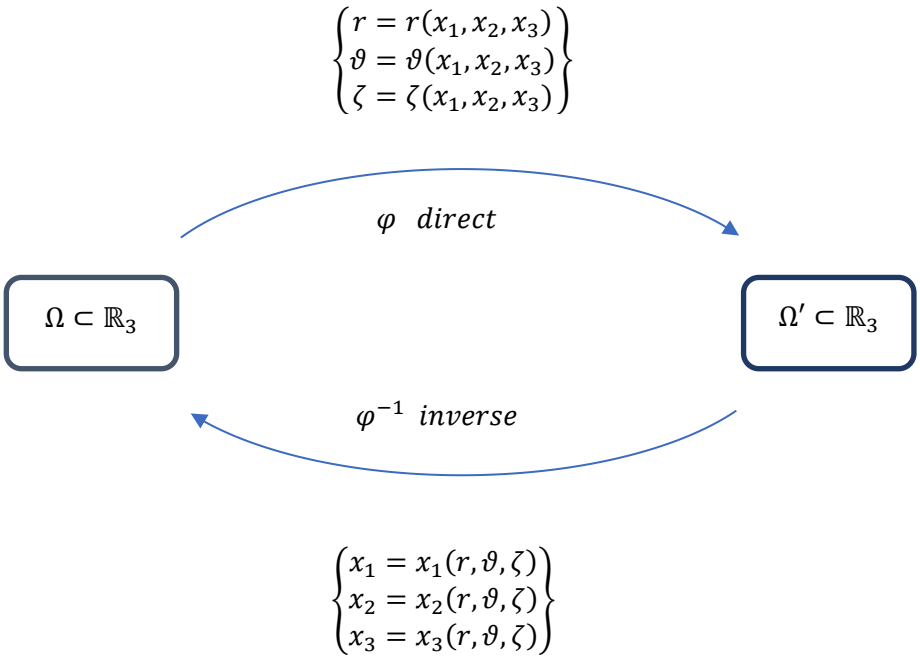

Figure 3-1 A one to one transformation map φ between Cartesian and curvilinear coordinates sets and its inverse

The aforementioned numerical methodologies will be presented applied on the integral Navier-Stokes equations in the following paragraphs. In the second paragraph, the nondimensionalized form of the Navier-Stokes equations is presented, in the third paragraph the numerical grid is presented, in the fourth paragraph the mathematical preliminaries of the algorithm are presented, in the fifth paragraph, the main discretization techniques are presented while in the sixth paragraph the overall solution methodology is presented. The current algorithm was developed by (Breuer 1998) for the stationary cases and enhanced with the motion characteristic by Hossein Madanikermani(2014).

3.1 Non-dimensionalization of the Navier Stokes equations

The Navier Stokes equations (3.7), (3.8) obtain a non-dimensional form by introducing the dimensionless variables of the next page

$$t^* = \frac{t}{L_o/V_o} \tag{3.10}$$

$$x_i^* = \frac{x_i}{L_o} \tag{3.11}$$

$$v_i^* = \frac{v_i}{V_o} \tag{3.12}$$

$$p^* = \frac{p}{\rho V_o^2} \tag{3.13}$$

Therefore, the velocities are normalised by a reference velocity V_o, the spatial coordinates by a reference length L_o and the pressure by a reference pressure ρV_o^2. When equations (3.10)-(3.13) are substituted in the equations (3.7) and (3.8) and after some calculations, the non-dimensionless integral form of the Navier –Stokes yields

$$\int_S v^* \cdot \vec{n} dS = 0 \tag{3.14}$$

$$\frac{\partial}{\partial t^*}\int_\Omega v_i^* d\Omega^* + \int_S v_i^* v^* \cdot \vec{n} dS^* = \frac{1}{Re}\int_S t_i^* \cdot \vec{n} dS^* - \int_\Omega p^* d\Omega^* + \int_\Omega b_i^* d\Omega^* \,, i = 1,2,3 \tag{3.15}$$

The result is two equations equivalent to the previous ones with the inverse of the Reynolds number appearing as a dimensionless quantity in the first term of the right-hand side of the momentum; the flow conditions are now regulated by the Re number only. For the remaining of this chapter the dimensionless form of the equations (3.14), (3.15) will be employed with the asterisks dropped for convenience reasons.

3.2 Grid of curvilinear coordinates

The computational grid is built with the inverse transform of Figure 3-1, of the previous page resulting in Cartesian coordinates from the following formulas,

$$\left.\begin{aligned} x_1 = x_1(r,\vartheta,\zeta) = rcos(\vartheta) \\ x_2 = x_2(r,\vartheta,\zeta) = rsin(\vartheta) \\ x_3 = x_1(r,\vartheta,\zeta) = \zeta \end{aligned}\right\} \tag{3.16}$$

The grid is built starting at the surface of the cylinder as in Figure 3-2 a), below, and expand with a constant factor r_e

$$r = r + r_e r_{min} \tag{3.17}$$

The computational grid is boundary fitted to the cylinder's wall and built with a C-mesh construction method. An initially stretched Cartesian mesh Figure 3-2 (a) consisting of rectangular CVs is wrapped through the use of a curvilinear mapping around the cylinder Figure 3-2(b) the Cartesian orthogonal x and y directions are now transformed to the circumferential i-direction and radial j-direction equivalently; the area in the proximity of the cylinder is densely covered by the coordinates to compensate for the high-velocity divergence areas. The curvilinear mesh is then stretched to fit the rectangular channel domain Figure 3-2 (c), forming the final mesh where the flow and calculations are performed.

The red lines represent the overlapping due to the C-mesh construction; the overlapping demands more specific boundary conditions as it will be explained in the dedicated boundary conditions paragraph 3.8 of the present chapter.

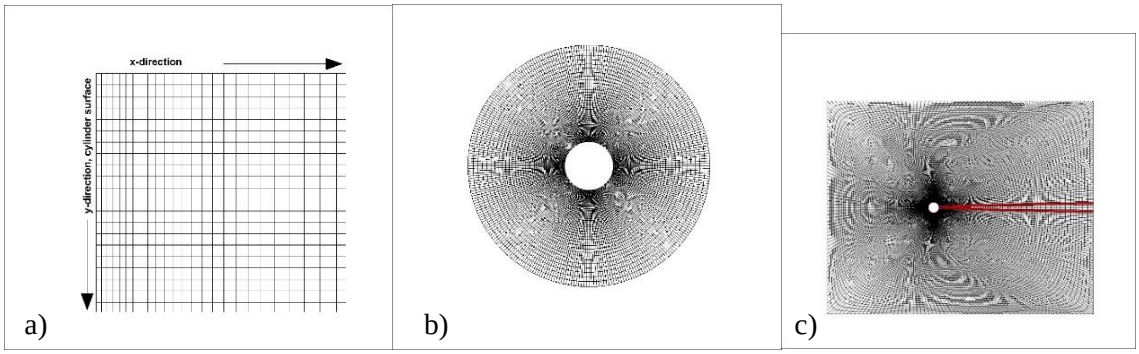

Figure 3-2 a) initial Cartesian mesh, b) curvilinear mapping of the initial mesh c) final mesh stretched to fit the rectangular flow domain; the red lines indicate the overlaping region.

The variables for each CV of the domain are collocated on the CV centre (cell-centred or non-staggered approach). The shape of the CVs varies according to which sub-region of the domain it belongs to as the coordinates are non-orthogonal, except the spanwise direction that consists of curvilinear surfaces orthogonal to the other two directions curvilinear surfaces. A simplified CV is presented for demonstration purposes in the next page Figure (3-3), depicting the compass and index notation for each CV of the computational domain.

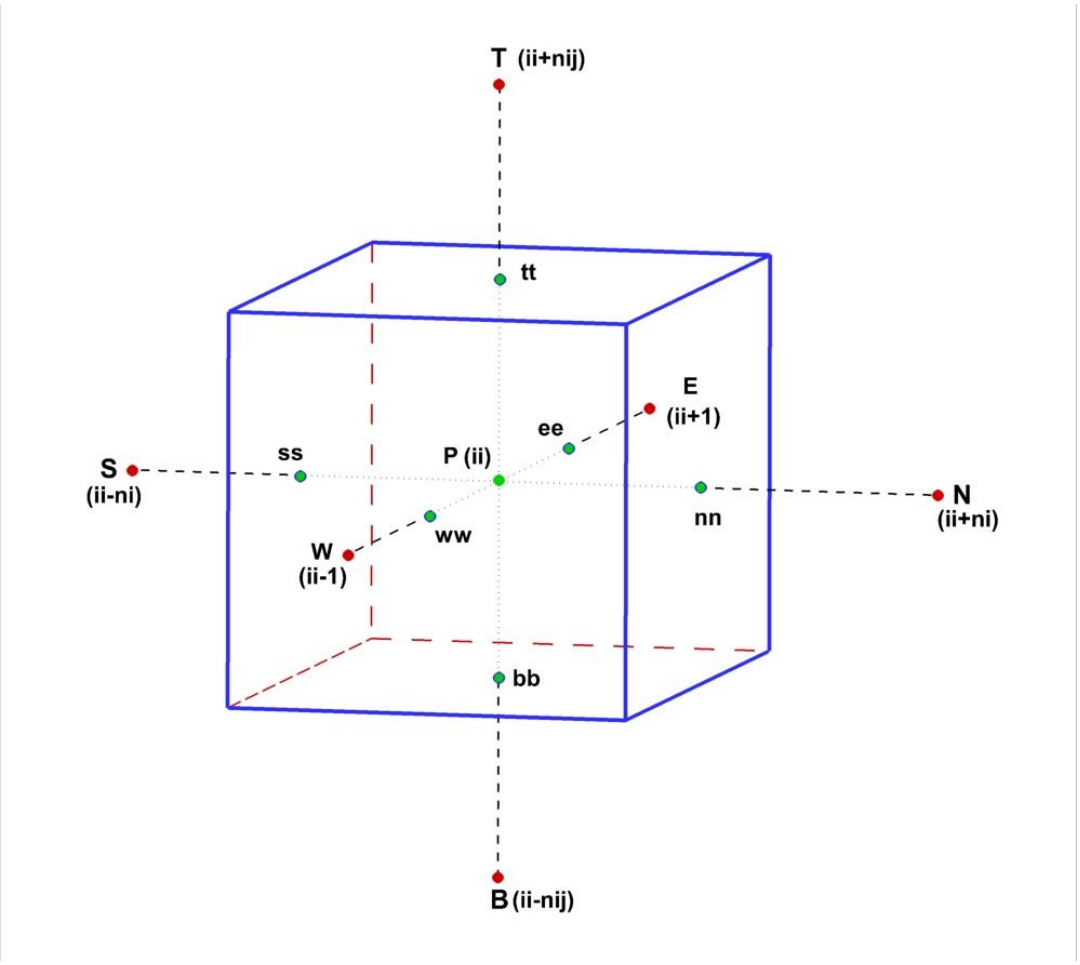

Figure 3-3 a computational stencil of a CV the current mesh indicating the compass and index notation

3.3 Mathematical preliminaries of the algorithm

Recalling from the introduction, the physical and computational domain are identical; it must be stretched that although a curvilinear coordinate setting is applied, the basis vectors for the domain remain defined on the Cartesian domain, there is no advantage in using any other basis (e.g. covariant, contravariant or grid oriented) since there is no simplification of terms due to the three-dimensionality of the flow (Ferziger, Peric 2012). As such the vectors are not transformed to a local curvilinear vector basis and the surface normal vectors are defined on a Cartesian basis namely,

$$\vec{\iota_1} = (1,0,0), \qquad \vec{\iota_2} = (0,1,0), \qquad \vec{\iota_3} = (0,0,1) \tag{3.17}$$

Thus the fluid velocity vector field is defined on a Cartesian basis as in the vector formula below,

$$\vec{V} = (v_1, v_2, v_3) = v_1\overrightarrow{\imath_1} + v_2\overrightarrow{\imath_2} + v_3\overrightarrow{\imath_3} \tag{3.18}$$

The gradient, Nabla and curl operators are also defined on a Cartesian basis

$$grad\varphi = \overrightarrow{\imath_1}\frac{\partial\varphi}{\partial x_1} + \overrightarrow{\imath_2}\frac{\partial\varphi}{\partial x_2} + \overrightarrow{\imath_3}\frac{\partial\varphi}{\partial x_3} \qquad \text{Gradient of a scalar field} \tag{3.19}$$

$$\nabla\cdot\vec{V} = \left(\overrightarrow{\imath_1}\frac{\partial}{\partial x_1} + \overrightarrow{\imath_2}\frac{\partial}{\partial x_2} + \overrightarrow{\imath_3}\frac{\partial}{\partial x_3}\right)\cdot\vec{V} \qquad \text{Divergence of a vector field} \tag{3.20}$$

$$\nabla\times\vec{V} = \begin{vmatrix} \overrightarrow{\imath_1} & \overrightarrow{\imath_2} & \overrightarrow{\imath_3} \\ \dfrac{\partial}{\partial x_1} & \dfrac{\partial}{\partial x_2} & \dfrac{\partial}{\partial x_3} \\ v_1 & v_2 & v_3 \end{vmatrix} \qquad \text{Curl of a vector field} \tag{3.21}$$

Regardless of the operators being defined on a Cartesian basis, they contain partial differential operators. In the present algorithm the spatial differential operators that appear in the equations and . the equations above, are the only terms that are transformed to a curvilinear form through the use of chain rule and the metrics of the transformation

$$\frac{\partial v_1}{\partial x_1} = r_{x_1}\frac{\partial v_1}{\partial r} + \vartheta_{x_1}\frac{\partial v_1}{\partial\vartheta} + \zeta_{x_1}\frac{\partial v_1}{\partial\zeta} \tag{3.22}$$

where the metric coefficients $r_{x_1}, \vartheta_{x_1}, \zeta_{x_1}$ etc. are calculated as follows

$$r_{x_1} = \frac{x_{2\vartheta}x_{3\zeta} - x_{2\zeta}x_{3\vartheta}}{J} \tag{3.23}$$

Where J is the Jacobian of the transformation; with a cyclic permutation of the letters and signs, the rest of the formulas for the remaining metrics can be deduced.

The aforementioned method of transforming only the independent spatial variables x_i while the vector field retains the Cartesian basis is called partial transformation. The differential form of the Navier Stokes partially transformed to curvilinear coordinates has been developed by (Ge, Sotiropoulos 2007). The advantage of the current integral form is that the spatial derivatives due to the operators that exist in the differential form, do not exist in the integrals due to the Gauss divergence theorem simplifying significantly the complexity of the equations.

More detailed information on the various forms of the integral Navier-Stokes equations according to the basis choice can be found in the thesis of Ismet Ahmed Demirdzic (Demirdzic 1982) who derived all basic forms of the transformed generalised equations namely contravariant, covariant, grid based and Cartesian form.

3.3.1 Geometrical quantities

The volume of each CV is calculated by the volume formula of a tetrahedron defined by four vertices. Given four vertices P_1, P_2, P_3, P_4 in three-dimensional space, the volume is given by the formula

$$V_{CV} = \frac{1}{6}\left\|\begin{matrix} x_1 & y_1 & z_1 & 1 \\ x_2 & y_2 & z_2 & 1 \\ x_3 & y_3 & z_3 & 1 \\ x_4 & y_4 & z_4 & 1 \end{matrix}\right\| \tag{3.24}$$

The normal vector of a CV surface is assumed to have an outward direction and is defined as the outer or vector product of the two tangent vectors of the curvilinear lines going through the CV surface central point. Given $\overrightarrow{T_1}(x_1, y_1, z_1)$, $\overrightarrow{T_2}(x_2, y_2, z_2)$ the two tangent vectors to the CV surface, the normal vector of the surface on the Cartesian basis is given by the formula

$$\vec{N}_i = \left(x_i^1, x_i^2, x_i^3\right) = \left(\begin{vmatrix} y_1 & z_1 \\ y_2 & z_2 \end{vmatrix}, -\begin{vmatrix} x_1 & z_1 \\ x_2 & z_2 \end{vmatrix}, \begin{vmatrix} x_1 & y_1 \\ y_1 & y_2 \end{vmatrix}\right), \quad i = n, w, e, s, t, b \tag{3.25}$$

Cell centres are denoted by capital letters cell faces are denoted by small letters according to the compass notation.

3.4 Spatial Discretization of the Navier-Stokes equations

DNS can satisfactorily predict all spatial variations of the dependant variables with the demand of monitoring and controlling the numerical errors. There are various strategies employed in the

spatial discretization of the N-S equations the most commonly used are FDM, FVM , FEM and spectral methods. The current algorithm employes a FV method for the spatial discretization, a spectral method is employed for the span-wise direction of the pressure variable while FDM are employed for the CV surface nodes.

The Navier-Stokes equations integral form read,

$$\int_S \rho v \cdot n dS = 0 \tag{3.28}$$

$$\frac{\partial}{\partial t}\int_\Omega \rho v d\Omega \quad = \int_S \tau_{ij} i_i \cdot n dS - \int_\Omega \frac{\partial p}{\partial x_i} d\Omega - \int_S \rho v_i v \cdot n dS + \int_\Omega \rho b_i d\Omega \tag{3.29}$$

The momentum flux vector is split into a viscous contribution (diffusive term) $\tau_{ij} i_i$ and a convective contribution consisting of the pressure contribution $\mathrm{p}i_i$ and the convective term. The form presented in (3.29) which assigns on the left hand side the unsteady term and on the right hand side all the spatial terms, is suitable for the presentation of the numerical schemes used in the present algorithm.

The fluxes are defined positive when directed outwards. The assumption that each variable is a constant inside the CV space leads to the physical assumption that the outward flux through a CV face is equal to the inward flux through the opposite (compass notation) face; the computational advantage for the current three-dimensional algorithm is that three fluxes per control volume are calculated.

Commencing the description of the algorithm the mass continuity equation is firstly treated, then the unsteady term of the momentum equation the convection, diffusion fluxes. In the following paragraphs, only the spatial discretization of the terms is considered. The time derivative of the velocity in the momentum equation is explained in a separate paragraph.

3.4.1 The continuity equation

In the case of the continuity equation, the discretization is taking place as follows

$$\int_S \rho \vec{V} \cdot \vec{n} dS = \sum_k \int_{S_k} \rho \vec{V} \cdot \overrightarrow{n_k} dS_k \,,\ k = n, w, e, s, t, b \tag{3.30}$$

Where S is the surface enclosing the CV space, S_k is the k surface of the CV, $\vec{V}$ is the velocity vector, ρ is the constant density and $\overrightarrow{n_k}$ the surface normal vector as defined in equation 3.25. Each CV surface integral of the sum is approximated by the midpoint rule. The integrand is approximated as a product of its cell-face value and the cell face area. The cell-face value is approximated by the mean value over the surface

$$F_e = \int_{S_e} f dS \cong \overline{f_e} S_e \cong f_e S_e \tag{3.27}$$

The integrand then is approximated,

$$\int_{S_e} \rho \vec{V} \cdot \overrightarrow{n_e} dS_e \cong \left(\rho \vec{V} \cdot \vec{n}\right)_e S_e = \rho\left[\overline{v_1^e} x_e^1 + \overline{v_2^e} x_e^2 + \overline{v_3^e} x_e^3\right] = \overline{m}_e \tag{3.31}$$

where $\overline{v_i^e}$ are the average values of the Cartesian fluid velocity components at the e cell face. Recalling from the introduction that the fluxes of opposite sides must be equal in magnitude but opposite direction inward or outward accordingly, the mass continuity equation using compass notation is discretized as follows

$$\boldsymbol{\overline{m}_e - \overline{m}_w + \overline{m}_n - \overline{m}_s + \overline{m}_t - \overline{m}_b = 0} \tag{3.32}$$

mass conservation serves as a kinematic constraint on the velocity field rather as a dynamic equation (Ferziger, Peric 2012) i.e. it is not resolved along with the momentum equations. The cell faces velocities are corrected, for the current time step, as it will be shown later on using the pressure gradient. The individual surface mass fluxes are used in the calculations of the momentum equation fluxes as it will be shown in the spatial discretization of the momentum equations fluxes.

3.4.2 The momentum equation

In the present paragraph, the discretization of the individual terms of the momentum equations is presented starting with the convective flux term in the following page

The convective flux term

The convective term, the third quantity on the right hand side of equation (3.29), is split into six CV face surface integrals

$$\int_S \rho uv \cdot \vec{n} dS = \sum_k F_k^C = \sum_k \int_{S_k} \rho uv \cdot \vec{n}_k dS\,, \qquad k = e, w, n, s, t, b \tag{3.33}$$

It is assumed that the u_i velocity components are constant across the CV i.e. identical values for the CV centre and the cell surface points; the convective flux is then calculated as the product of the mass flux (which is approximated by the average value over the surface) and the mean value of velocity component over the surface from the existing velocity field (Ferziger, Peric 2012) e.g. for the east side of the CV of Figure 3-3 in page 49. Employing the equation (3.31) the convective flux is approximated as follows

$$F_e^C = \int_{S_e} \rho v_e^1 \vec{V} \cdot \vec{n}_e dS = \overline{v_e^1} \left(\int_{S_e} \rho \vec{V} \cdot \vec{n}_e dS \right) = \overline{v_e^1} \bar{m}_e \tag{3.34}$$

The coefficients are obtained by summing the convective and diffusive contributions (Ferziger, Peric 2012).

The diffusive flux term

Calculation of the diffusive fluxes requires approximation of the integrand $\boldsymbol{\tau_{ij}}$ on the CV faces

$$F_e^D = \int_{S_k} \tau_{ij} i_i \cdot \vec{n}_e dS_e = \overline{(\tau_{ıJ})_k} S_k \tag{3.35}$$

The pressure term

In FV methods the pressure term is usually regarded as a volumetric force, as such the volume integral is evaluated

$$Q_P^p = -\int_S \mathrm{p} i_i \cdot \bar{n} dS = -\int_\Omega \frac{\partial p}{\partial x_i} d\Omega \cong -\overline{\left(\frac{\partial p}{\partial x_ı}\right)}_P \Delta\Omega \tag{3.36}$$

The unsteady term

The unsteady term on the left hand side of the equation (3.29)

$$\frac{\partial}{\partial t}\int_{\Omega}\rho v d\Omega = f(t,v) \tag{3.37}$$

$$f(t,u_i) = \int_S \tau_{ij} i_i \cdot \vec{n} dS - \int_{\Omega}\frac{\partial p}{\partial x_i} d\Omega - \int_S \rho v_i v \cdot \vec{n} dS + \int_{\Omega}\rho b_i d\Omega \tag{3.38}$$

The volume integral inside the time derivative is approximated by a second order approximation which replaces the volume integral by the product of the mean value of the integrand and the CV volume, the mean value is approximated by the value of the integrand at the CV centre:

$$\int_{\Omega}\rho v d\Omega = \rho\overline{v_p}\Delta\Omega \tag{3.39}$$

Where v_p represents the value of the fluid velocity at the CV centre P.

3.5 Temporal discretization (Predictor step)

The following Runge-Kutta scheme is used with three slope evaluations at each step, where n+1 denotes the next time-step and n the current time-step in the flow evolution:

$$y_{n+1} = y_n + \frac{\Delta t}{6}(k_1 + 4k_2 + k_3) \tag{3.40}$$

$$k_1 = f(t_n, y_n) \tag{3.41}$$

$$k_2 = \mathrm{f}(t_n + \tfrac{1}{2}\Delta t, y_n + \tfrac{1}{2}\Delta t k_1) \tag{3.42}$$

$$k_3 = f(t_n + \Delta t, y_n - \Delta t k_1 + 2\Delta t k_2) \tag{3.43}$$

Applying the third order RK scheme described in equations (3.40) to (3.43) the equation (3.34) discretized in time becomes, using the approximation (3.35) instead of the integral of (3.33)

$$(\rho u_i)_{n+1} = (\rho u_i)_n + \frac{\Delta t}{\Delta\Omega 6}(k_1 + 4k_2 + k_3), \tag{3.44}$$

from (3.41)

$$k_1 = f(t_n, y_n) = f\big(t_n, v_n(t)\big), \tag{3.45}$$

the k_2, k_3 of the second and third sub-step are calculated from (3.42) and (3.43) until the algorithm is complete and the flow solver moves on to the next timestep.

Thus for each sub-step of the Runge Kutta algorithm the quantity (3.33) written also in spatially discretized form

$$f(t, u_i) = \frac{1}{Re}\overline{(\tau_{ij})_k} S_k - \overline{\left(\frac{\partial p}{\partial x_i}\right)}_P \Delta\Omega - \bar{u}_e \bar{m}_e + \overline{b_{i,P}}\Delta\Omega \tag{3.46}$$

is calculated for the i^{th} direction.

The equations (3.44) and (3.46) can be written in a compact form to ease the unfolding of the algorithm

$$(\rho u_i)_{n+1} - (\rho u_i)_n = \frac{\Delta t}{\Delta\Omega 6}(H_i^n - \overline{\left(\frac{\partial p}{\partial x_i}\right)}^n \Delta\Omega), \tag{3.47}$$

After the time advancement has finished with the completion of the three time sub-steps of Runge-Kutta, an estimate of the velocity field has been calculated that in general does not satisfy the continuity equation at the new time step. In the following paragraph the methodology is advanced to the corrector step that guarantees the mass conservation

3.6 S.I.M.P.L.E. pressure velocity coupling

The SIMPLE velocity-pressure coupling scheme was developed by Patankar and Spalding (Patankar, Spalding 1972) and it is a predictor-corrector method. Commencing the main part of

the algorithm a velocity field $u_i^n$and a pressure field $p_i^n$are introduced at time t_n , the velocity field does not necessarily satisfy the incompressibility constraint of the continuity equation, and it will be corrected through the use of continuity equation in combination with the Poisson equation. The aforementioned method presents similarities with the projection methods and more information can be found in Drikakis and Rider book (Drikakis, Rider 2006). The predictor step has been performed utilising the Runge-Kutta with three sub steps in the time discretization of the unsteady term in the previous paragraph. The predictor step is the two steps of the SIMPLE method which can be described as follows

- Start with a velocity field v_i^n and a pressure field p^n at time t_n
- The Runge-Kutta provides an estimation of the new time step velocity field that is not divergent free.

At this step of the method, the momentum equation is in the form of equation 3.47. The continuity is now enforced by applying the divergence operator on the equation 3.47; the operator is applied numerically resulting in the following equation

$$\frac{\delta(\rho u_i)_{n+1}}{\delta x_i} - \frac{\delta(\rho u_i)_n}{\delta x_i} = \frac{\Delta t}{\Delta\Omega\, 6} \frac{\delta(H_i^n - \overline{\left(\frac{\partial p}{\partial x_\iota}\right)}^n \Delta\Omega)}{\delta x_i} \tag{3.48}$$

The first term is the divergence of the new velocity field which is zero, the second term is zero if continuity is enforced at the previous time step (if not it is left in the equation), the H_i^n term may contain zero terms due to the continuity imposed at the previous term but similarly to the second term it is kept in the equation. Rearranging under the previous assumptions results in the equation of the next page

$$\frac{\delta}{\delta x_i}\left(\overline{\left(\frac{\partial p}{\partial x_\iota}\right)}^n\right) = \frac{\delta H_i^n}{\delta x_i} \tag{3.49}$$

The equation 3.49 above is a Poisson equation and the pressure field that satisfies the equation corrects the velocity field that now will be divergent free.

As the momentum equations are vector equations, the Poisson equation of 3.49 is derived for each direction. Although the particular algorithm is employing a spectral method for the spanwise direction with the first term of the equation occurring from the divergence being evaluated by a sum of Fourier series; it is assumed that pressure is a periodic function in the spanwise direction, thus the boundary conditions of the pressure in the spanwise boundaries are periodic. The

advantage of the algorithm when the spectral method is employed stems from the fact that the matrix system occurring from the Poisson system of all the CVs is a two dimensional system with the third dimension being separately calculated from the spectral method, thus the solution is significantly simplified to a 2D system. The matrix system of the Poisson equations is solved using a SIP solver also known as Stone's method; more information on Stone's method can be found in (Ferziger, Peric 2012).

3.7 Forced vibration of the cylinder

Vibration of a discrete mass (body oscillator) can be described in terms of sinusoidal functions. The harmonic motion of the form,

$$x(t) = A_r \sin(\omega_r t)\,, \omega = 2\pi f_r \tag{3.50}$$

where x is the body deflection from its mean position, x_0 the amplitude, ω the circular frequency, t the time and f the frequency in cycles per second or Hertz. The equation (3.50) is traditionally employed for the representation of the harmonic motion, transverse or longitudinal, of a rigid circular cylinder in fluid flow.

Moving frame of reference

The moving frame of reference algorithm of Li, Sherwin et al (L. Li et al. 2002) is employed; considering that the body moves with translation $d = (g(t), h(t))^T$ and rotational angle $\theta = \theta(t)$ in the absolute frame of reference (x', y') the corresponding moving frame of reference can be attached to the body through the transformation

$$x' = g(t) + xcos\theta + ysin\theta \tag{3.51}$$

$$y' = h(t) - xsin\theta + ycos\theta \tag{3.52}$$

Deriving the expressions for the temporal and spatial operators, see (L. Li et al. 2002) for details, the Navier Stokes equations transform to the moving frame of reference as follows

$$\nabla v = 0 \tag{3.53}$$

$$\frac{\partial v}{\partial t} + (v \cdot \nabla)v = -\nabla p + v\nabla^2 v + G(v,t) \tag{3.54}$$

$$G(v,t) = 2\dot{\theta} I_o v + \left(\dot{\theta}\right)^2 x + \ddot{\theta} I_o x - A^T \ddot{d} \tag{3.55}$$

Where $2\dot{\theta} I_o v$ refers to the Coriolis force, $\left(\dot{\theta}\right)^2 x$ is the centrifugal force and the last two terms are related to unsteady translation and rotation equivalently; the matrix A is the rotation matrix and A^T its transpose. As the current study is concerned only with the transverse unsteady translation of the cylinder only the last term of equation 4.55 is employed with A being the unit matrix and $\ddot{d}$ the cylinder's acceleration due to the harmonic motion. Thus the motion can be represented by employing a volume force on each CV with the acceleration applied on each CV mass

$$\ddot{d} = -\omega^2 x_0 \cos(\omega t) \tag{3.56}$$

being applied on the y direction momentum equation for the transverse direction.

3.8 Boundary conditions

Following (L. Li et al. 2002) in the far field lateral boundaries of the domain a Dirichlet boundary condition is applied as follows

$$v_b = A^T(v' - \dot{d}) \tag{3.57}$$

Since the motion is taking place on the transverse to the flow direction the transverse component of the fluid velocity is changing at the boundary while for the inline component symmetry conditions are applied.

The velocity at the inlet in the stationary case would be a prescribed velocity, in a moving frame of reference the inlet flow should follow the motion thus the transverse component at the inlet

also changes with equation 3.57; if the velocity does not follow the motion stress will be developed in the near the inlet cells disturbing the flow possibly resulting to turbulence.

Cylinder wall

On the cylinder surface, since a viscous flow is considered, the energy dissipation of the fluid moving on the circumference when the fluid passes over irregularities, is sufficient to bring the fluid to rest (Richardson 1973). The no-slip condition is applied assuming that at a molecular level there is a bond between surface and fluid, thus effectively no tangential motion is allowed. On the other hand, a zero shear stress condition assumes no bond between fluid and surface, while it would allow for slip on the surface that can lead to instabilities (Pearson, Petrie 1965). Richardson(1973) proved that the no slip condition is the most appropriate boundary condition as any deviations occurring are of the same order of magnitude as the wall undulations. More information on the wall boundary conditions is available on the papers of (Richardson 1973, Day 1990)

It must be stretched that the cylinder boundary is not moving rather the moving frame of reference strictly refers to the flow moving under a force applied as described earlier, therefore the no-slip condition is serving as well as in a stationary case.

Outlet

At the outlet a convective outflow condition (Robin condition) that ensures the smooth passing of the vortex structures from the boundary without numerical disturbances, with no-reflections generated, see (Pauley, Moin et al. 1990). The transverse direction fluid velocity component does not undergo an oscillation as in the inlet case since the particular boundary condition allows for any shear stresses to go through and does not affect as in inlet where the shear stresses are developing on the immediate row of the inlet CVs if the oscillating transverse component is not included.

Overlap

As the grid is constructed with a C-mesh method at the wake branch cut there is an overlap. To account for the overlap a condition exists that copy the flow quantities from the one plane to the overlapping plane, while for the extreme nodes at the edge of the overlap symmetry conditions exist.

For the pressure a zero gradient is prescribed for all boundaries, except for the span wise direction that as mentioned earlier due to the spectral method employed the conditions for the pressure are periodic.

For the ease of understanding of the present paragraph, summary of the computational domain boundary conditions is presented in the next Figure (3-4)

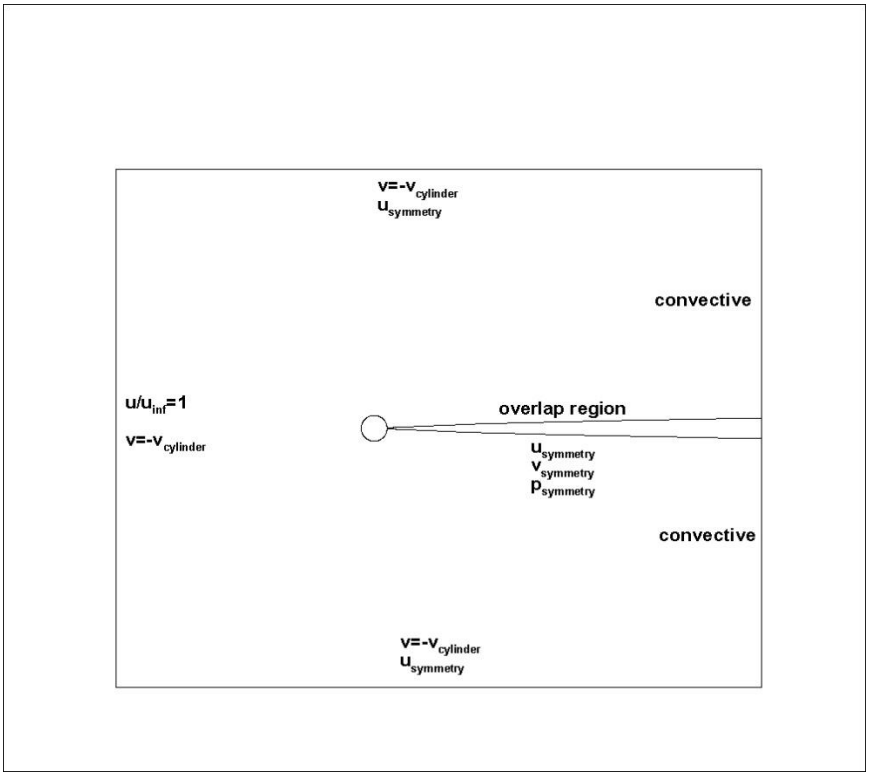

Figure 3-4 flow domain boundary conditions for the primary variables of velocity and pressure

4 Studies on the flow around a stationary cylinder

In the present chapter, the numerical results produced by the flow development as calculated by the previous chapter algorithm, are illustrated in order to validate the algorithm and compare with previous experimental and numerical studies on the stationary circular cylinder case. The Reynolds number equal to 100 is used as a benchmark for the numerical domain optimization so the physical quantities of the fluid flow around a circular cylinder are captured. The Reynolds numbers of 80, 120 and 200 are also investigated for completeness reasons so the algorithm is proved sufficient to provide credible results in the steady Karman region or periodic regime that is the Re number range of the current thesis.

The D.N.S. of the fluid flow as described by the primary variables of velocity and pressure around a stationary circular cylinder is performed; the unsteady viscous incompressible flow is represented by the integral form of the Navier-Stokes equations. The finite volume method is applied until convergence i.e. a periodic solution is sought that is mainly reflected in the time-series of the fluid forces exerted on the cylinder and in the wake topology i.e. alternating vortex shedding.

In the first paragraph, the fluid flow coefficients employed in the current investigation of the flow around a stationary circular cylinder are presented. The mesh density of the numerical domain is initially examined so the main characteristics of the fluid flow are captured. The domain size study is extended with the blockage effect study on the flow physical quantities. After the mesh study is completed, the results comparison of the algorithm with previous numerical and experimental studies is presented. It is underlined that numerical discrepancies occur very often between studies and as the computational methods used are different and a complete comparison with the other studies is not feasible. As such and for completeness reasons, the results in the present chapter are compared with unconfined experimental and numerical studies for the Re number flow equal to 100.

4.1 Fluid flow coefficients

The validation of the algorithm and the comparison with previous studies is concentrating on the dimensionless coefficients presented in the equations (4.1) - (4.8) of the present paragraph. Initially, the pressure coefficient C_P is defined as,

$$C_P = \frac{P_\theta - P_\infty}{\frac{1}{2}\rho V_\infty^2} \tag{4.1}$$

where P_θ is the static pressure at a point of angle θ on the surface of the cylinder, P_∞ is the free stream static pressure or reference pressure and the denominator is the dynamic pressure of the fluid of density ρ and the free stream velocity V_∞. The base pressure coefficient is the pressure coefficient at the point of the cylinder's surface at an angle of 180^0 (opposite to the stagnation point),

$$C_{bp} = \frac{P_b - P_\infty}{\frac{1}{2}\rho V_\infty^2} \tag{4.2}$$

The base pressure coefficient is sensitive to the process of vortex shedding and general any instabilities of the wake (Tropea, Yarin et al. 2007), an increase in St is associated with an increase in the base suction coefficient (Qu, Norberg et al. 2013). The negative sign of the time averaged base pressure coefficient $-C_{bp}$ is called the suction coefficient (C. Williamson, Roshko 1990). It must be underlined that different locations are used for the reference pressure in the literature; P_∞ is sampled at the inlet (Henderson 1995) or P_∞ is the pressure at the front stagnation point (Persillon, Braza 1998); both definitions are strongly dependent on the domain's dimensions. In the present simulations, the reference pressure P_∞ for the calculation of the base pressure coefficient was sampled at the inlet section of the domain in order to avoid any possible disturbances due to the cylinder's presence.

Recalling from the paragraph 2.4, the lift and drag forces are calculated including the pressure (F_{Dp}, F_{Lp}) and the frictional components (F_{Df}, F_{Lf}). It is convenient to reduce to the non-dimensional force coefficients that for the drag and the lift force yield in the next page

$$C_D = 2F_D/\rho V_f^2 DL \tag{4.3}$$

$$C_L = 2F_L/\rho V_f^2 DL \tag{4.4}$$

Traditionally, the time averaged quantities of the force coefficients are examined, as in fluctuating physical entities it is the statistical quantities that reveal the true effect of a phenomenon. As such, the time averaged or mean drag coefficient is examined, that is

$$C_{Dmean} = \frac{\sum_{t_i}^{t_N} C_D^{t_i}}{t_i - t_N} \tag{4.5}$$

For the lift coefficient as it fluctuates around a zero mean, the averaged root mean square value is investigated to assign an effective value to the variation for the negative values, that is

$$C_{Lrms} = \sqrt{\frac{\sum_i^N \left(C_L^{t_i}\right)^2}{N}} \tag{4.6}$$

The Strouhal number, the inverse value of the non-dimensional time-mean shedding period was detected by the FFT of the time series of the lift coefficient.

The separation point in the boundary layer is customarily determined by the condition (Schlichting, Gersten 2003),

$$\frac{du}{dy} = 0 \tag{4.7}$$

or equivalently it is the point where the wall vorticity is zero

$$\tau_x = \mu \frac{du}{dy} = \mu \left(\frac{\partial v_2}{\partial x_1} - \frac{\partial v_1}{\partial x_2}\right) = -\mu \omega_z = 0 \tag{4.8}$$

The separation angle is measured on the circumference of the cylinder with the counter clockwise direction from the stagnation point towards the wake as in the Figure (4-1) in the next page.

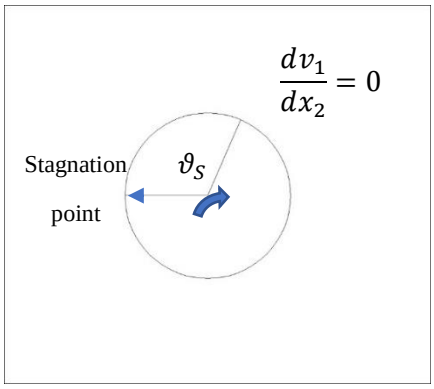

Figure 4-1 Definition of the angle of the separation point

Finally, the velocity deficit is defined as

$$V_{def} = v_1 - \bar{v}_1 \tag{4.9}$$

where v_1 is the longitudinal component of velocity and $\bar{v}_1$ is the mean longitudinal velocity component. The velocity deficit is employed for the measurement of the wake width; the wake line where the V_{def} has zero value is generally considered to be the border of the vorticity region of the wake, after that limit laminar flow occurs in the form of sheets.

4.2 Mesh Refinement

The current paragraph's study attempts to broadly set up an initial mesh to perform the tuning of the algorithm. At first place the mesh is validated under the minimum criterion of predicting the correct St number as determined by the equation (1.7) of the second chapter paragraph 2.3, that is repeated for convenience reasons below

$$St = 0.2731 - \frac{1.1129}{\sqrt{Re}} + \frac{0.4821}{Re} \tag{4.10}$$

The Strouhal number has been extensively used for validation purposes in the past research studies. Recently, Posdziech and Grundmann (2007) postulated that it is not a sufficient criterion to assure a grid independent solution as it is less affected by the grid resolution and the blockage effect. The fluid forces and the base pressure coefficient have been proved to be more stringent criteria for the investigation of the grid independence. The Strouhal number is employed as an initial criterion to

determine a start-up mesh, while the force and pressure coefficients are also employed for the refinement of the mesh. The procedure is monitored by comparing the coefficients' calculated values with those of unconfined flow studies.

4.2.1 Effect of domain size

Recalling from paragraph 3.2 of the previous chapter, the mesh density depends on the number of control volumes on each curvilinear direction, the immediate to the surface cell dimension Δ_S and the stretch factor A. These geometrical characteristics are simultaneously varying to achieve a dense coverage in the high divergence areas around the cylinder and in the near wake. The aspect ratio of the cells has to be preserved to small values to avoid numerical discrepancies, during the solution procedure. In the Table (4-1) the initial mesh test configurations are presented. Each direction, radial or circumferential, is increased by a number of 20 nodes individually of the other direction, the spanwise direction was identical for all cases; mainly the stretch factor had to be adapted to regulate the distribution of the increasing number of nodes in each direction. The equation (4.9) for Re equal to 100 results in the approximate value of 0.167 for the Strouhal number.

Table 4-1 Mesh density study

N_i	N_j	A	Δ_S	St	Timestep independency	C_{Lrms}	C_{Dmean}
286	106	1.04	0.015	0.172	-	-	-
286	126	1.04	0.01	0.171	-	-	-
286	146	1.03	0.01	0.167	No	0,412	1.22
302	106	1.05	0.01	0.170	-	-	-
302	126	1.03	0.01	0.168	Yes	0.39	1.25
302	146	1.02	0.01	0.170	-	-	-
326	106	1.05	0.01	0.170	-	-	-
326	126	1.04	0.01	0.171	-	-	-
326	146	1.03	0.01	0.172	-	-	-
Unconfined flow (Singha, Sinhamahapatra 2010),(Simulation)				0.165	-	0.226	1.431
(Zdravkovich 1997) (experimental)				0.167	-	-	1.4

The Strouhal number study significantly narrowed down the choices to two configurations ($N_i = 286, N_j = 146,\ A = 1.03, \Delta_S = 0.01$) and ($N_i = 302, N_j = 126,\ A = 1.03, \Delta_S = 0.01$). The next step of the mesh refinement study is to test the cases for timestep independency (presented in the third column) i.e. the results should not vary for different timesteps. For this purpose, the configurations that resulted in the desirable Strouhal number, were tested for the following timesteps, increasing in order $\Delta t_1 = 0.00005, \Delta t_2 = 0.0001, \Delta t_3 = 0.00015$. The Strouhal number value according to the timestep influence was over predicted by 6% of the expected value for the ($N_i = 302, N_j = 126,\ A = 1.03, \Delta_S = 0.01$) configuration and 18% for the ($N_i = 286, N_j = 146,\ A = 1.03, \Delta_S = 0.01$) case. As such the former case is preferred to proceed with the study.

After the timestep independency test, a stretch factor study was performed for the current mesh candidate. The effect of the stretch factor on the Strouhal number, presented in the Table (4-2) below, shows a great sensitivity of the numerical solution and the Strouhal number to the stretch factor.

Table 4-2 Stretch factor study

$N_i \times N_j$	A	St
302×126	1.02	0.172
	1.03	0.168
	1.04	0.171

The force coefficients values were also examined. The mesh configuration provides a good estimation of the Strouhal number but over-predicts, the C_L^{rms} by 72% and under-predicts the mean drag by 13%, see Table (4-1) in the last page. A possible factor that could affect the flow is proven to be the aspect ratio, $r_a = \frac{x_{CV}}{y_{CV}}$ of the cells in the mid region of the wake. In the immediate region around the cylinder the concentric circles building the mesh are almost equidistant, forming almost square CVs preserving a small aspect ratio The large r_a is biasing the flow in the circumferential direction as the flux integrals approximated in the y-momentum equation have a larger area multiplied by the averaged value of the velocity, incorrectly indicating increased mass flux through the CV in the circumferential direction, see Figure (4-2) of the next page.

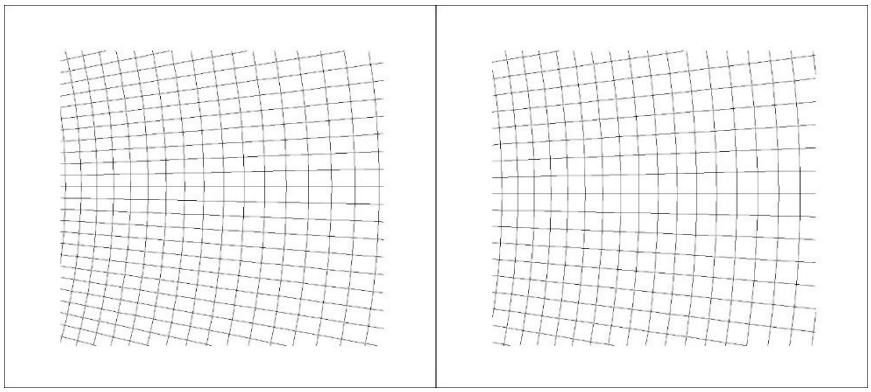

Figure 4-2 A segment of the computational domain two diameters downstream in the wake centre line, the average aspect ratio is 1.35 indicating rectangular CVs (left) and 1.05 indicating square CVs (right)

The aspect ratio was regulated by introducing more computational nodes mainly on the radial direction and at the same time reducing the stretch factor to compensate for the increased number of nodes. The final choice of the mesh based on the refinement procedure is 310x206, A=1.02 and surface cell dimension of 0.01. The results obtained improved the values of the lift and drag force coefficients, as shown in the Table (4-3), while maintaining the St number that also proves the Posdziech and Grundmann remark on the deficiency of the Strouhal number.

Table 4-3 Comparison of the results of the aspect ratio study

N_i	N_j	r_a	St	C_{Lrms}	C_{Dmean}
302	126	1.35	0.168	0.39	1.25
302	206	1.05	0.168	0.35	1.357
Unconfined flow (Singha, Sinhamahapatra 2010)			0.165	0.226	1.431

The remaining cases of the mesh density study in Table (4-2) deviated far from the expected values and cannot be considered credible. Although the unconfined flow values are not yet achieved, a more extensive study of the mesh density is not practical since the blockage effect has not been studied yet and it is largely affecting the forces exerted on the cylinder, thus the refinement study advances to the blockage effect study of the next paragraph.

4.2.2 The blockage effect

The effect of the location of the lateral boundaries on the fluid flow quantities is examined in the present paragraph. The blockage ratio is determined as the dimensionless quantity,

$$B_r = \frac{D}{H} \tag{4.11}$$

Behr, Hastreiter et al (1995) investigated the effect of the position of the lateral boundaries on a two-dimensional unsteady and incompressible fluid flow around a circular cylinder at Re=100; they observed that the minimum of channel width should be 16D so the blockage ratio effect is negligible. Kumar and Mittal (2006) postulate that the onset of vortex shedding is significantly influenced by the blockage ratio; their investigation resulted in a much higher channel width of 100D. The present investigation is examining six different blockage ratios using as a starting mesh the one defined by the mesh refinement study of the previous paragraph and then adapting the mesh to the blockage ratio study by altering the width of the channel and thus the mesh geometrical characteristics resulted from the previous paragraph. The flow domain length is also altered to adjust the mesh density and skewness of the mesh. The aforementioned choice of grid resulting from the mesh refinement study has a blockage ratio of 0.03; higher and lower values of the $B_r = 0.03$, are examined that are presented in the Table (4-4) along with the geometrical characteristics of each mesh.

Table 4-4blockage effect study cases along with the mesh characteristics

B_r	N_i	N_j	r_a	Δ_s
0.1	246	106	1.04	0.01
0.08	246	118	1.04	0.01
0.03	310	206	1.02	0.01
0.025	310	206	1.03	0.01
0.02	310	206	1.03	0.01
0.016	310	222	1.02	0.01
0.0125	308	232	1.022	0.01
0.01	300	244	1.02	0.01

The compression of the wake can be observed in the Figure (4-3) of the next page, where the vorticity contours of the seven blockage ratios under study are depicted. The compression of the wake due to the high blockage ratio is clearly observed in the Figure (4-3) (a) where the alternate vortex shedding from each side almost forms a single row of vortices rather than a Benard-Karman vortex street. The second lower blockage ratio allows for the vortices to widen their surface, although the single row of vortices is still visible. For the lower $B_r = 0.03$, $B_r =$

0.025 and $B_r = 0.016$ of the Figure (4-3) the vortex streets are almost identical with two rows of vortices forming a Benard-Karman street. The lowest blockage ratios present a slightly different image of vortices that cannot possibly distinguish the hydrodynamics due to the blockage ratio change. The distinction becomes clearer when the vortex street is observed through the wake width. The wake width is measured utilising the V_{def} of equation (4.9) of page 6. For the study of the blockage ratio the dimensions of the mesh are also adapted to compensate for the narrowing or widening of the sidewalls. The previous configuration had the width of 30D which is the third case in the Figure (4-3) (c).

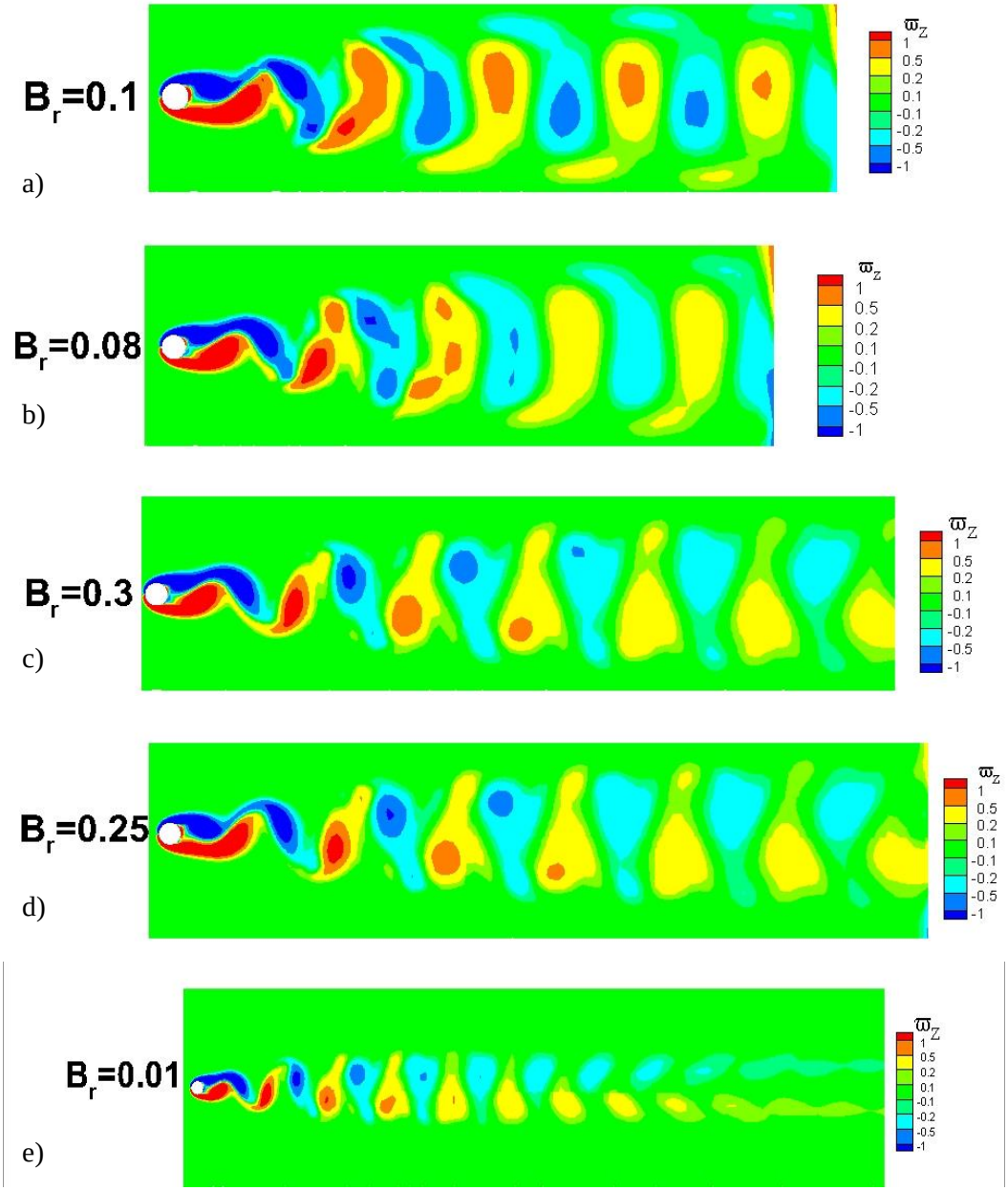

Figure 4-3 vortex streets for different blockage ratios

The increasing width of the wake observed in the first cases of the blockage ratio study agrees with Anagnostopoulos et al study on the same topic with $B_r = 0.25, 0.15, 0.05$; the image of the three ratios wakes is presented in the Figure (4-4) below(Anagnostopoulos, Iliadis et al. 1996).

The wake width is very small for the highest blockage ratio case of $B_r = 0.1$ as it can be observed by the single row of vortices of the Figure (4-3) (a) in the previous page. In the next case of $B_r = 0.08$ the wake width significantly increases despite of the small difference of the blockage ratios; in Figure 4-3 (b) the vortices are not anymore of a circular shape as in the first case of Figure (4-3) (a) rather the shape is closer to an ellipse which justifies the widening of the wake and the relaxation of the pressure due to the sidewalls proximity. The decreasing of the blockage ratio relaxes the pressure exerted by the top free flow laminar layers. The vortices grown during the formation in the near wake, are moving out of the compression due to the pressure in the near wake region of the cylinder, exerted by the shear layers. The vortex is allowed to spread and interact with the free flow in the downstream wake region; the interaction with the flow leads to entrainment of the free flow fluid by the vortex, thus the growth of the vortex and the widening of the wake.

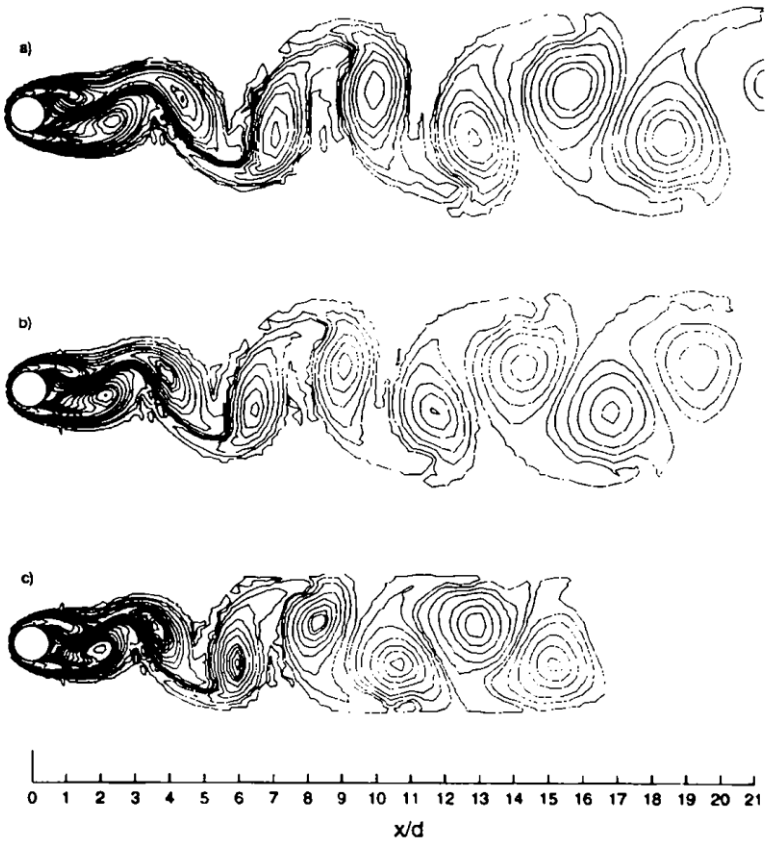

Figure 4-4 Blockage ratio study on the vortex street(Anagnostopoulos et al. 1996)

In the Table (4-5) below, the wake width at a downstream distance from the cylinder can be observed as defined by the velocity deficit. Five positions were sampled for the wake width with the maximum distance from the cylinder being common for all the cases.

Table 4-5 wake width at 5, 10, 15, 20 and 24 diameters downstream in the wake region for the different blockage ratios.

B_r	5D	10D	15D	20D	24D
0.1	2.2D	2.36D	2.6D	2.8D	3.1D
0.08	3.46D	5.3D	6.48D	7.04D	7.3D
0.03	3.78D	6.02D	6.8D	7.42D	7.76D
0.025	3.5D	6.84D	6.22D	7.46D	8.6D
0.016	3.5D	6.8D	6.1D	7.44D	7.9D
0.0125	3.4D	4.8D	5D	5.1D	5.2D
0.01	3.3D	4.4D	4.52D	5.4D	5.8D

The hydrodynamics description provides only an adequate explanation of the blockage effect, the refinement study will continue with the dependence of the flow coefficients on the blockage ratio in the paragraph of the next page.

4.2.3 The flow coefficients dependence on the blockage ratio

The frequency of the vortex shedding is increased as the vorticity fed from the boundary layer is increasing the growth rate of the vortex. Thus, the sufficient vorticity for the vortex to be shed accumulates faster decreasing the release time from the wake region near the cylinder. As it can be observed in the Figure (4-5) of the next page, the St number decreases as the B_r decreases; the current study agrees well with the results of (Qu et al. 2013) that show the same trend for the $B_r = 0.016, 0.01$ and the conclusion of (Anagnostopoulos et al. 1996) that the Strouhal number increases with the blockage ratio; Anagnostopoulos worked on a Re number equal to 106 flow and $B_r \in [0.05 - 0.25]$, he also observed the increasing St number value with the B_r.

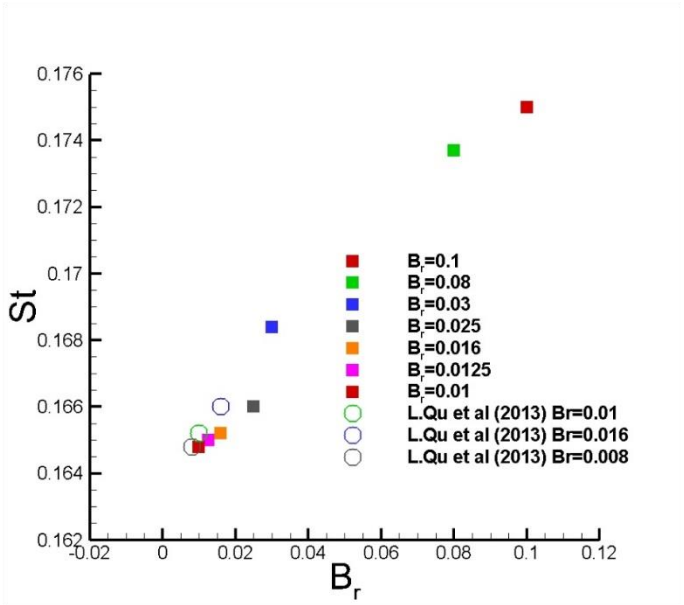

Figure 4-5 Strouhal vs blockage ratio study for Re=100 : square symbols belong to the current study results, circle symbols belong to the study of (Qu et al. 2013)

The Strouhal number presents an almost linear variation with blockage effect. A 10% decrease of the blockage effect results in a 6% drop of the Strouhal number based on the limit values of $B_r = 0.1\ and\ 0.01$.For the base pressure coefficient, it can be postulated that it decreases as the blockage ratio decreases from the higher values to the small values. Although, for the low blockage ratio cases observing the Figure (4-6) below, a clear relation between blockage ratio and pressure base coefficient cannot be observed. On the other hand, Qu, Norberg et al observed that the base pressure coefficient presents a clear trend depending on the span-wise boundaries location; this study could not be performed due to the computational time demanded. Nonetheless, the current study results on the base pressure coefficient are in a fair agreement with the studies of the papers of (Y. Li, Zhang et al. 2009, Qu et al. 2013, Rajani, Kandasamy et al. 2009).

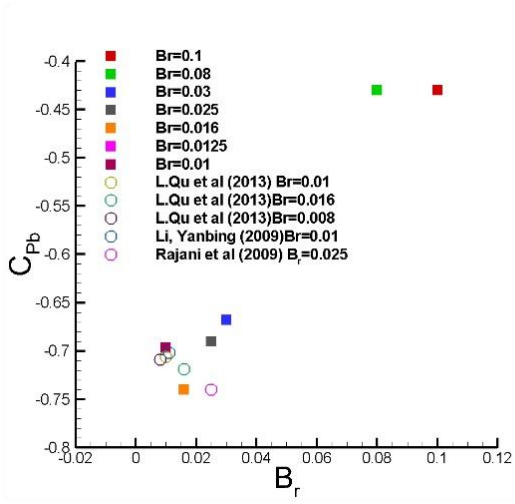

Figure 4-6 Base pressure coefficient vs blockage ratio study for Re=100: square symbols belong to the current study results, circle symbols belong to the study of (Qu et al. 2013) and

Similar trend, with the base pressure coefficient, can be observed for the lift and drag coefficients vs the B_r in the Figure (4-7) below. The r.m.s. values of the lift coefficient and the mean drag coefficient in generally decrease with the blockage ratio; for the low blockage ratio region it can be observed again that the relation is not that clear which is also verified by the studies of other authors. Discrepancies between the current study results and other studies are possibly due to the difference of the numerical methods but as it can be observed, the differences are not large and the current results can be considered to be in a good agreement with past studies results.

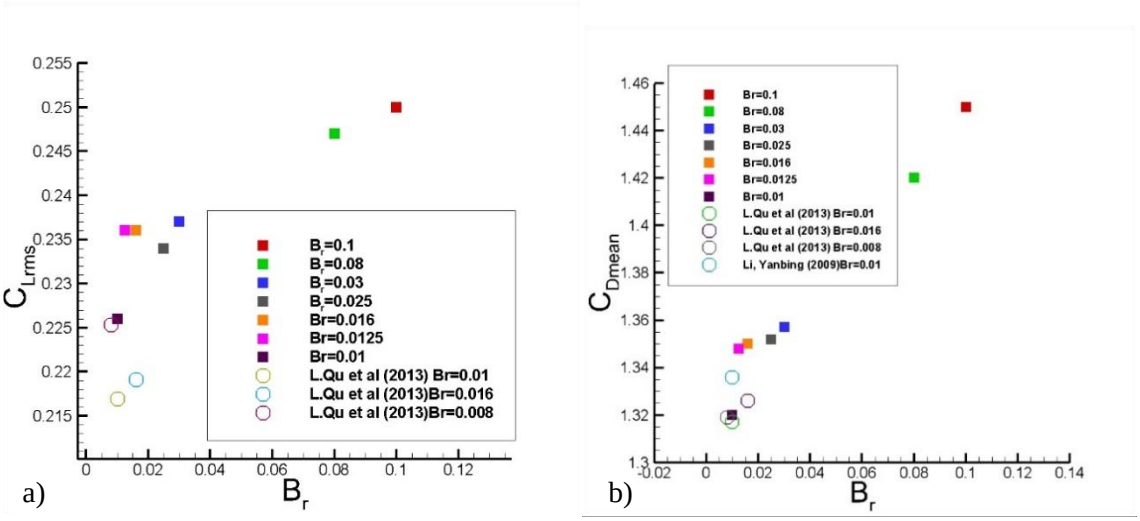

Figure 4-7 a)r.m.s. values of lift coefficient and b)mean drag coefficient vs blockage ratio study for Re=100: square symbols belong to the current study results, circle symbols belong to the study of (Qu et al. 2013) and (Y. Li et al. 2009)

The blockage effect study presented in the current paragraph is performed to compliment the refinement study so a numerically acceptable mesh can be deduced for further studies. The results have been in good agreement with past studies and the unconfined flow values were sought. In the Table (4-6) of the next page, the comparison of the final mesh results on the C_{Lrms}, C_{Dmean} and St number are presented in comparison with past numerical and experimental studies. The basic flow characteristics of unconfined flow have been achieved apart from the mean drag coefficient that presents 6% decrease from the unconfined flow value. The previous discrepancy can be safely considered acceptable, as similar differences can be observed between other studies of the Table (4-6) and values for unconfined flow (Zdravkovich 1997, Singha, Sinhamahapatra 2010).

To finalize the current refinement study, the width of the channel should be 100D, so the flow is considered free of the lateral position of the boundaries effect, that fairly agrees with the study of (Kumar, Mittal 2006). The final mesh resolution is ($N_i = 300, N_j = 244,\ A = 1.02, \Delta_S = 0.01$) and this configuration is employed for the comparison of the Table (4-7) The present mesh will

further be examined in the following paragraph for four Re namely 80, 100, 120 and 200 to examine if the change of the Re number can be captured by the current mesh configuration.

Table 4-6 comparison of flow quantities with earlier numerical results for Re=100.

Study	$-C_{pb}$	C_{Dmean}	A_{C_L}	**St**	C_{Lrms}	C_{Dp}**(mean)**
(Park, Kwon et al. 1998)	0.725	1.33	-	0.165	0.235	0.99
(Kravchenko, Moin et al. 1999)	0.73	1.32	-	0.164	0.222	0.99
(Shi, Gerlach et al. 2004)	-	1.318	-	0.164	-	-
(Mittal, Singh 2005)	-	1.322	-	0.164	0.226	-
(Stålberg, Brüger et al. 2006)	-	1.32	-	0.166	0.233	0.972
(Posdziech, Grundmann 2007)	0.709	1.325	0.321	0.164	0.228	-
(Y. Li et al. 2009)	0.709	1.336	-	0.164	-	0.995
(Behr et al. 1995) 2D	-	1.369	0.37	0.162	-	-
(Qu et al. 2013)	0.709	1.319	-	0.1648	0.225	0.984
(Singha, Sinhamahapatra 2010)	-	1.431	-	0.165	0.226	-
(Zdravkovich 1997), exp.	-	1.4	-	0.167	-	-
Present study	0.698	1.32	0.33	0.166	0.235	1.002

4.3 Fluid flow quantities for the Re number of 80,100,120 and 200

The flow coefficients, presented in the paragraph 4.1 of this chapter, will be examined for their variation with the Re number. The current study will provide a measure for the Re number adequacy of the computational mesh and the algorithm.

4.3.1 Separation Point

The time mean values of the separation angles θ_s, are displayed in the Figure (4-8) of the next page, along with other experimental and numerical studies for validation purposes. The separation point moves upstream on the cylinder circumference with increasing Reynolds number; the

change of the position is associated with the decreasing of the wall-bounded shear layer thickness (Qu et al. 2013). However, the existing data on the separation point position are only tolerably consistent presenting a deviation band of 10^o degrees; the limits of the band can be seen in the Figure (4-8),where the values from (Grove, Shair et al. 1964) define the upper limit while the values of (Homann 1936) and (M. Wu, Wen et al. 2004) define the lower limit. The present calculations are in good agreement with the lower region of the band and the studies of Wu, Wen et al. The last authors elaborated on the deviation band and more detailed information can be found in their paper.

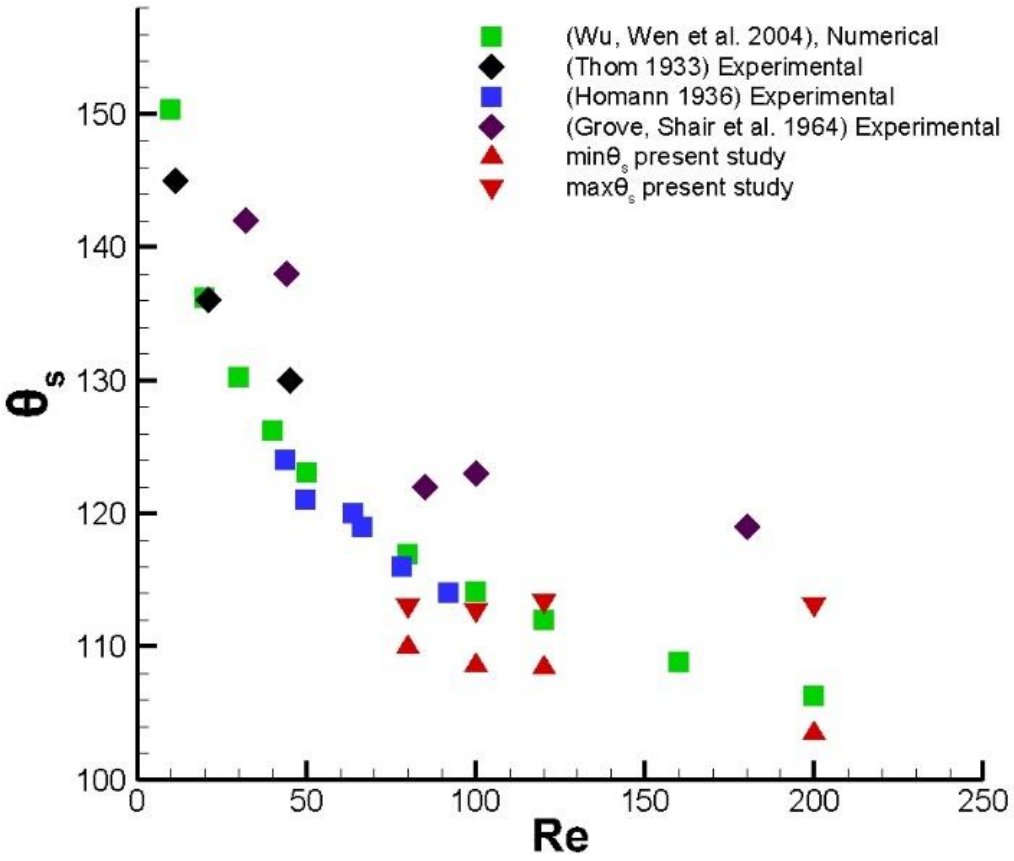

Figure 4-8 The Re=80, 100, 120, 200 minimum (delta symbol) and maximum (Nabla symbol) separation angles along with other experimental and numerical studies

In Figure (4-9) of the next page, a segment of the Re=100 flow around the circular cylinder is presented depicting the minimum and maximum of the separation point. The flow streamlines are drawn on top of the vorticity contour, to satisfy both conditions of equations (4.7) and (4.8) of page 65, depicting the area where the flow separation occurs, the wake below the separation point is dominated by vortical structures while on top the flow remains laminar in the form of sheets.

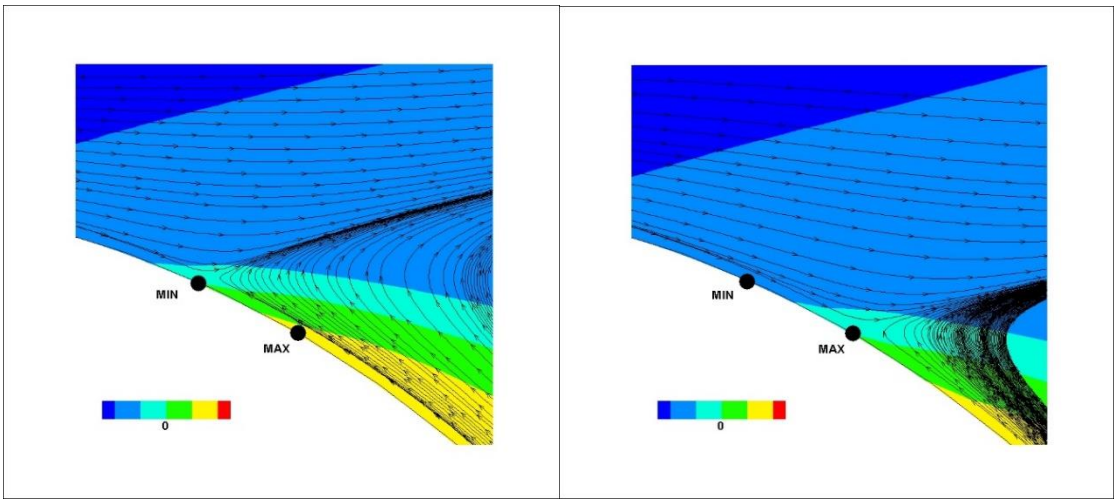

Figure 4-9The Re=100 minimum and maximum separation angles, along with the streamlines and the vorticity contour indicating the flow separation.

The separation point oscillates between the minimum and maximum positions, while the length of the path that the separation point moves on the surface of the cylinder is increasing with the Re number (Qu et al. 2013); observe the Figure (4-8) in the previous page where the distance between the minimum and maximum separation points increases with the Re number, the distance between the angles is shown in the Table (4-7) below for the different Re numbers.

Table 4-7 Re number-separation angle variation in degrees

Re	$\theta_{s_{var}}$
80	3.11
100	4.14
120	5.04
200	9.67

4.3.2 Vorticity

As described earlier the motion of the separation point upstream to the surface thickens the shear layer of the cylinder allows for more vorticity to be conveyed in the near the cylinder wake region, thus the vortex grows stronger and remains stronger further downstream. Another distinct feature of the periodic laminar regime is captured and can be observed in the Figure (4-10) of the next page; the vortices are not shed directly from the cylinder but instead the vortex path initiates at the end of the closed near wake as it is due to the instability of the wake trail, recall the description

of the second chapter for the particular regime. The Re=80, 100, 120 and 200 vortex contours of Figure (4-10) (a), (b), (c) and (d) correspondingly, present a very similar vortex street, it can be observed that the darker shades areas are increased with the Re numbers which depicts stronger vortices that can travel further downstream. In the Re=200, the vortices appear stronger than in the lower Re cases, observe the intensity of the contour colours.

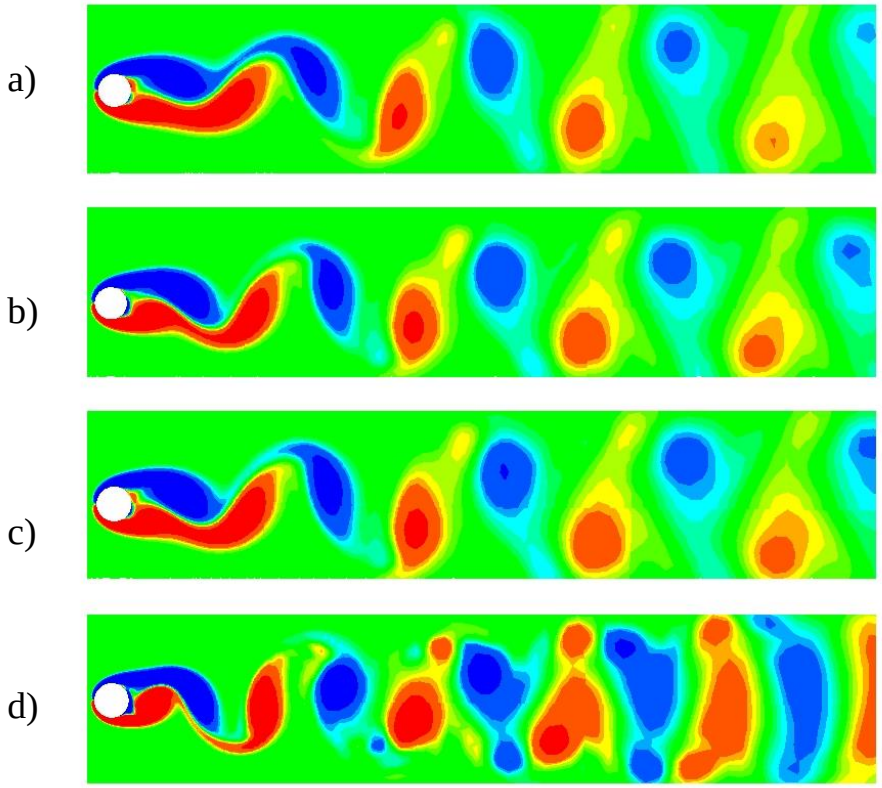

Figure 4-10 Vorticity contours of the a) Re=80, b) Re=100, c) Re=120 and d) Re=200 simulation cases.

4.3.3 The fluid flow coefficients

The r.m.s. values of the lift coefficient are presented in Figure (4-11) (i) of the next page. A good agreement is observed for the Re number of 80 and 100 while the Re=120 and 200 are underestimated. The drag coefficient dependence on the Re number can be observed in Figure 4-11 (ii), where the comparison with other studies experimental and computational cannot establish a clear relationship with the Re number; nonetheless it shows good agreement with the experimental studies of (Tritton 1959)

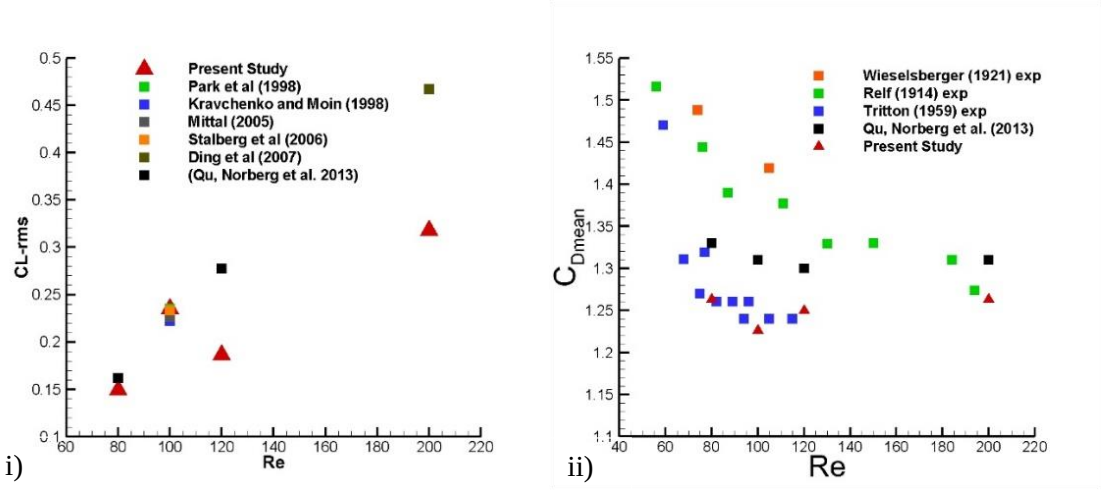

Figure 4-11 R.m.s. values of the i) lift and ii) the mean drag coefficient for the a) Re=80, b) Re=100, c) Re=120 and d) Re=200 cases in comparison with other studies.

Norberg (1994) observed that for Reynolds number lower than 250, an increase in St number is associated with an increase of the base suction coefficient which can be observed in Figure (4-12) below. A very good agreement can be observed between the values of the suction coefficient of the present study (red triangles) and the studies of (Qu et al. 2013, Kravchenko et al. 1999, Posdziech, Grundmann 2007).

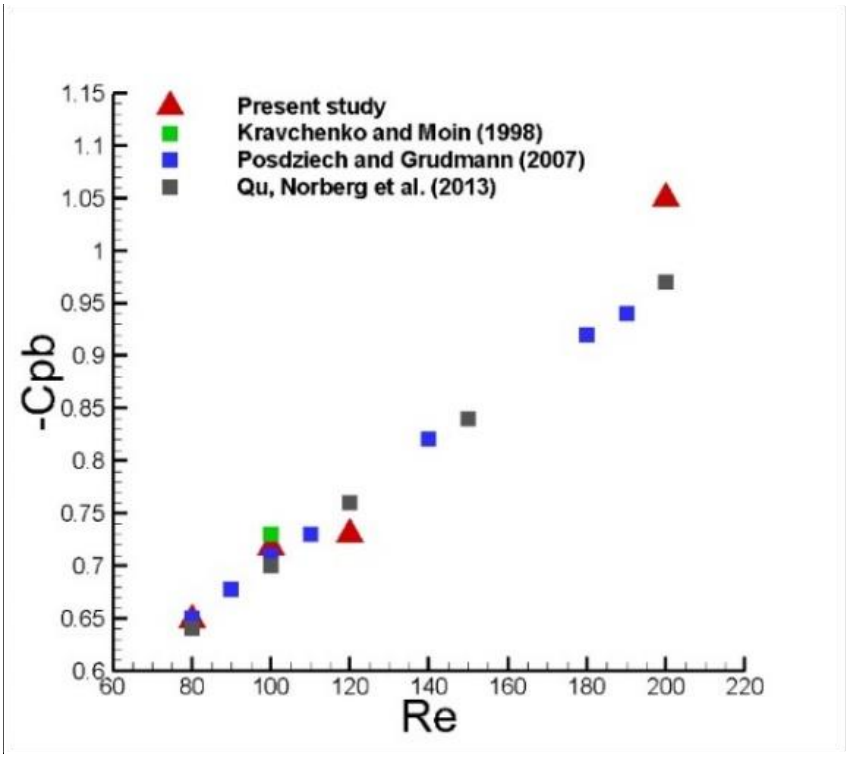

Figure 4-12 Suction coefficient of the a) Re=80, b) Re=100, c) Re=120 and d) Re=200 simulation cases.

4.4 Summary

The present algorithm described in the previous chapter has been used to simulate the incompressible flow around a circular cylinder for an initial mesh configuration. The mesh was chosen under the least criterion of Strouhal number validation. The Re number under study was the Re=100 that the Equation (1.5) of page 15, returns the value of 0.166 for the St number. Mainly of geometrical nature corrections of the mesh took place so the numerical calculations accurately predict the St number. The mesh refinement continued with the blockage effect on the force and pressure-based coefficients; it was concluded that a length of 100D would be sufficient for an unconfined flow conditions simulation. A new observation is made through the benchmark studies of this chapter. The aspect ratio of the mid-wake CVs has a significant effect on the flow quantities. Most of the studies are only emphasizing on the quality of the immediate region of the cylinder as a necessary condition for the correct results; it is proved that the distant regions are equally important for the calculations

For reasons of computational time, the 100D mesh could not be employed rather the 40D was preferred that as observed from the coefficient study of paragraph 4.4 can provide credible results for the hydrodynamics of a stationary case.

Finally, the mesh refinement study mesh configuration is tested for four Re namely 80, 100, 120, 200. The variation of the fluid flow coefficients was also examined in relation to the particular Re numbers. It can be postulated that the algorithm for the Re number variation accurately predicts the $C_{pb}, C_{Lrms}, C_{Dmean}$ values with any discrepancy with other studies being considered as traditional between studies due to numerical calculations and the level can be observed in the diagrams; the main characteristics of the flow have been successfully captured.

The study continues employing the 40D mesh for the moving cylinder cases and the results are presented in the following chapter for different amplitude and frequency ratios.

5 Transverse FoV of a cylinder in a uniform incompressible flow.

In the present chapter Numerical simulations are performed representing a cylinder forced to oscillate in a direction transverse to the fluid flow of Re number equal to 200. The motion of the cylinder is in effect from the start of the simulation i.e. in the cylinder wake flow structures have not been developed and flow separation has not occurred prior to the motion. The excitation amplitude A_e and frequency f_e are the variable parameters and the FoV cases are distinguished with one of the two being a constant. The force coefficients are the main variables examined under lock-in and non-lock-in conditions. Recalling from the literature review the study of the force coefficients present the phenomenological effect of the flow on a moving cylinder and do not contain any information on the disturbance and alteration of the wake. The forces are calculated from the integral sum of the pressure and shear forces exerted on the cylinder, therefore cannot distinguish the flow structures that develop on the cylinder's circumference and the effect of the motion on the vorticity or the pressure separately.

As mentioned in the literature review the lock-in occurs when the excitation frequency is in the neighbourhood of $\pm 20\%$ around the St frequency; recalling from the previous chapter the St frequency acquires the value of 0.199 for the present study Re number. It must be underlined that the St frequency is slightly overestimated and the value of 0.197 is considered to be the actual value according to the approximation equation (1.5) of page 15. Recalling from the previous chapter results, the fluid forces exerted on the stationary circular cylinder for the particular Re number can be observed in Figures 4-11 of page 81; to ease the reading, the mean drag coefficient obtains the value of 1.35 while the r.m.s. value of the lift coefficient acquires the value of 0.318. The results of the FoV studies are compared to the results of the stationary cases to understand the effect of the motion on the stationary cases characteristics and the quantitative differences between the FoV cases; the furthest objective of the present chapter is the quantitative description of the lock-in and non-lock-in regions.

In the Figure (5-1) below, the lock-in zone for the Re=200 is presented on the amplitude-frequency plane according to the limits established by Koopmann (1967) depicted by the red line. The present transverse oscillation characteristics are chosen so the lock-in region limits are crossed. The cases examined are discretely defined i.e. there is no continuous variation of the excitation amplitude or frequency but rather their values are defined as a constant at the beginning of each simulation case.

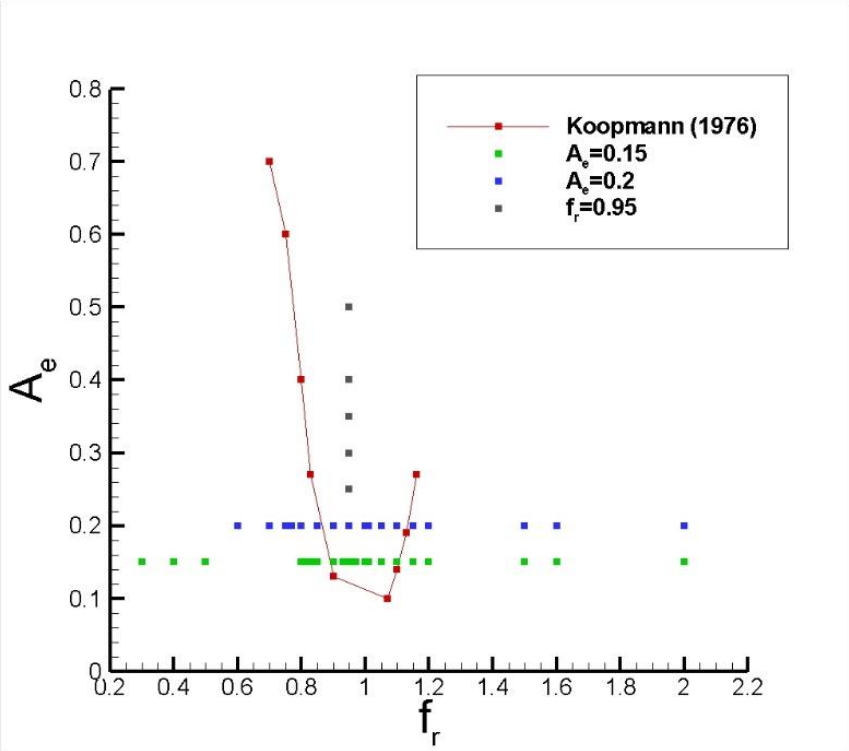

Figure 5-1 FoV cases on the (A_e, F_r) plane for Re=200 fluid flow, red line is the lock-in boundaries as defined by Koopmann (1967)

Initially the time-series of the C_L and C_D are presented followed by the spectral analysis of their FFT. The first part of the simulations is performed for constant A_e equal to 0.15 and the cases are distinguished according to the f_r values as in the Table (5-1) below

Table 5-1 The f_r cases for A_e equal to 0.15

A_e	$f_r \leq 1$											
0.15	0.3	0.4	0.5	0.8	0.82	0.83	0.85	0.9	0.93	0.95	0.97	1
	$f_r > 1$											
	1.01	1.05	1.1	1.15	1.2	1.5	1.6	2				

The second part of the simulations is performed for a higher A_e equal to 0.2 and the cases are distinguished according to the f_r values as in the Table (5-2) at the beginning of the next page.

Table 5-2 The f_r cases for A_e equal to 0.2

A_e	$f_r \leq 1$										
0.2	0.4	0.5	0.6	0.7	0.72	0.73	0.8	0.85	0.9	0.95	1
	$f_r > 1$										
	1.01	1.05	1.1	1.15	1.2	1.5	1.6	2			

The third part of the simulations is performed for constant f_r equal to 0.95 and variable A_e as presented in the Table (5-3) below

Table 5-3 The A_e cases for f_r equal to 0.95

f_r	A_e						
0.95	0.15	0.2	0.25	0.3	0.35	0.4	0.5

Only the cases of the Table (5-1) and (5-3) are presented in the following paragraphs. In general, as it will be shown in the next chapter the behaviour of the FSI system for the two different amplitudes of 0.15 and 0.2 is quantitively very similar as far as it concerns the force coefficients behaviour.

5.1 FoV cases of constant A_e and variable f_r

The lift and drag coefficients time history traces of the FoV study oscillation configurations are presented in the current paragraph. A transition period is apparent in the forces time series for all cases. During this period the flow adapts numerically and physically to the motion; the transition period T_a is measured as the number of oscillation periods T_o until a steady force pattern starts developing.

5.1.1 Fluid force coefficients

In all the cases the excitation amplitude acquires the same value 0.15D, the coefficients drag (green line) and lift (red line) are presented along with the harmonic oscillation displacement of

the cylinder (blue line). Finally, the adaptation time T_a is also presented for each case as a dashed grey line on the same diagram of the force coefficients time-series.

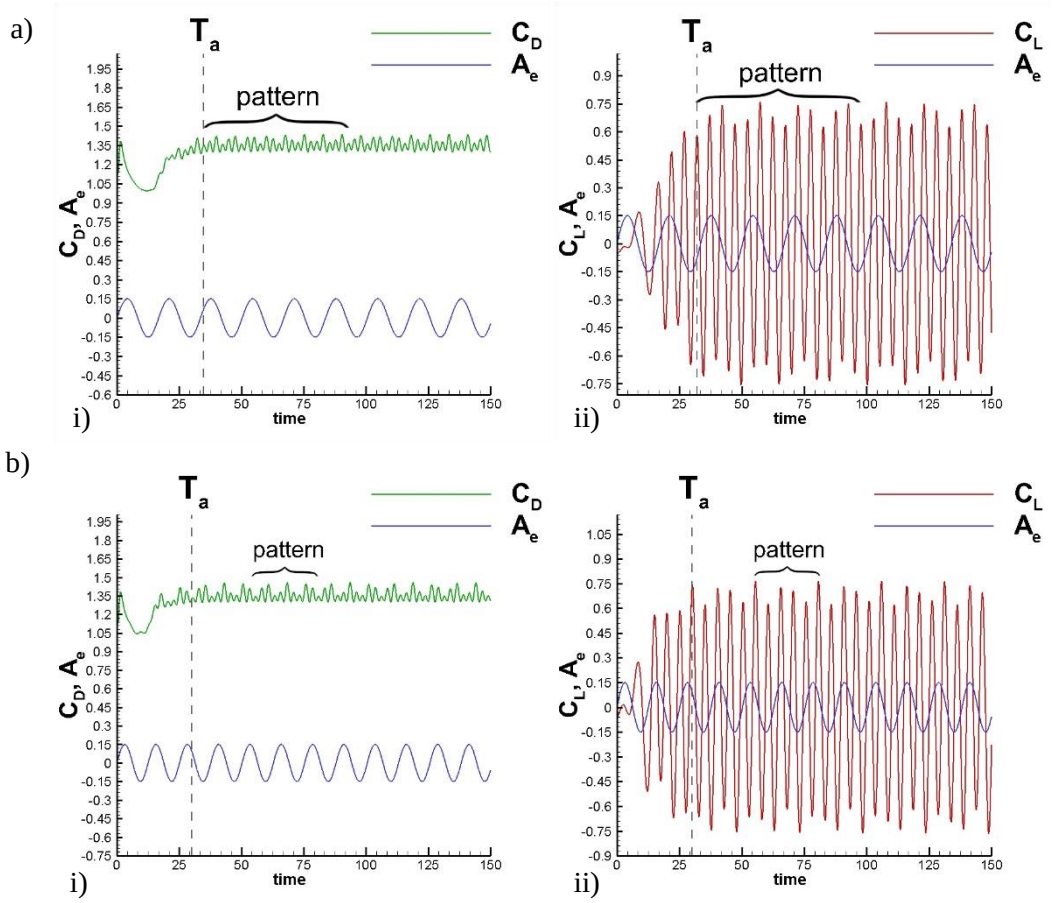

Figure 5-2 a)f_r=0.3, b) f_r=0.4 , i) lift and ii) drag coefficient time-series along with the harmonic oscillation displacement and adaptation period

In the first two cases (a) 0.3 and (b) 0.4 in the Figure (5-2) above, it is apparent that the lock-in has not occurred since the time-series consist of a combination of sinusoids that results in a complex pattern after the transition period is exceeded. The pattern is depicted with a horizontal bracket on top of the corresponding repeated part of the time-series, while the transition period can be observed to be approximately $2T_o$. In comparison to the stationary cylinder case the mean drag coefficient is decreased to the 86% of the stationary value while the lift is increased by 43% of its stationary value.

In the Figure (5-3) of the next page, the case of $f_r = 0.5$ harmonic motion is presented with the difference in comparison to the previous cases, that the forces have not yet converged to a steady pattern. It can be speculated that eventually there will be a long pattern appearing but due to the statistical independence that is sought for the study of the time-series e.g. for the FFT analysis of the next paragraph, it is computationally expensive to continue the current case simulation.

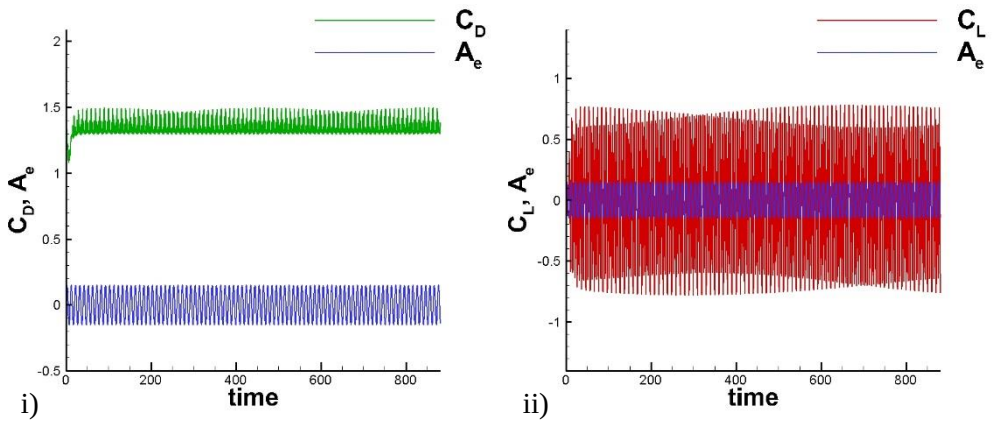

Figure 5-3 $f_r = 0.5$ i) lift and ii) drag coefficient time-series along with the harmonic oscillation displacement

In the Figure (5-4). below, the $f_r = 0.8$ case is presented. The $C_{Dmean}$is decreased by 3% and the C_{Lrms} is decreased by a 20% in comparison to the lower frequency cases of Figure 5-2 of page 86, while the T_a has increased to approximately $3T_o$. Comparing to the stationary cylinder cases the C_{Dmean} is decreased to 83% of the stationary value while the C_{Lrms} is increased by a 38% of the stationary value.

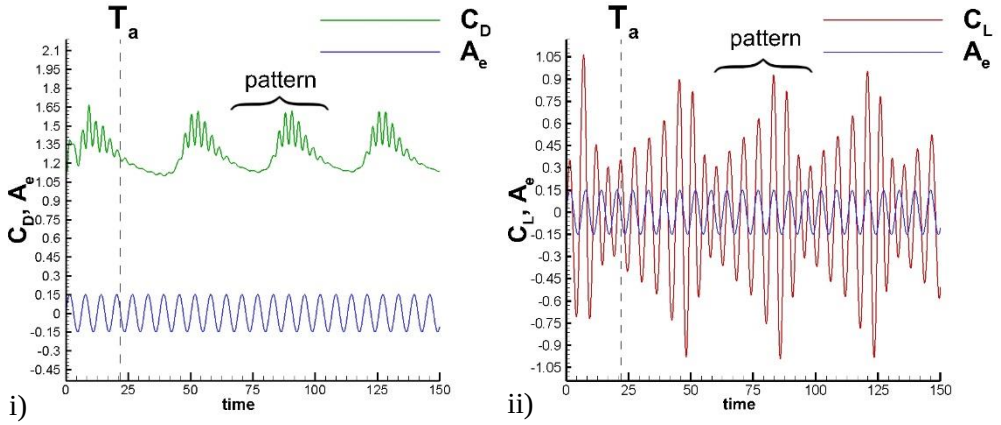

Figure 5-4 $f_r = 0.8$ i) lift and ii) drag coefficient time-series along with the harmonic oscillation displacement and adaptation period

The simulations so far have been performed in the non-lock-in region i.e. outside the area enclosed by the Koopmann curve of Figure (5-2) in page 86. The following cases cross the limit defined by the Koopman curve entering the lock-in region, resulting in a pure sinusoidal force coefficients time-series while the transient time is significantly increased in comparison to the lower frequency ratio cases.

In the case of Figure (5-5) below, the $f_r = 0.82$ case is presented. The C_{Dmean} is decreased by a 3% and the C_{Lrms} is decreased by a 25% in comparison to the previous case of Figure 5-4 of the previous page, while the $T_a$has significantly increased to approximately $11T_o$. In comparison to the stationary case, the C_{Dmean} is decreased to the 81.7% of the stationary value while the C_{Lrms} is decreased to the 34% of the corresponding stationary value.

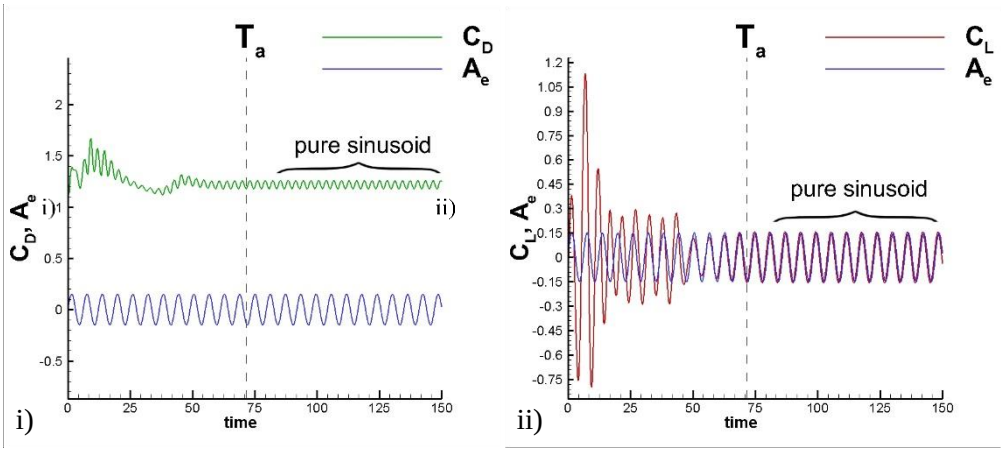

Figure 5-5 $f_r = 0.82$ i) lift and ii) drag coefficient time-series along with the harmonic oscillation displacement and adaptation period

In the Figure (5-6) below, the f_r acquires the value of 0.83. The C_{Dmean} is increased by a 0.5% and the C_{Lrms} is decreased by an 8% in comparison to the previous case while the T_a is similar to the previous case approximately $12T_o$. In comparison to the stationary case, the C_{Dmean} is decreased to the 82% of the stationary value while the C_{Lrms} is decreased to the 32% of the corresponding stationary value. For the time being the current case is considered to be the lower lock-in limit; a more extensive and detailed investigation of the lock-in limit is conducted later on in the discussion chapter, for the appropriate definition of the limit.

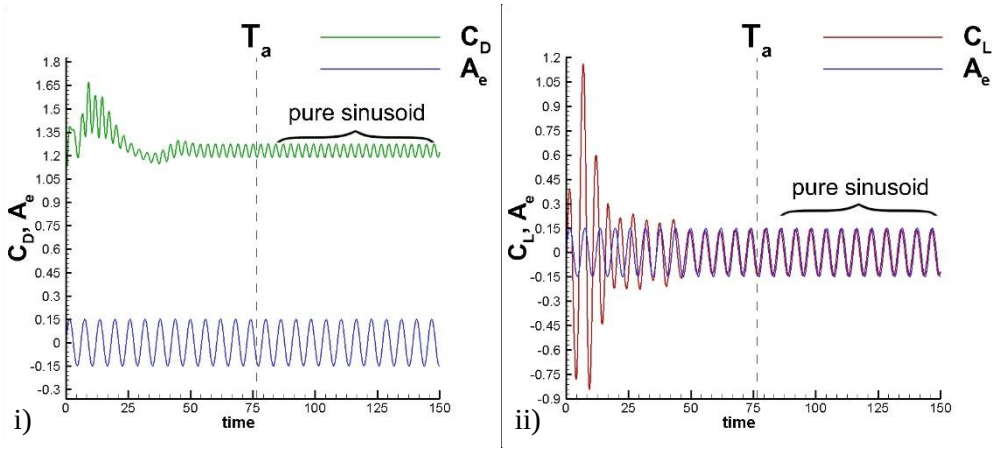

Figure 5-6 $f_r = 0.83$ i) lift and ii) drag coefficient time-series along with the harmonic oscillation displacement and adaptation period

In the Figure (5-7) below, increasing further the f_r to the value of 0.85 results in an increase of 9% of the C_{Dmean} and a decrease of 11% of the C_{Lrms} in comparison to the case $f_r = 0.83$ of the Figure (5-6) of the previous page, while the T_a maintains the number of oscillation periods at the same level as the previous two cases, approximately $13T_o$. The C_{Dmean} is decreased to the 83% and the C_{Lrms} is decreased to the 28% of the corresponding stationary values.

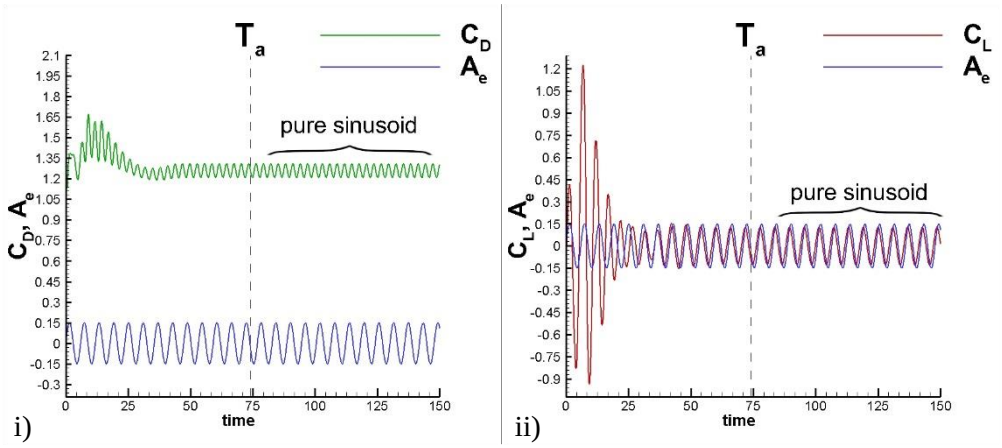

Figure 5-7. Case of $f_r = 0.85$ i) lift and ii) drag coefficient time-series along with the harmonic oscillation displacement and adaptation period

In the Figures (5-5), (5-6) and (5-7) another characteristic of the interaction can also be observed, that is the phase difference between the forces and the displacement; it is more convenient to observe the lift coefficient time-series. In the case of $f_r = 0.82$ and 0.83, the phase difference is very small as the time-series of the lift and the harmonic oscillation displacement almost coincide, rather in the case of Figure (5-7) the phase difference is increased as the lift time-series shift away from the harmonic oscillation displacement. The phase difference plays an important role in FoV studies and it will be presented in the following chapter.

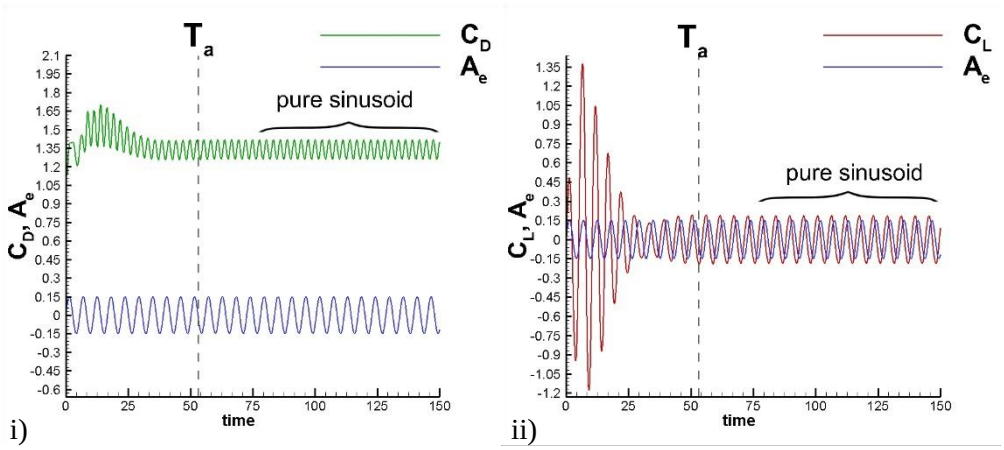

Figure 5-8 $f_r = 0.9$ i) lift and ii) drag coefficient time-series along with the harmonic oscillation displacement and adaptation period

In the Figure (5-8)of the previous page, the case of $f_r = 0.9$, an increase of 3% of the C_{Dmean} and 47% of the C_{Lrms} in comparison to the case $f_r = 0.85$ of the Figure (5-7) of the previous page is estimated. The C_{Dmean} is decreased to the 85% and the C_{Lrms} is decreased to 41% of the corresponding stationary values. The T_a is reduced in comparison to the case of $f_r = 0.85$ to approximately $10T_o$. In the Figure (5-9) below, the case of $f_r = 0.93$ is presented. An increase of 2% of the C_{Dmean} and 58% of the C_{Lrms} in comparison to the case $f_r = 0.9$ of the Figure (5-8), of the previous page, is estimated, while the T_a is increased in comparison to the case of $f_r = 0.9$ to approximately $15T_o$. The C_{Dmean} is decreased to the 87% and the C_{Lrms} is decreased to the 66% in comparison to the stationary values.

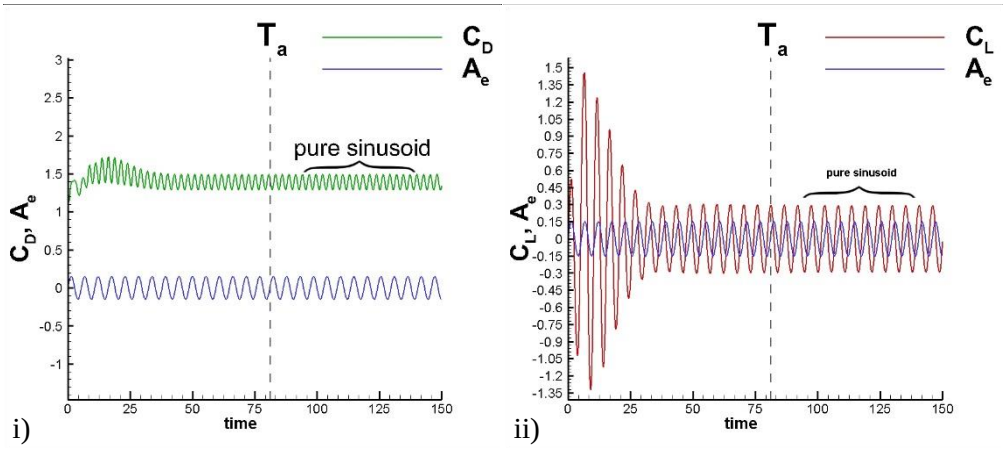

Figure 5-9 $f_r = 0.93$ (i) drag and (ii) lift coefficient time-series along with the harmonic oscillation displacement and adaptation period

In Figure (5-10) below, the f_r is increased to the value of 0.95. An increase of 1.4% of the C_{Dmean} and 32% of the C_{Lrms} in comparison to the case $f_r = 0.93$ of the Figure (5-9) above is estimated while the T_a is increased to $20T_o$. The C_{Dmean} is decreased to the 88% and the C_{Lrms} is decreased to the 88% of the corresponding stationary values.

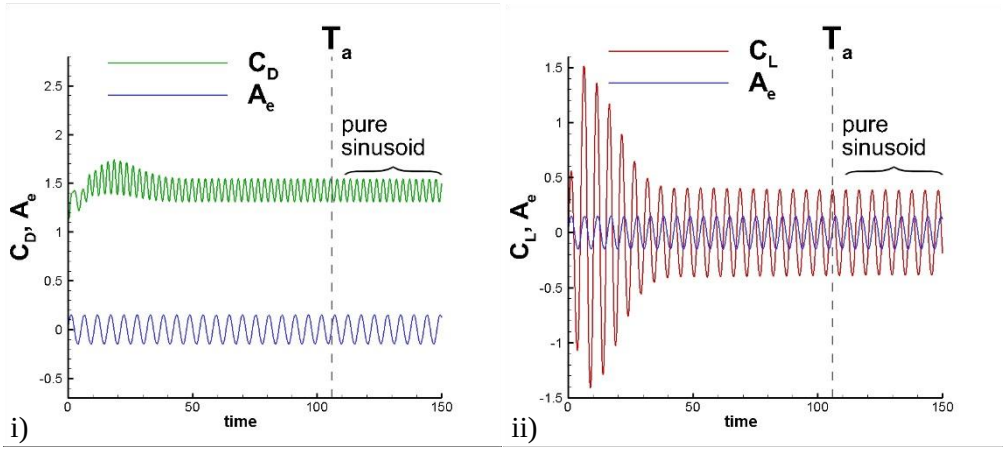

Figure 5-10 $f_r = 0.95$ (i) drag and (ii) lift coefficient time-series along with the harmonic oscillation displacement and adaptation period.

The case of Figure (5-11) below, presents the lift and drag coefficients time-series for the frequency ratio of 97% of the stationary Strouhal frequency. an increase of 1.25% of the C_{Dmean} and 28% of the C_{Lrms} in comparison to the case $f_r = 0.95$ of the Figure (5-10) above is estimated while the T_a is increased in comparison to the case of $f_r = 0.95$ of the Figure (5-11) to approximately $28T_o$. The C_{Dmean} is decreased to the 90% and the C_{Lrms} is increased to the 113% of the corresponding stationary case values.

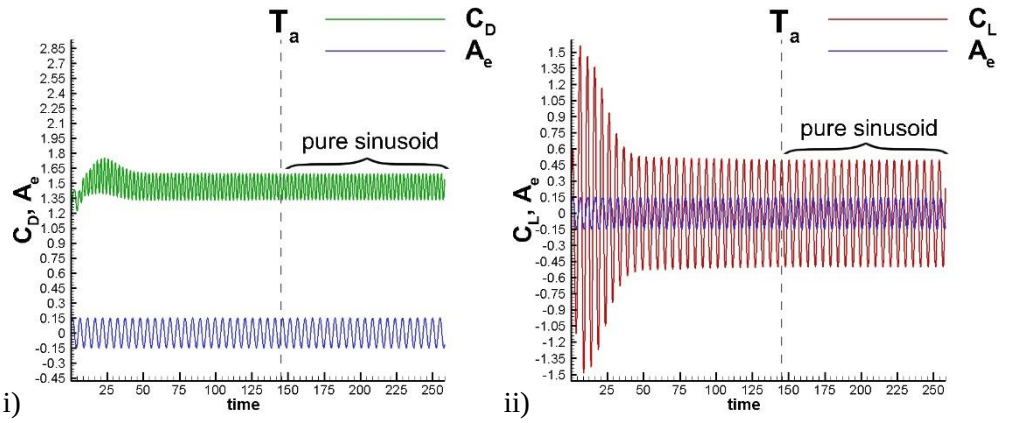

Figure 5-11 $f_r = 0.97$ (i) drag and (ii) lift coefficient time-series along with the harmonic oscillation displacement.

In the case of Figure (5-12) below presents the lift and drag coefficients time-series for the frequency ratio of unity i.e. 100% of the stationary St frequency value. An increase of 1.4% of the C_{Dmean} and 32% of the C_{Lrms} in comparison to the case $f_r = 0.95$ of the Figure (5-11) above is estimated, while the T_a is increased to $40T_o$.The C_{Dmean} is decreased to the 91% and the C_{Lrms} is increased by 62% of the corresponding stationary values.

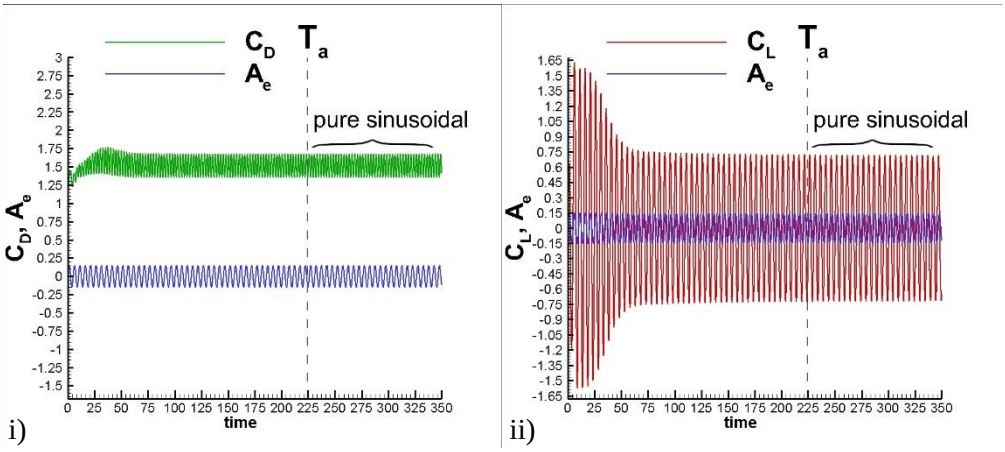

Figure 5-12 $f_r = 1$ (i) drag and (ii) lift coefficient time-series along with the harmonic oscillation displacement.

The cases presented so far belong to the lower than unity frequency ratio region, non-lock-in or lock-in, the presentation of results will now proceed with the cases where the frequency ratio is higher than unity.

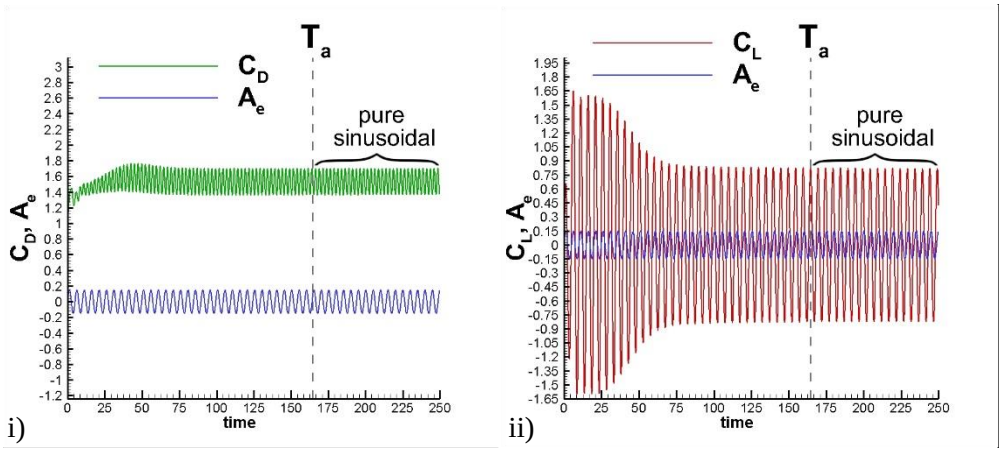

Figure 5-13 $f_r = 1.01$ (i) drag and (ii) lift coefficient time-series along with the $A_e = 0.15$

In the case of Figure (5-13) above the f_r is slightly increased to the value of 1.01. The C_{Dmean} presents a slight increase by 1% while the C_{Lrms} is increased by 2% in comparison to the case of $f_r = 1$ of the Figure (5-12) on top of the page is estimated. The C_{Dmean} is decreased to the 91% of the stationary values and the C_{Lrms} is increased by 86% of its stationary value. The T_a is decreased in comparison to the case of $f_r = 1$.

In the following case of Figure (5-14) below, the lock-in is not present as it is in the lock-in cases presented so far. Although as it will be seen in the following paragraph, where the spectral analysis will be presented the excitation freqeuncy is still dominant in both coefficients which according to the literature review it is considered lock-in even if there are other frequency components present. Recall that the upper lock-in range presents differences in the lock-in conditions than the lower lock-in region.

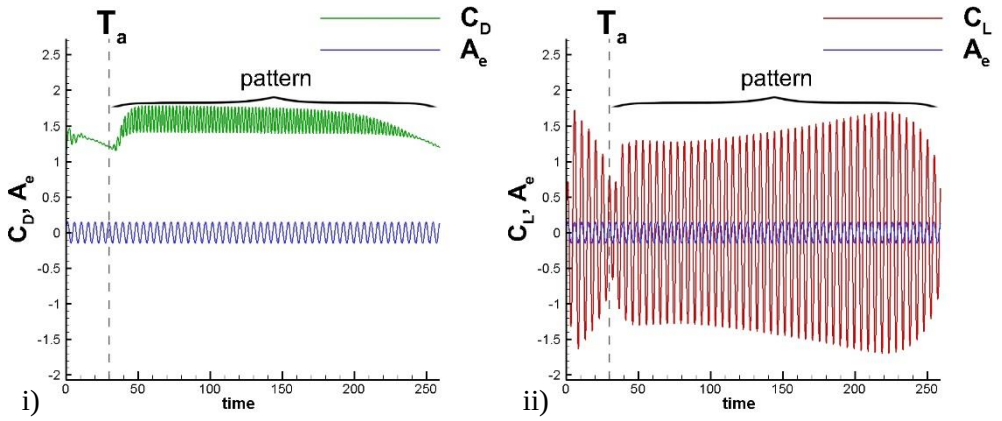

Figure 5-14 $f_r = 1.05$ (i) drag and (ii) lift coefficient time-series along with the harmonic oscillation displacement

The f_r is increased to the value of 1.05 in Figure (5-14) of the previous page, the C_{Dmean} presents a slight decrease by 1% while the C_{Lrms} is largely increased by 71% in comparison to the case $f_r = 1$ of the Figure 5-13 of the last page is estimated, while the T_a amounts to a few oscillation periods, approximately $5T_o$. The C_{Dmean} is decreased to the 91% and the C_{Lrms} is largely increased to the 320% of the stationary values. As it can be observed in the case of Figure (5-14) above, the characteristic of the pure sinusoidal time-series is lost, it must be also stretched that the upper lock-in limit has not yet been located, a more detailed step study for the frequency ratio is presented in the following chapter.

An increase of the frequency ratio to the value of 1.1 results in the diagrams of the Figure (5-15) below. The C_{Dmean} presents a slight decrease by 3%, while the C_{Lrms} is increased by 6% in comparison to the case $f_r = 1.05$ of the Figure (5-14) of the previous page, while the T_a amounts to approximately $4T_o$. The C_{Dmean} is decreased to the 91% and the C_{Lrms} is largely increased to the 320% of the corresponding stationary values.

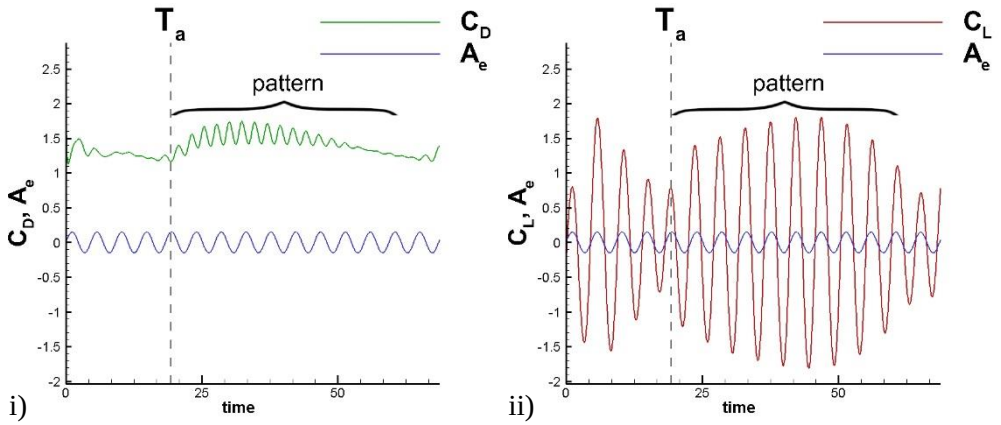

Figure 5-15 $f_r = 1.1$ (i) drag and (ii) lift coefficient time-series along with the oscillation displacement and the adaptation time

Further increase of the f_r to the value of 1.15 presented in the Figure (5-16) of the next page results in a slight decrease of 1% of the C_{Dmean}, the C_{Lrms} is increased by 3% in comparison to the previous case $f_r = 1.1$ of the Figure (5-15), while the T_a amounts to less than four oscillation periods. The C_{Dmean} is decreased to the 88% and the C_{Lrms} is largely increased to the 350% of the corresponding stationary values.

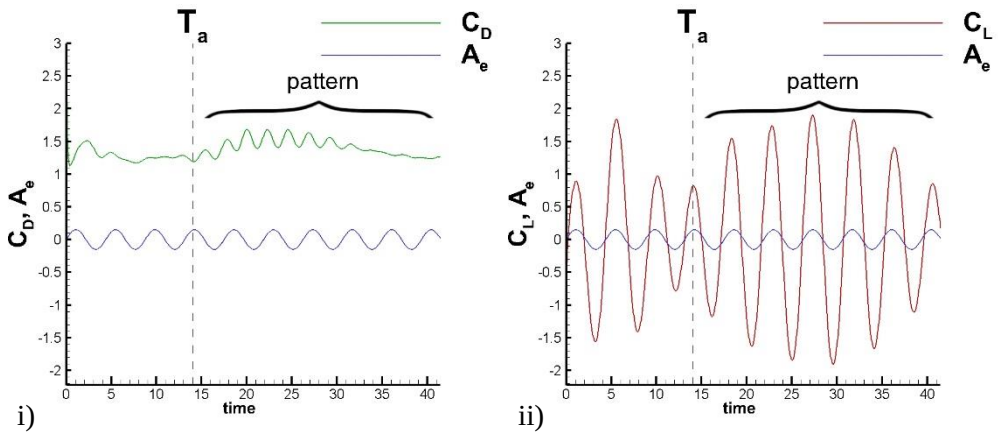

Figure 5-16 $f_r = 1.15$ (i) drag and (ii) lift coefficient time-series along with the oscillation displacement and the adaptation time

Further increase of the f_r to the value of 1.2, Figure (5-17) below. The C_{Dmean} and the C_{Lrms} present very similar to the previous case of Figure 5-17 behaviour, a slight decrease by 1% and an increase of 3% in comparison to the case $f_r = 1.15$ of the Figure (5-16) above is estimated, the T_a amounts to less than three oscillation periods. The C_{Dmean} is decreased to the 88% and the C_{Lrms} is largely increased to the 360% of the stationary values.

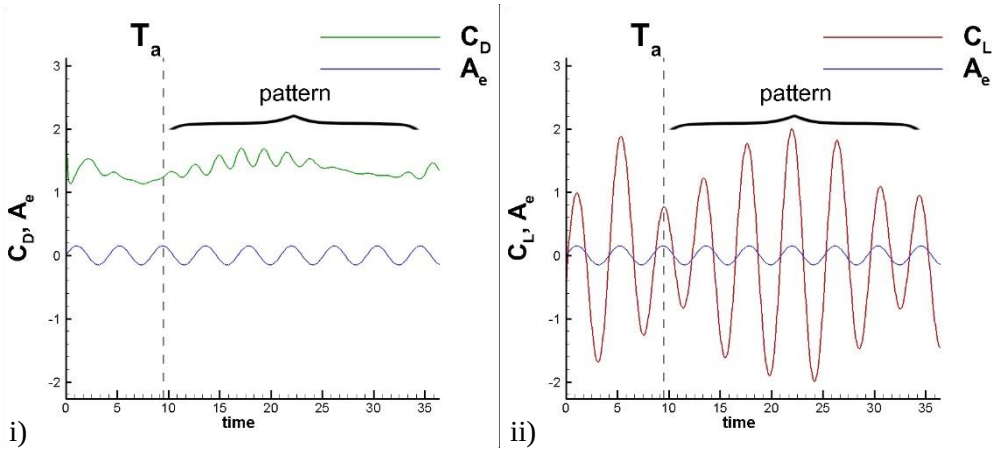

Figure 5-17 $f_r = 1.2$ (i) drag and (ii) lift coefficient time-series along with the oscillation displacement and the adaptation time

The upper lock in limit of $+20\%$St is now exceeded. A further increase of the f_r to the value of 1.5 in Figure (5-18) of the next page does not alter the C_{Dmean} , the C_{Lrms} presents an increase of 34% in comparison to the case of the Figure (5-17) above, while the T_a amounts to less than two oscillation periods. The C_{Dmean} is decreased to the 86% and the C_{Lrms} is largely increased to the 485% of the corresponding stationary values.

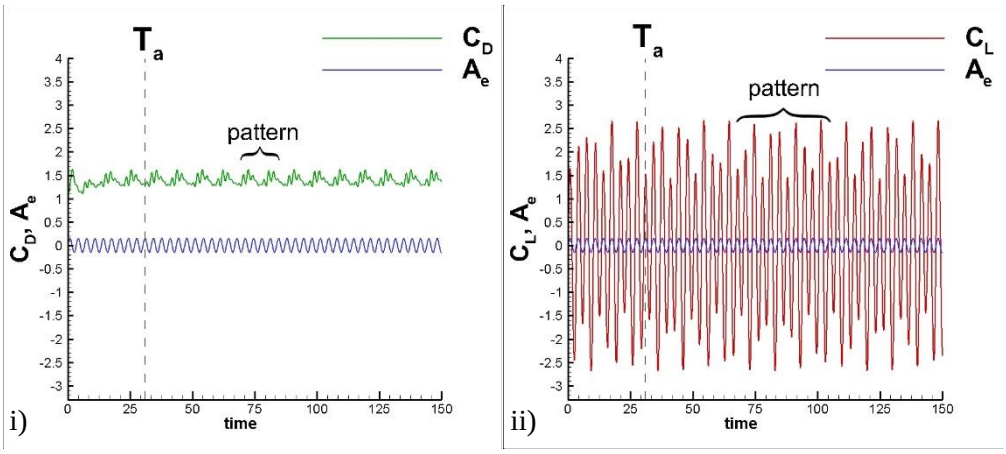

Figure 5-18 $f_r = 1.5$ (i) drag and (ii) lift coefficient time-series along with the oscillation displacement and the adaptation time

In contrast to the lower non-lock-in region the lift coefficient is largely increased in comparison to the stationary values and the lock-in values as well. The results are summarized and discussed in the following chapter in an attempt to define the behaviour of the force coefficients regarding the motion effect.

Further increase of the f_r to the value of 1.6 results in the Figure (5-19) below. The C_{Dmean} increases by 2%and the C_{Lrms} presents an increase of 34 % in comparison to the case of the Figure 5.18 above is estimated, the T_a amounts to less than two oscillation periods. The C_{Dmean} is decreased to the 89% and the C_{Lrms} is largely increased to the 530% of the corresponding stationary values.

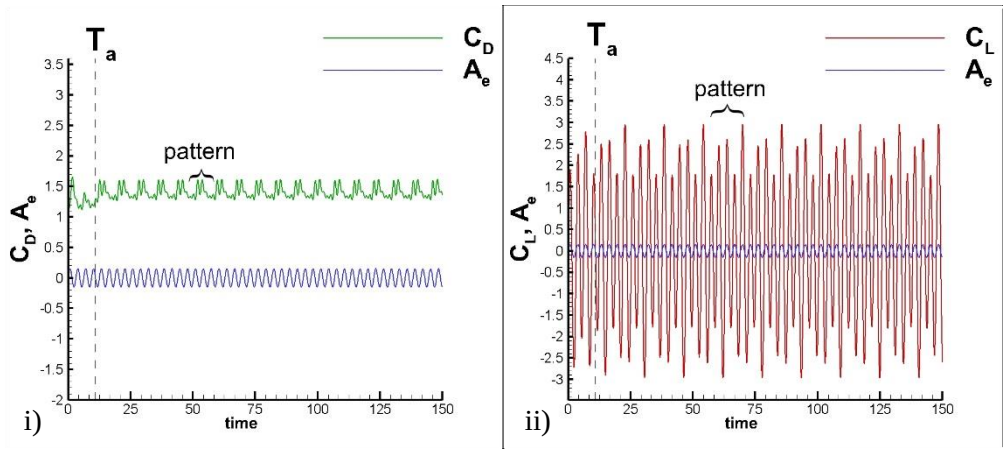

Figure 5-19 $f_r = 1.6$ (i) drag and (ii) lift coefficient time-series along with the oscillation displacement and the adaptation time

Finally, the study is completed with the case of Figure (5-20) of the next page, where the excitation frequency obtains the value of double the St frequency. The C_{Dmean} increases by 10%, the C_{Lrms} presents an increase of 40 % in comparison to the case of the Figure (5-19) of the

previous page is estimated while the T_a amounts to approximately $4T_o$. The C_{Dmean} is decreased to the 90% and the C_{Lrms} is largely increased to the 788% of the corresponding stationary values.

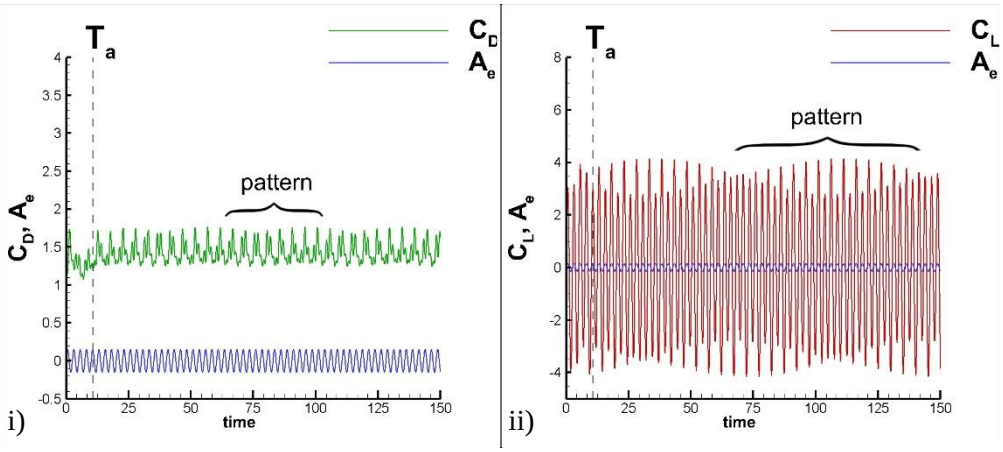

Figure 5-20 $f_r = 2$ (i) drag and (ii) lift coefficient time-series along with the oscillation displacement and the adaptation time

The previous results concentrated on the time-series quantitative description and the rough definition of the non-lock-in and lock-in regions. The limits of the lock-in region where approximately defined and a comparison of the statistical values of the force coefficients in comparison to the stationary case values was presented.

The study is now moving to the FFT analysis as it was applied to the preceding results of the force coefficients time-series. The spectral analysis reveals qualittative and quantitative characteristics of the behaviour of the force coefficients in the non-lock-in and lock-in regions.

5.1.2 The Force coefficients spectra

The previous paragraph emphasised on the quantitative description of the simulations results on the fluid force coefficients time-series. It is natural to describe the time-series through their spectral variables of frequency and amplitude, the FFT analysis reveals the force coefficients spectral components and their spectral characteristics; the components that are multiples of the St frequency or the excitation frequency will be referred to as St or excitation components correspondingly. The frequency is normalised with the excitation frequency, so the reader can instantly observe the existence or not of the lock-in to the excitation frequency; the actual spectral variables' values are depicted in the brackets above the corresponding peaks.

Commencing the FFT description with the Figure (5-21) of the next page, the case of $f_r = 0.3$ force coefficients spectra can be observed. The drag coefficient consists of three spectral components in the transformed domain. The highest spectral amplitude corresponds to the St

component while the other two peaks correspond to components that appear solely due to the interaction, although it can be easily observed that the oscillation or the double of the oscillation frequency with values 0.0597 and 0.1194 correspondingly, do not appear in the drag spectra but only in the lift.

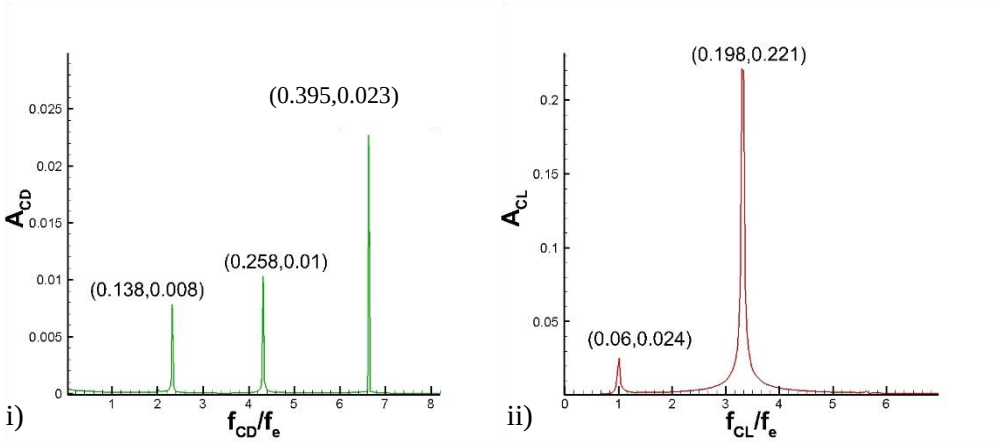

Figure 5-21 Spectra of (i) drag and (ii) lift coefficients for harmonic motion of f_r=0.3

It can also be observed that amongst the three frequencies of the C_D, the one corresponding to the value of 0.258 is the difference of the third highest with value at 2St (equal to 0.398) and the lowest spectral amplitude component with value 0.138. As far as it concerns the C_L, it can be observed that the only components appearing are the St and the excitation components. For both coefficients the highest spectral amplitude component is the St component revealing that the wake flow is not locked-in to the excitation frequency and it is still dominated by the stationary vortex shedding; the extra components appearing due to the interaction are of small spectral amplitude in comparison to the St components, one order of magnitude difference causing only a disturbance to the shedding process.

Increasing the f_r to the value of 0.4, increases the spectral amplitude (the second number of the pairs in the brackets) of both the excitation and the St components for both force coefficients, observe the Figure (5-22) in the next page, in comparison to the Figure (5-21) above. The number of spectral components appearing in the current case FFT analysis, is the same as the previous case of $f_r = 0.3$. The dominant component in the drag spectra is still the St- component for both coefficients revealing that the vortex shedding is still dominated by the stationary characteristics. The excitation component appears only for the lift coefficient while it is absent in the drag coefficient. For the last coefficient the same characteristic with the previous case can be observed; the small frequency component is the difference of the St and the excitation component.

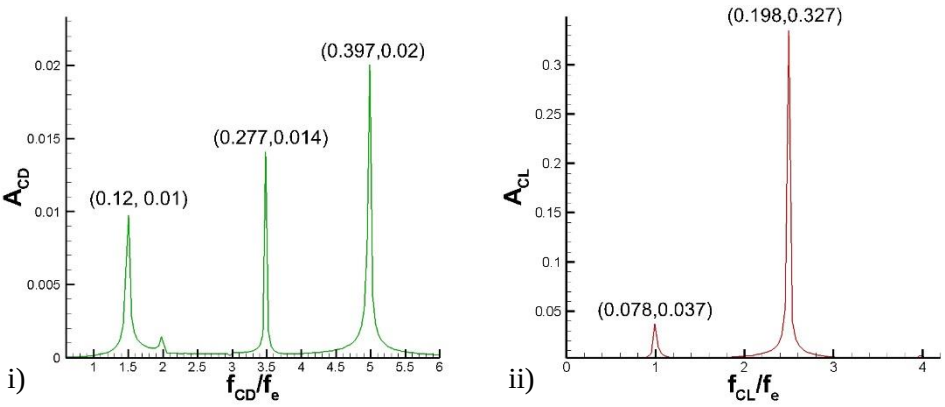

Figure 5-22 Spectra of (i) drag and (ii) lift coefficients for f_r=0.4

In the Figure (5-23) below, the f_r is increased to the value of 0.8; it must be underlined that the frequency ratio is now in the vicinity of the lock-in range of frequencies (20-30%St). In comparison to the lower f_r cases of Figure (5-21) of the last page and of Figure (5-22) above, a multiple of more than two or three spectral components is manifesting for both force coefficients.

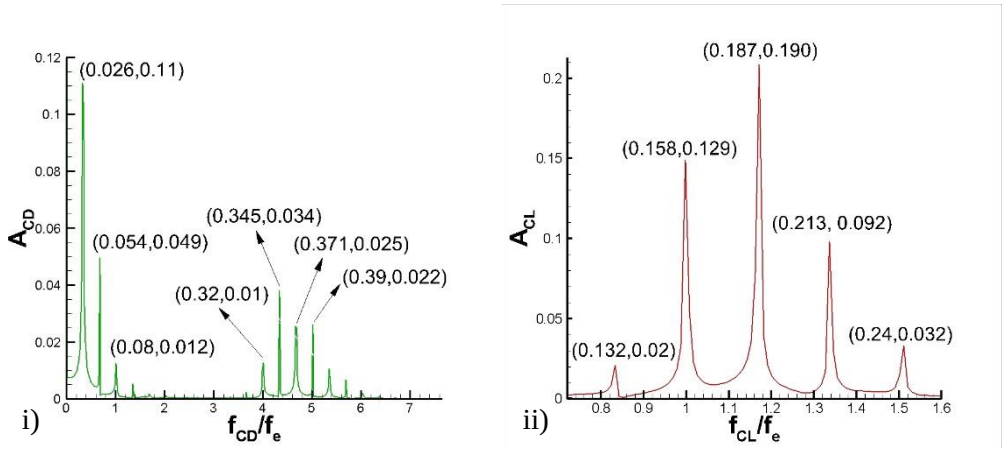

Figure 5-23 Spectra of (i) drag and (ii) lift coefficients for f_r=0.8

The highest spectral amplitude component that appears in the C_D spectrum of Figure (5-24) (i), in the next page, appears to be a very small frequency component of value equal to 0.026; it can be observed that the small frequencies can be regarded as the difference of higher frequency components e.g. the pairs of (0.371,0.345) and (0.39,0.371). In the C_L spectrum of Figure (5-24) (ii), the excitation component has significantly increased spectral amplitude in comparison to the previous lower frequency ratio cases; although it must be underlined that the dominant components in Figure (5-24) are neither the St component nor the excitation component in contrast to the earlier cases where the dominant component was the St frequency. It can also be observed that the difference between two consecutive peaks' amplitudes is the same for all pairs. The lift coefficient also presents a stronger excitation component while the St component does not appear in the spectrum.

In the cases that follow the FSI system has reached the lock-in criteria with the vortex shedding frequency acquiring the excitation frequency; recalling the pure sinusoidal form of Figures (5-5) to (5-13) of the previous paragraph the corresponding force coefficients spectrums present a single peak corresponding solely to the excitation frequency. What there is to be observed apart from the single peak, is the spectral amplitude that is increasing with the frequency ratio assigning a resonance characteristic to the cases distinguishing the lock-in cases to a resonance and non-resonance region.

The first two cases of the lock-in region are presented below in the Figure (5-24) (a) $f_r = 0.82$ and (b) $f_r = 0.83$. inititally it can be observed that the drag coefficient presents a single frequency that is the double of the excitation frequency and the lift presents the excitation frequency, the aforesaid leads to the conclusion that the vortex shedding does not experience any alterations due to the motion and has re-established the traditional vortex-shedding as in the stationary cases. Despite the lock-in conditions that occur, the amplitude for both coefficients is very small.

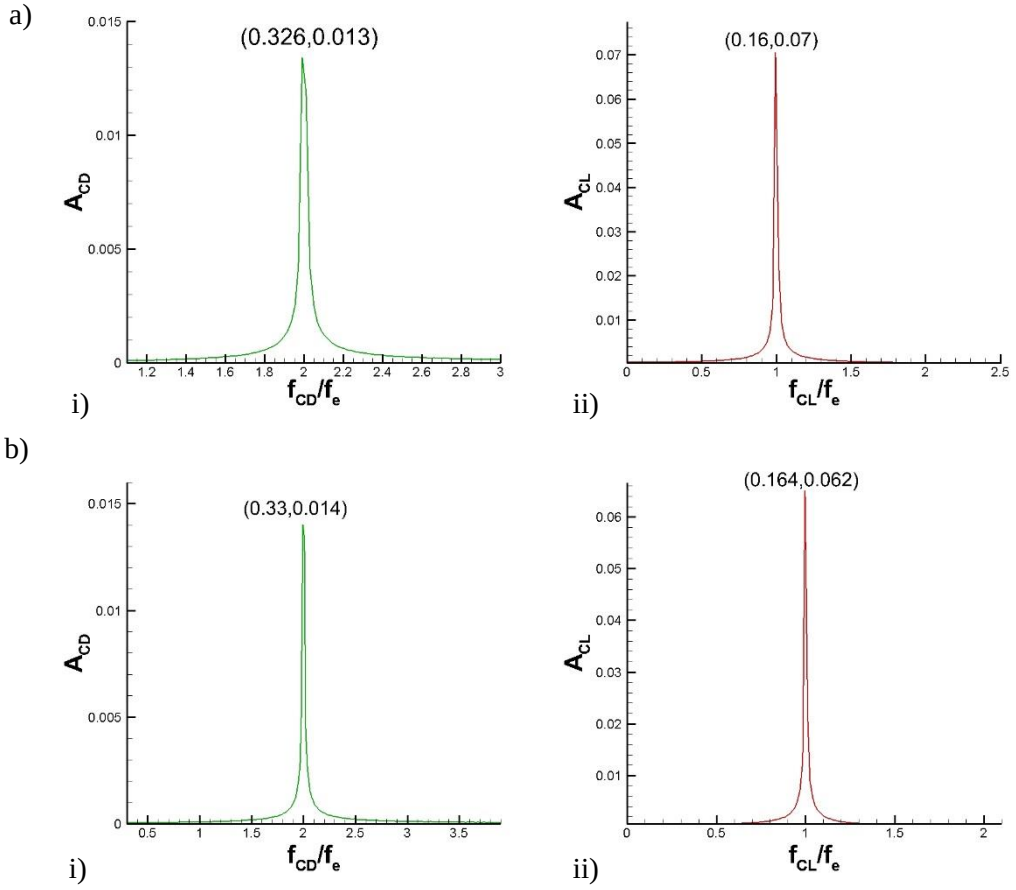

Figure 5-24 Spectra of (i) drag and (ii) lift coefficients for f_r equal to a) 0.82, b) 0.83

In Figure (5-25) of the next page, the force coefficient spectra for the cases of $f_r = 0.85$ and 0.9 can be observed, the drag spectral amplitude is increased approximately double in comparison to

the previous cases of Figure (5-24) of the previous page while the lift coefficient does not show any significant change in comparison to the previous cases.

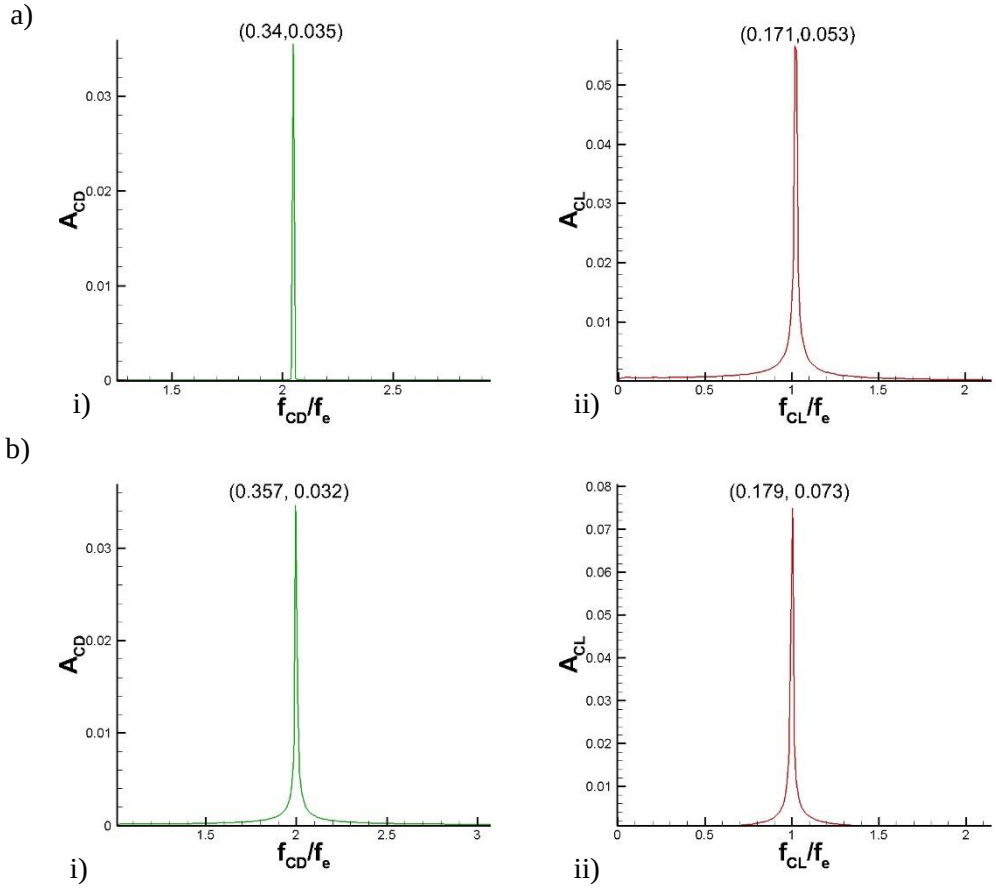

Figure 5-25 Spectra of (i) drag and (ii) lift coefficients for f_r equal to a)0.85 and b)0.9

The traditional vortex shedding characteristic of the drag frequency being the double of the lift frequency can be clearly observed, although the resonance cannot be observed yet. In the case of $f_r = 0.93$ of the Figure 5-26 below the resonance is observed with the spectral amplitude of both force coefficients being increased

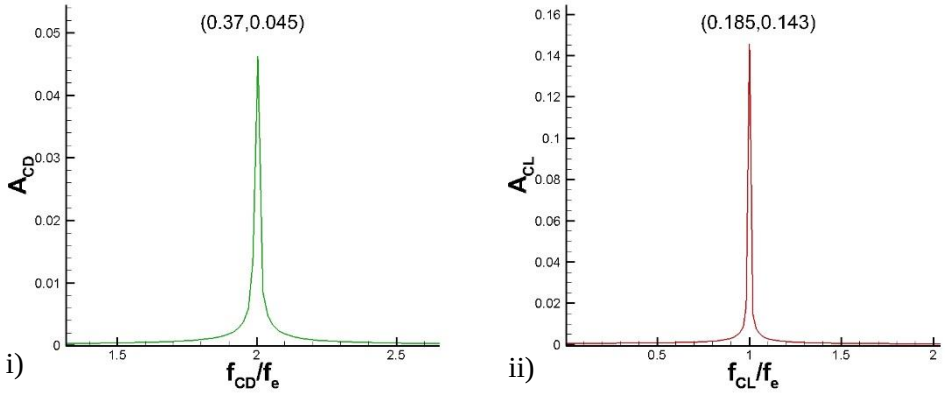

Figure 5-26 Spectra of (i) drag and (ii) lift coefficients for f_r equal 0.93

In the figure (5-27) below the spectra of the force coefficients for the cases of *a)* f_r*=0.95* and b)0.97 can be observed.

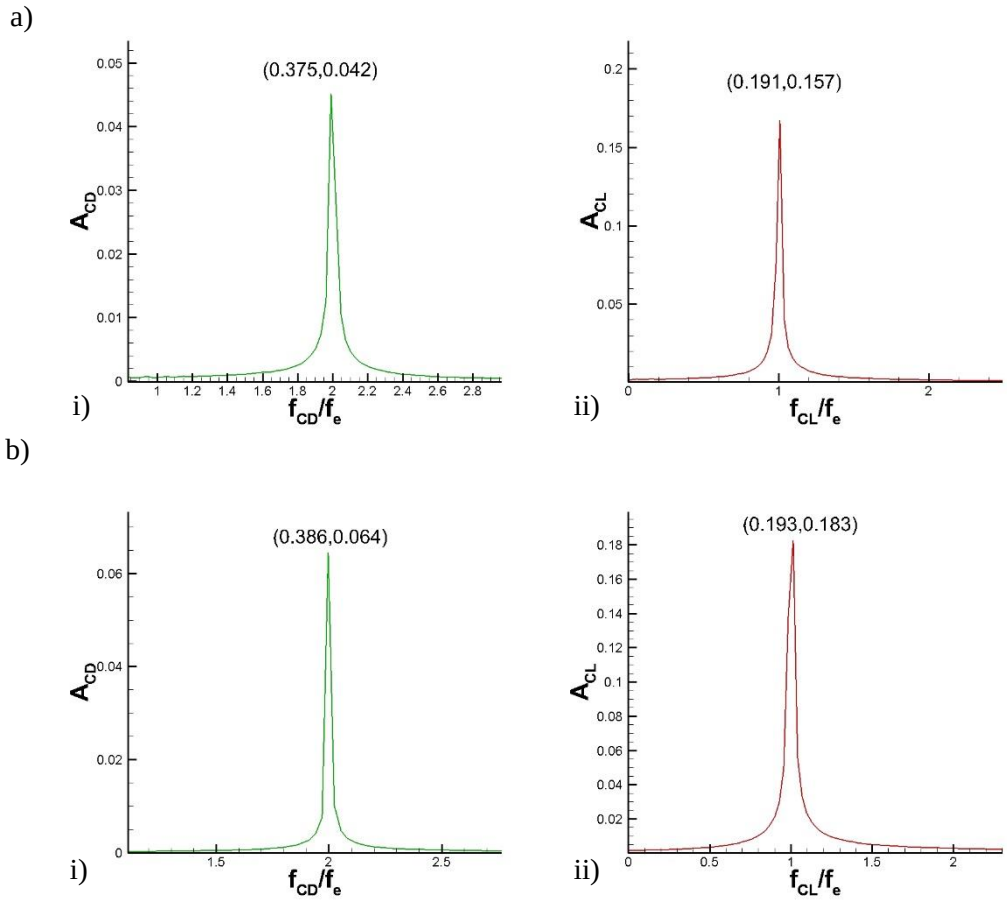

Figure 5-27 Spectra of (i) drag and (ii) lift coefficients for a) f_r***=0.95, b)0.97.***

The increasing spectral amplitude of the lift can be observed while the drag initially, for the case of f_r*=0.95,* maintains the amplitude almost at the same value as in the case of Figure (5-26); it increases when the frequency ratio increases to the value 0.97 of Figure (5-27) (b). the resonance is further enhanced when the frequency ratio reaches the unity , observe the Figure (5-28) below.

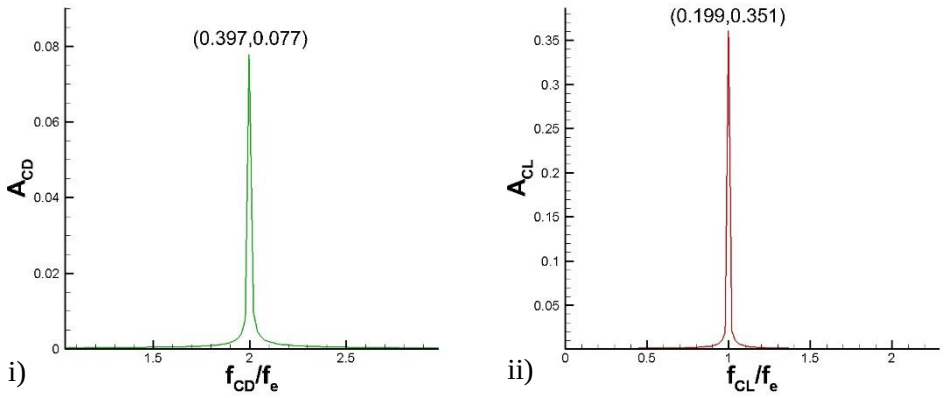

Figure 5-28 Spectra of (i) drag and (ii) lift coefficients for f_r***=1.***

In the Figure (5-29) below the unity frequency ratio is surpassed entering the upper lock-in region; the lift coefficient amplitude increases further, the spectral amplitude of the drag is decreased, therefore the resonance limit is the unity frequency ratio of the Figure (5-28) of the previous page.

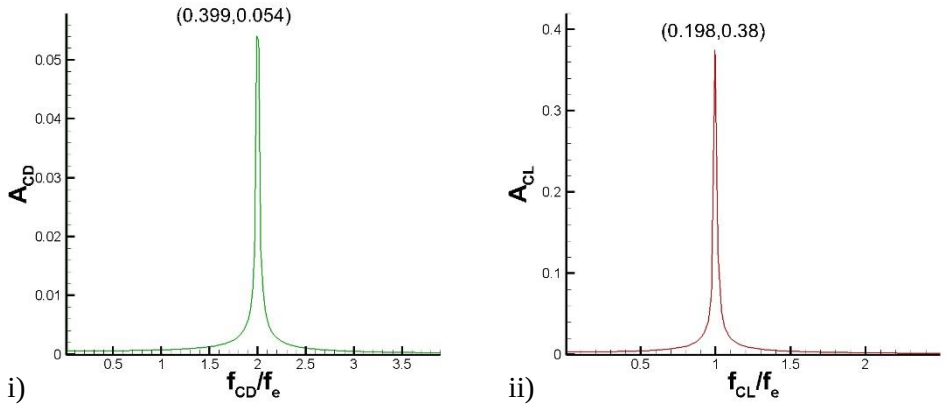

i) ii)

Figure 5-29 Spectra of i) drag and ii) lift coefficients for f_r=1.01

Increasing further the f_r, reduces drastically the spectral amplitude for both coefficients while more frequencies re-appear signifying the end of the lock-in region, observe the Figure (5-30) below. Despite the reappearance of more frequencies it can be observed that some characteristics of the lock-in region survive with the dominant frequency being that of the excitation frequency, while the spectral amplitude of the lift is increasing to higher values than the earlier lock-in cases.

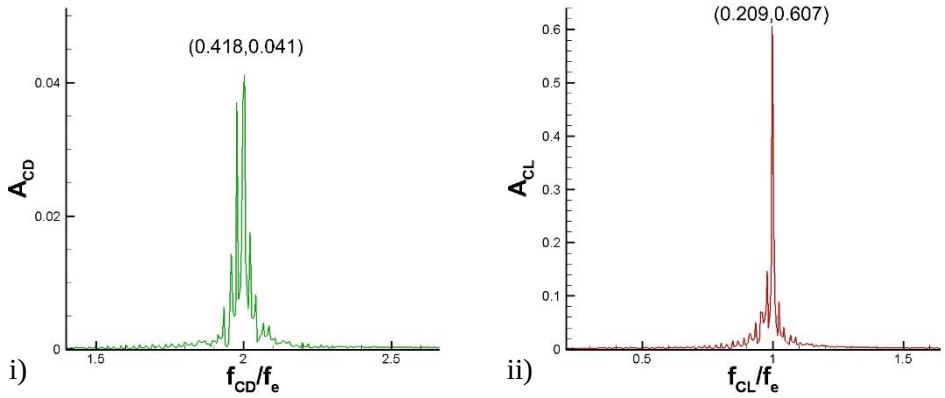

i) ii)

Figure 5-30 Spectra of i)drag and ii) lift coefficients for f_r=1.05

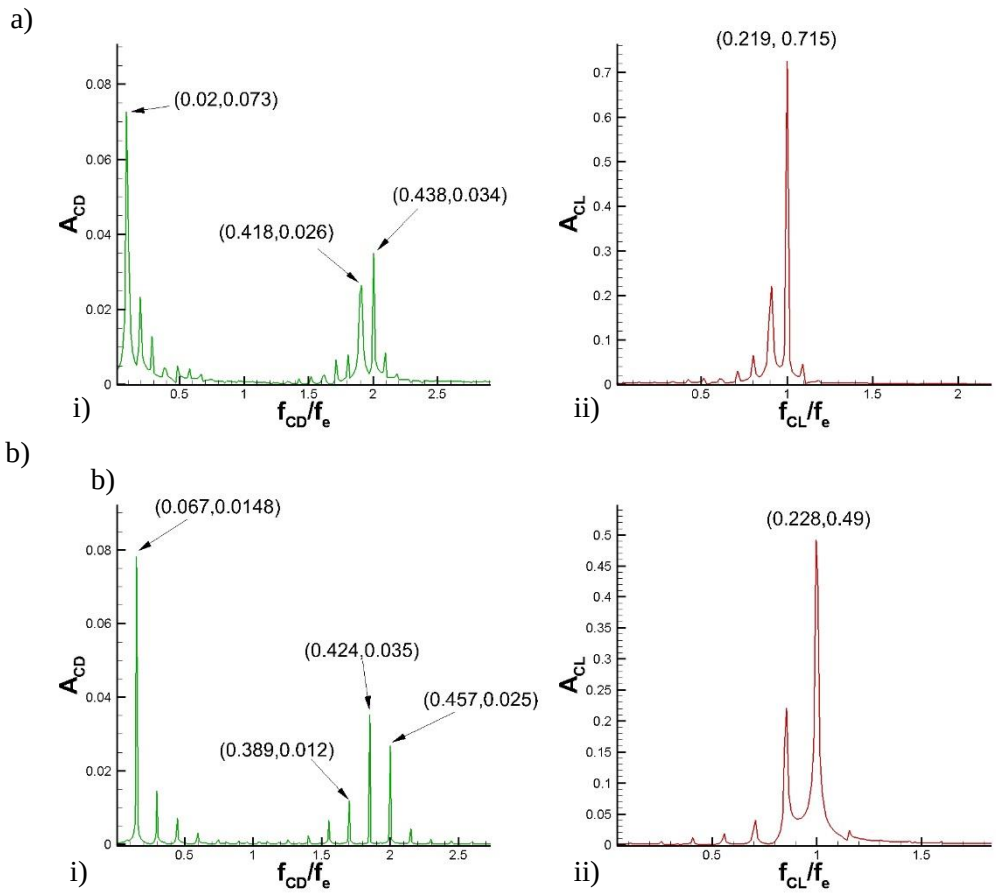

Figure 5-31 Spectra of (i) drag and (ii) lift coefficients for a) $f_r = 1.1$, b) $f_r = 1.15$

In Figure (5-31) above, (a) and (b) for the cases of $f_r = 1.1$ and $f_r = 1.15$ correspondingly, the force coefficients spectra are presenting more components, similarly to the lower non-lock in region before the lower lock-in limit, the dominant frequency of the drag coefficient is a low frequency that is the difference of higher frequencies as in Figure (5-23) in page 96. In comparison to the lower non-lock-in region the spectral amplitudes of the components are much higher. For the lift coefficient the dominant frequency is still that of the excitation frequency in contrast to the lower non-lock-in region where the dominant frequency was neither the St nor the excitation frequency.

In Figure (5-32) of the next page, for the last four cases of the study, the excitation frequency ceases to be the dominant frequency but in contrast to the lower non-lock-in region the St frequency does not appear in the upper region in either force coefficient.

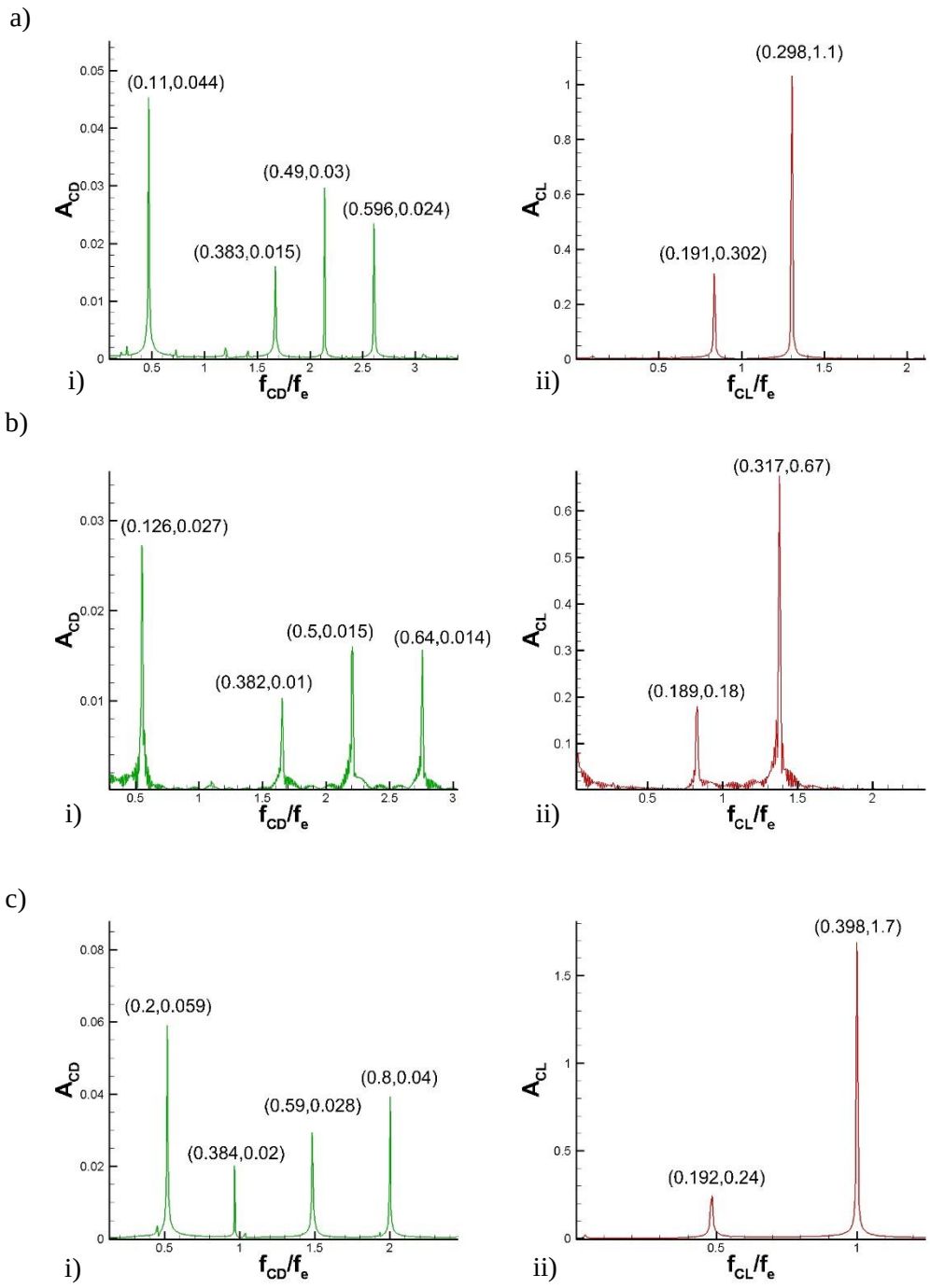

Figure 5-32 Spectra of i)drag and ii)lift coefficients for a) $f_r = 1.2$***, b)*** $f_r = 1.5$***, c)*** $f_r = 1.6$***, d)*** $f_r = 2$

The presentation of the results will continue with the cases of constant frequency ratio and variable amplitude. The frequency ratio is a constant located in the lock-in region while the amplitude is increased to higher values.

5.2 Variable amplitude cases with constant frequency ratio

The present paragraph concentrates on the description of the coefficient time series as these resulted from the simulations of FoV with constant frequency ratio of value 0.95, inside the expected lock-in region of the neighbourhood of 20%-30% of the St frequency, and variable amplitude.

5.2.1 Lift and Drag coefficients time-series

The first case of oscillation characteristics ($f_r = 0.95, A_e = 0.15$) has already been described in the previous paragraph 5.1.1. in the Figure (5-33) a) Maintaining the f_r and increasing the A_e to the value of 0.2D results in a reduction of the T_a to 12 oscillation periods. The C_{Daver} is increased by 2% and the C_{Lrms} is increased by 2% in comparison to the lower amplitude case of 0.15.

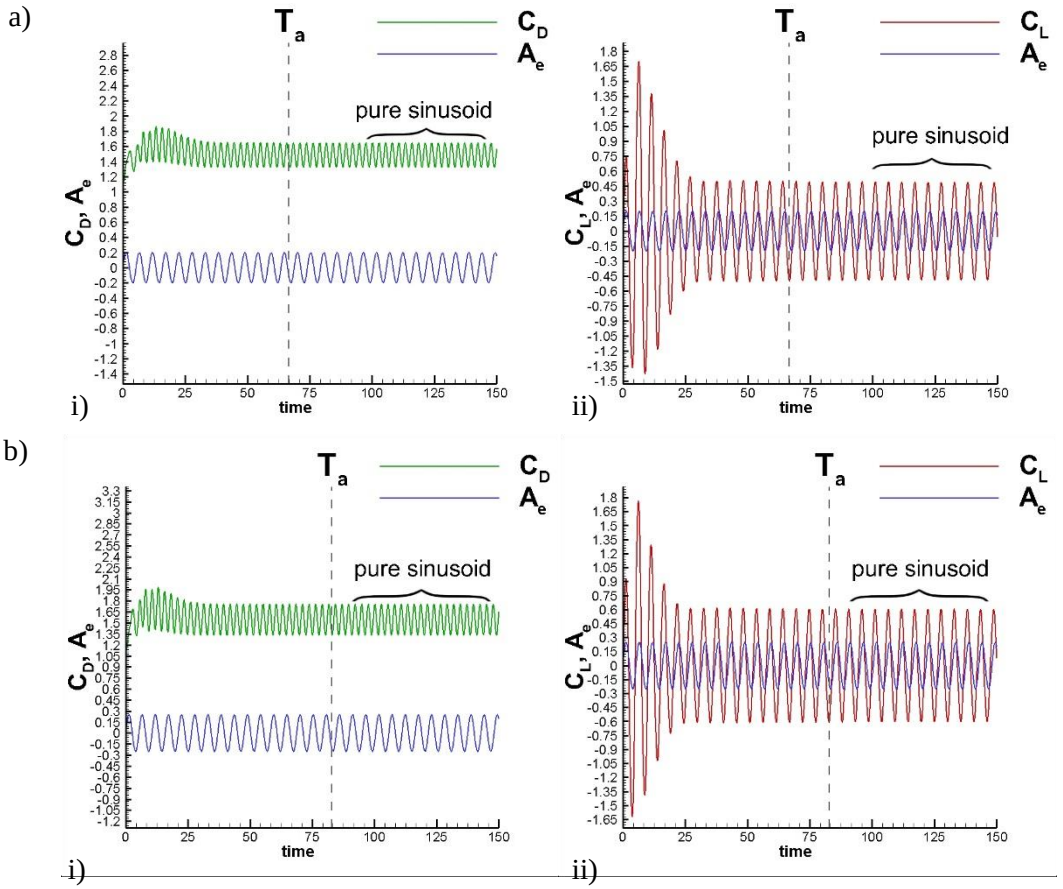

Figure 5-33 Amplitude cases of a) $A_e = 0.2$ and b) $A_e = 0.25$, for (i) drag and (ii) lift coefficient time-series along with the oscillation displacement

In the second part of the last page Figure (5-33) b), the time-series of the force coefficients for $A_e = 0.25$ are presented. The T_a has increased to 15 oscillation periods, the C_{Daver} is increased by 1.6% and the C_{Lrms} is increased by 21% in comparison to the lower amplitude case of 0.2.

The amplitude of the oscillation is further increased to the value of 0.3D resulting in the force coefficient time-series of the Figure (5-34) below. The T_a has increased to 28 oscillation periods, the C_{Daver} is increased by 2.4% and the C_{Lrms} is significantly increased by 80% in comparison to the lower amplitude case of 0.25.

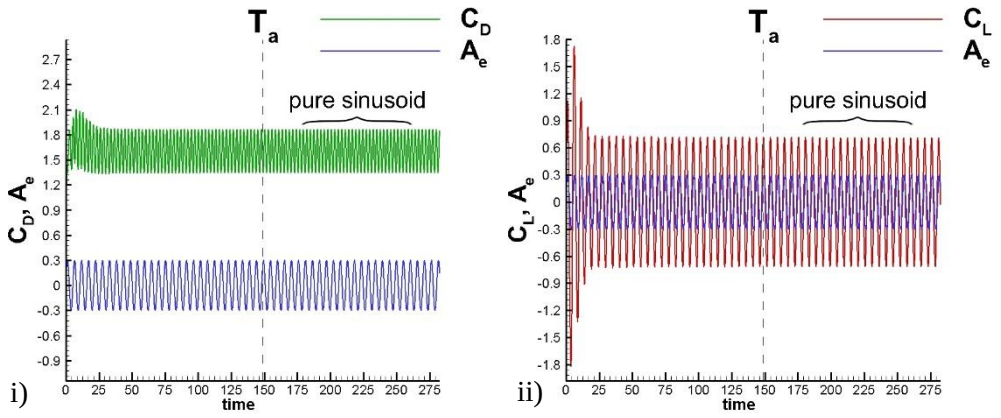

Figure 5-34 $A_e = 0.3$ (i) drag and (ii) lift coefficient time-series along with the oscillation displacement

The amplitude of the oscillation is further increased to the value of 0.35D resulting in the force coefficient time-series of the Figure (5-35) below. The T_a has decreased to 13 oscillation periods, the C_{Daver} is increased by 1.6% and the C_{Lrms} is decreased by 25% in comparison to the lower amplitude case of 0.3 above.

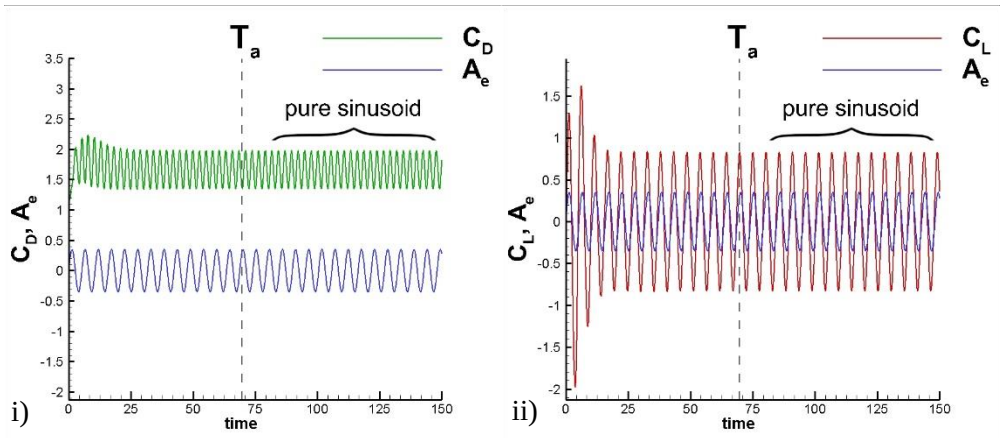

Figure 5-35 $A_e = 0.35$ (i) drag and (ii) lift coefficient time-series along with the oscillation displacement

The amplitude of the oscillation is further increased to the value of 0.4D resulting in the force coefficient time-series of the Figure (5-36) below. The T_a is increased to 22 oscillation periods, the C_{Daver} is increased by 1.6% and the C_{Lrms} is increased by 14% in comparison to the lower amplitude case of 0.35.

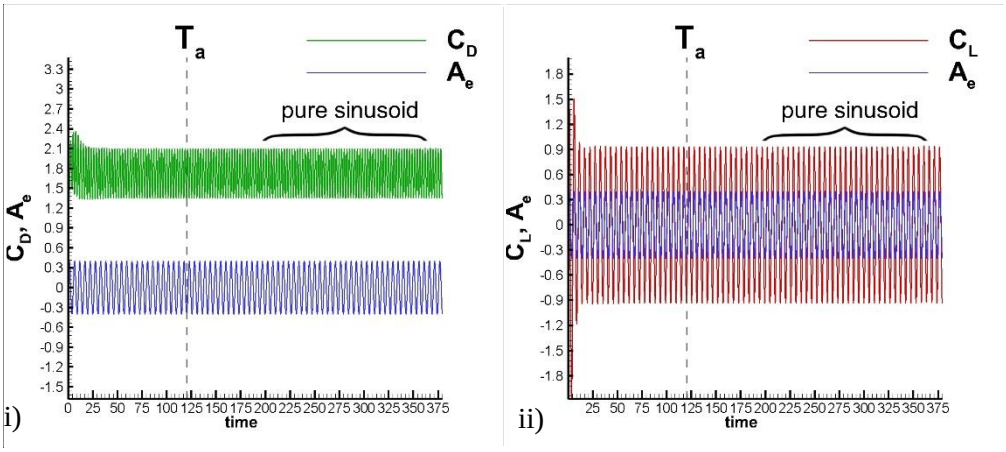

Figure 5-36 $A_e = 0.4$ (i) drag and (ii) lift coefficient time-series along with the oscillation displacement

The amplitude of the oscillation is further increased to the value of 0.5D resulting in the force coefficient time-series of the Figure (5-37) below. The T_a is increased to 22 oscillation periods, the C_{Daver} is increased by 1.6% and the C_{Lrms} is increased by 14% in comparison to the lower amplitude case of 0.35.

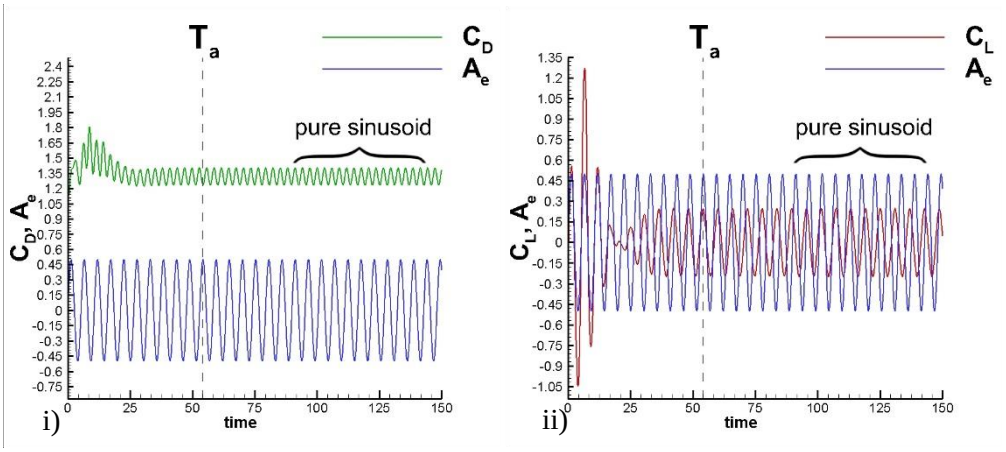

Figure 5-37$A_e = 0.5$ (i) drag and (ii) lift coefficient time-series along with the oscillation displacement

5.3 Summary

The present chapter presented the initial results for the FoV cases for a cylinder harmonically vibrating on a direction transverse to the flow. The main flow variables investigated are the force coefficients namely drag and lift with the independent variable being the excitation frequency and amplitude. Mainly a quantitative analysis was conducted with the time-series and their FFT analysis being employed for a better understanding of the interaction between the motion of the cylinder and the flow around the cylinder. The studies concentrated on both the lock-in and non-lock-in regions as were defined by Koopman's observation on the vibration frequency region being 20-30% of the St frequency. For the amplitude of the harmonic motion the cases emphasized on amplitudes larger than 0.1D since according to the literature review this is the limit so the wake of the cylinder is substantially affected by the motion. The study cases were distinguished to variable frequency and constant amplitude and inversely variable amplitude and constant lock-in frequency. The description was presented following the path in the order of lower-non-lock-in, lower lock-in, upper lock-in and upper non-lock-in region as defined in the Figure 2-2 (page 34) around the unity frequency ratio.

In the first case, for the non-lock-in regions the interaction of the flow with the cylinder's motion presents a complex pattern for the time-series of the lift and drag coefficients that through the FFT analysis is due to a multiple of spectral components that appear due to the interaction. In general, the frequencies of the components acquire values of the St or the oscillation frequency and differences between them; it was observed that either the oscillation or the St frequency were absent is some cases in either the lift or the drag spectrum. Moreover, when the excitation frequency is not in the neighbour region of the lock-in limits the number of spectral components is reduced in comparison to the higher frequency ratios; the spectral amplitude of the Fourier components is increasing as the frequency approaches the lock-in region.

In the lock-in region, a single component appears for both force coefficients with the distinctive characteristic of Benard-Karman street vortex shedding appearing as in stationary cases; namely the drag obtains a frequency that is the double of the lift frequency that in turn acquires the excitation frequency value. Furthermore, it is observed that the lock-in region can be further subdivided to resonant and non-resonant lock-in regions, these are the immediate regions of the limit of the lock-in region where the wake is locked-in but the force coefficients present a decreased amplitude and the immediate region of the unity frequency ratio where the force coefficients are significantly increased to at least one order of magnitude greater values.

In the upper lock-in region, as soon as the frequency ratio exceeds the 1.02 value the lock-in ceases to exist returning to the non-lock-in characteristic of multiple spectral components; although the resonant characteristics do not vanish with the coefficient values being increased further to higher values than the lower non-lock-in or lock-in regions.

As far as it concerns the case with variable amplitude and constant frequency, a lock-in frequency was selected since this is the region of interest in the ViV studies; recall that FoV is employed as an alternative approach to understand ViV phenomena. The amplitude varied from 0.15D to 5D; it can be concluded that the lock-in conditions were not affected by varying the amplitude inside the lock-in region while the force coefficients did not present a specific trend that changes with the amplitude.

Finally the results for constant $A_e = 0.2$ and variable frequency were not included in the present chapter as the behaviour was very similar to the $A_e = 0.15$ case; a summary of the $A_e = 0.2$ cases will be presented in the following chapter.

6 Discussion

The phenomenon of lock-in that occurs when the cylinder is oscillating in unison with the vortex shedding has been extensively investigated for various amplitudes and frequencies in FoV and various structural configurations in ViV. It is of great importance to be able to define the limits of the lock-in region. as it was observed in the previous chapter the initial results showed that inside the lock-in region due to the synchronization the force coefficients under study appear to be single sinusoidal functions of time thus the conditions of the FSI are clearly defined. Outside the lock-in region the time series are a combination of sinusoids with frequencies that appear due to the cylinder's motion that changes the flow conditions on the circumference of the cylinder.

The present chapter is summarising the initial results and presents a discussion on issues and phenomena that occur. A validation in comparison with other studies will be presented at first place to verify the appropriateness of the algorithm to investigate FSI phenomena. Secondly, the previous chapter study suggests that the lock-in limits regions should be further investigated to enhance the understanding of the transition to the lock-in region. A new set of cases that emphasise on the limit regions will be presented for a constant amplitude and variable frequency; a smaller step is employed to vary the frequency around the limit region. The results and conditions on the limit between the lock-in and non-lock-in regions are not clarified yet to have a specific characteristic that occurs for the different FoV configurations; it is generally acknowledged that at the limit the wake acquires the oscillating frequency. The results of the previous chapter emphasised on the description of the simulations results on the force coefficients time-series and their FFT analysis.

Moreover, the suitability of the algorithm to investigate FSI cases through FoV is investigated presenting results on the energy coefficient and the phase between the cylinder's harmonic motion and the force coefficients.

Finally, a Netwon polynomial is constructed to represent the drag coefficient and the lift coefficient amplitudes in the lock-in region.

6.1 Review of results and comparison with past studies

The current paragraph is employing results from past studies in an attempt to validate the algorithm. In the Figure (6-1) (i) below, the present thesis case on the harmonic oscillation characteristics are presented along with the results obtain from the study of (MadaniKermani 2014). The time-series, as these were obtained from a lock-in case, of the drag (green) and the lift (red) are in a fairly good agreement with the results of MadaniKermani Figure (6-1) (ii) (drag (blue), lift (red)). Although it can be observed that for the first timesteps of the algorithm were the computational time is below twenty the present algorithm exaggerates the computed values while the lift coefficient presents a decreased amplitude. The last discrepancy can be assigned to the different methodology employed by MadaniKermani who employs a two-dimensional algorithm for the study of FoV and FSI phenomena; according to observations for low amplitudes cases, the discrepancies between computed values of forces in two and three dimensional flows can be ignored (Peppa et al. 2015) and the difference can be assigned to the different computational methods employed for the solution of the Navier-Stokes equations. The drag coefficient is in a very good agreement with MadaniKermani's results.

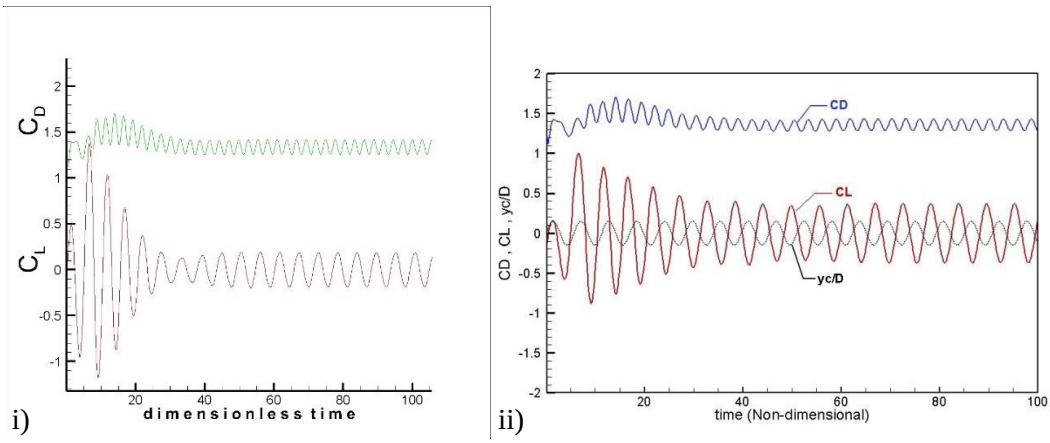

Figure 6-1 comparison of studies for $A_e = 0.15$ and $f_r = 0.9$, i) present study ii)(MadaniKermani 2014)

In the Figure (6-2) of the next page, a comparison is attempted for a non-lock-in case, in particular the case with oscillation characteristics ($A_e = 0.2, f_r = 0.9$); the case is compared with the study of (Tang et al. 2016). It can be observed that the time-series for both studies present a combination

of sinusoids pattern that is very similar in shape. The lift coefficient Figure (6-2) (a) (red line) presents again an increased amplitude while the drag Figure (6-2) (a) (green line) is in excellent agreement with the past study Figure (6-2) (b) (blue line).

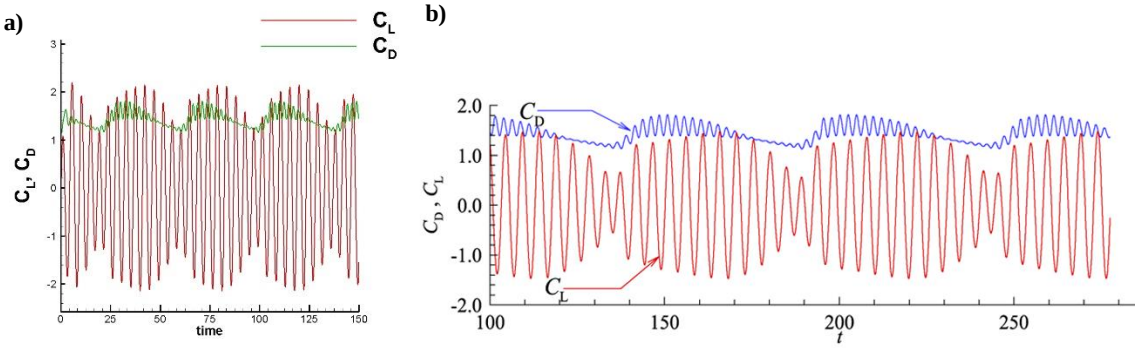

Figure 6-2 comparison of studies for $A_e = 0.2$ and $f_r = 1.1$, a) present study b) (Tang et al. 2016)

The comparison so far has presented a good agreement as far as it concerns the shape of the time-series of the force coefficients, a fact that assigns a good suitability characteristic for the current algorithm.

The comparison continues with the review of the average values of both force coefficients, namely C_{Dmean} and C_{Lrms}, for both excitation amplitudes of 0.15 and 0.2, employing once more the studies of (Tang et al. 2016).

In comparison to the stationary cases in Figure (6-3) of the next page, maintaining the amplitude constant and varying the frequency ratio reduces the mean drag coefficient to 82-91% of the stationary value, while the r.m.s. values of the C_{Lrms} depend on the region of the frequency ratio and vary from 0.06% to 190% of the stationary value for the $A_e = 0.15$ and from 0.12% to 250% of the stationary value for the $A_e = 0.2$ cases.

Observing Figure (6-3) below, (a) C_{Dmean} and (b) C_{Lrms}, in the unlocked region (left of the lower lock-in limit) both of the coefficients appear to attain a constant value independently of the amplitude or the frequency of the oscillation; recalling from the spectral analysis results of the last chapter, the dominating frequency in the lower non-lock-in region is the Strouhal frequency with the oscillating frequency appearing at a much smaller spectral amplitude component. While approaching the lock-in region the values of both of the force coefficients start diminishing; at the first limit line, entering the lock-in region the C_L and C_{Dmean} reach their lowest value. Entering the lower lock-in region the values of both coefficients are increasing. In the upper lock-in region the behaviour of the two coefficients is substantially different with the C_{Lrms} following the same trend as in the lower lock-in region thus increasing, but the C_{Dmean} starts diminishing; the mean drag reaches a local minimum at the right lock-in limit (right grey line) while C_{Lrms} reaches a local maximum at the same limit line. Outside the lock-in region on the right-hand side of the

upper limit lock-in limit, the C_{Lrms} is drastically increasing reaching the highest value at $f_r = 2$ while the mean drag increases at a slower rate reaching a local maximum at $f_r = 2$. Furthermore, it can be observed that the behaviour of the average values of the coefficients follow the same trend independently of the oscillation's amplitude, a fact that assigns the frequency ratio a more deterministic effect on the flow phenomena.

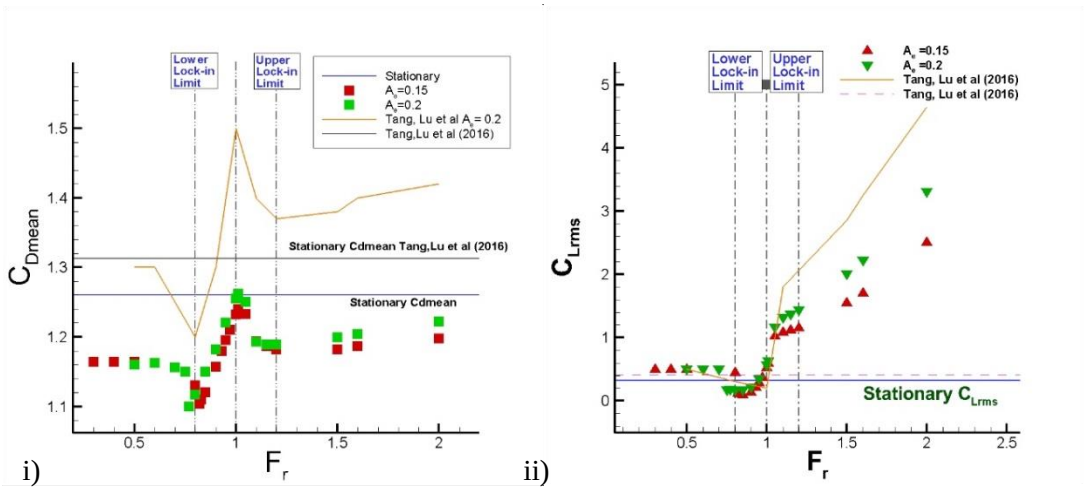

Figure 6-3 i) Mean drag coefficient and ii) average rms lift coefficient for constant amplitude and variable frequency ratio (Re=200)

Although the C_{Lrms} is in a very good agreement with the study of (Tang et al. 2016) the C_{Dmean} appears diminished. It can be observed that the present study stationary C_{Lrms} value is in good agreement with the value of Tang, Lu et al rather the C_{Dmean} appears reduced.

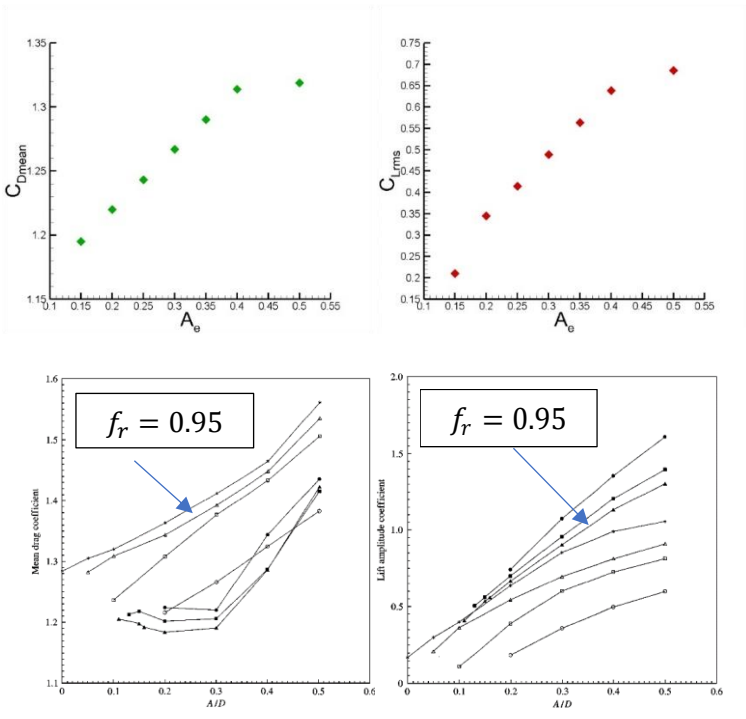

Figure 6-4 a)Mean drag coefficient (i) and average rms lift coefficient (ii) for constant frequency $f_r = 0.95$ and variable amplitude (Re=200) b) results of (Anagnostopoulos 2000)

It is understood that the stationary cases values affect the FoV results as far as it concerns the proximity of the resulting values although the overall trend is very similar for both studies, a fact that makes the FoV force coefficients behaviour for varying frequency ratio almost independent of the stationary values.

Figure (6-4) (a) (i) and (ii) of the previous page, reveals that for constant frequency the oscillation amplitude magnifies the mean drag and rms values of the lift coefficient. The second part of the Figure (6-4) (b) presents the results of Anagnostopoulos (2000); the trend of the force coefficients is in a good agreement.

In the aforementioned analysis the forces were examined through the forces magnitude perspective that revealed some characteristics of the flow coefficients when the frequency ratio is the study variable. The discussion continues with the characteristic of the transient time i.e. the time required for the flow to reach a stable state.

6.2 Transient time

In the force coefficients time-series diagrams of the previous chapter it can be observed the transition period T_a, until a steady pattern or a pure sinusoid starts manifesting, it is measured as the number of oscillation periods completed by the cylinder's motion. During the transition period the forces exhibit higher or lower values than the values of the later in time periods.

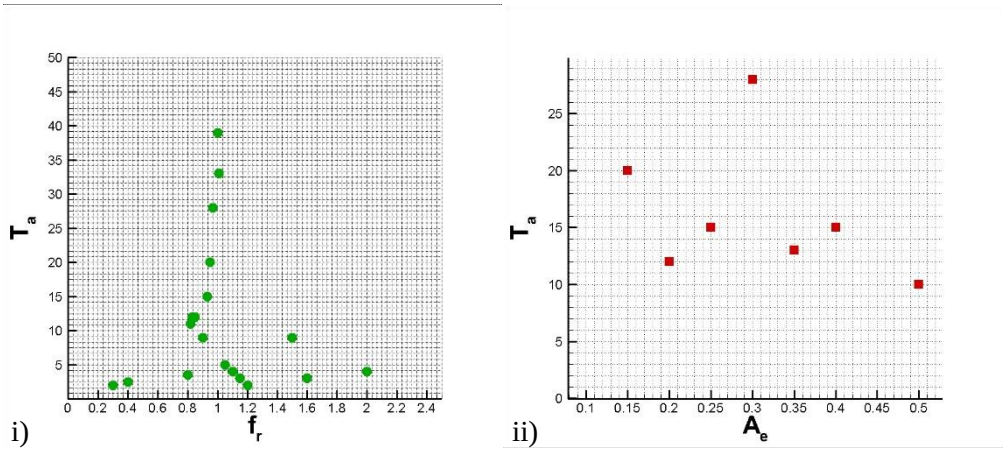

Figure 6-5 Transition period T_a against i) frequency ratio and ii) excitation amplitude

In the Figure (6-5) above the transition period is plotted against the i) frequency ratio and ii) the excitation amplitude. As far as it concerns the f_r, it can be observed that the lower lock-in region cases closer to the unity i.e. the band between [0.9,1] present the longest transition period rather

the rest of the cases fall in the same band of transition between $2T_{osc}\ and\ 10T_{osc}$. For the A_e the observations cannot reach to a similar conclusion as the T_a values of Figure (6-5), of the previous page, (ii) do not follow a trend as the excitation amplitude modifies. It is understood, that the transition period has a dual character numerical and physical. More precisely, the flow suddenly acquires an acceleration due to the forcing term at the cylinder wall that exaggerates the numerical computations in the near wall cells at the beginning of the computational procedure that justifies the increased values. Furthermore, every timestep the flow is fully resolved thus the different transition periods represent the physical adaptation of the pressure and the shear stresses to the motion; although the forces are not further analysed to precisely define the effect on the individual force components. The increased adaptation period suggests that the flow strives into reaching a steady state in the lock-in region, rather in the non-lock-in cases the forces time series are almost immediately acquiring the equivalent repeated pattern values. Anagnostopoulos also observed that increasing of the oscillation frequency in the upper lock-in region, reduces the number of oscillation cycles required for the transient (Anagnostopoulos 2000); that is in agreement with the trend of the transition time for the frequency ratios over unity of the present investigation and the current thesis results are further enhancing the description of the transition period in the lower lock-in region and the non-lock-in regions as well.

6.3 The energy transfer between the fluid flow and the cylinder

According to textbooks (Naudascher, Rockwell 2012) the work done by a force during an oscillation cycle can be derived by the integration of the inner product of the force and the displacement vector that yields

$$W_o = \oint \vec{F} \cdot \overrightarrow{dx} = \int_0^{T_o} \vec{F} \cdot \vec{\dot{x}} dt \tag{6.1}$$

Recalling from the 3rd chapter the energy coefficient C_E can be written in dimensionless form as

$$C_E = \int_{t_0}^{t_0+T_{osc}} C_L(t)\, V_e(t) dt \tag{6.2}$$

Where T_{osc} is the oscillating period V_e the transverse excitation velocity and C_L is the lift coefficient and t_0 a point in time which for convenience can be regarded as 0.

For the calculation of the integral there exist a few numerical methodologies; Blackburn and Henderson(1999) made use of Green's theorem to calculate the area integral of the limit cycle that the phase diagram of C_L and $V_e$is converging to. Stewart, Leontini et al (2005)evaluated the integral by making use of composite Simpson's rule on the limit cycle. Both methodologies need to define by approximation the limit cycle (e.g. cubic splines) and then numerically calculate the integral. Recently, Tang, Lu et al(2016) provided an analytic but also empirical methodology and eliminated the numerical labour; they observed that in the lock-in region the Fourier transform reveals frequencies that are multiples of the oscillation frequency, thus the lift coefficient can be written as a sum of sinusoids with the corresponding amplitude, frequency and phase as follows

$$\begin{aligned} C_L(t) & \\ &= C_{L1}\sin(2\pi F_r + \varphi_1) + C_{L2}\sin(4\pi F_r + \varphi_2) + \ \dots \\ &+ C_{Lk}\sin(2k\pi F_r + \varphi_k) \\ &= \sum_{k=1}^{K} C_{Lk}\sin(2k\pi F_r + \varphi_k) \end{aligned} \tag{6.3}$$

Recalling from mathematics that the set of trigonometrical functions $\sin(n\omega t), \cos(m\omega t)$ is an orthogonal set and that the integral of the product of two orthogonal functions is zero, the integral that expresses the energy coefficient after some calculations yields,

$$C_E = \pi C_{L1} A_e \sin(\varphi_1) \tag{6.4}$$

As a result of the calculations, only the fundamental i.e the first term of the right hand side of the equation (6.1) of the last page takes part in the energy transfer while equation 6.4 suggests that the phase difference between the lift coefficient and the oscillation displacement controls the energy transfer between the cylinder and the fluid (Naudascher, Rockwell 2012).

Before the energy transfer coefficient results the concept of the force-displacement or phase diagrams is introduced as an alternative study approach that facilitates the observations and is commonly used in the FSI studies.

6.3.1 The force displacement diagrams

In this paragraph another tool for the observation of the lock-in conditions is employed, that will help in defining more precisely the lock-in conditions. Initially the lock-in characteristics observed in the results of the previous chapter through the forces time-series and their FFT analysis will be underlined, so this methodology is verified to be able to reveal the basic

characteristics of the lock-in conditions. Next, a case where the time-series and the FFT analysis reveals non-lock-in conditions will be presented, it will be shown that the phase portrait analysis reveals lock-in conditions. In the following paragraph the mathematical context of the phase-portrait analysis is presented for completeness reasons.

It is common when the studies involve the investigation of relations between variables, to examine their co-evolution in time. In the present paragraph the variables under investigation are the force coefficients and their behaviour along with the harmonic motion characteristic variables of displacement and velocity is sought. It is mandatory for the better understanding of the present paragraph to borrow from the mathematical theory of the superposition or combination of two harmonic oscillations. Since the harmonic motion is prescribed to be perpendicular to the flow it is of the same direction with the lift force and vertical to the direction of the drag force, thus for the lock-in region only it is considered the combination of two same direction harmonic motions for the pair of lift and harmonic motion and two perpendicular harmonic motions for the pair of drag and cylinder's motion.

When the frequency ratio is lower than unity and below the lower lock-in limit (-20%St), the force coefficients time-series are periodic but non-harmonic since they are not pure sinusoids but a combination of sinusoids as it was observed in the last chapter initial results.

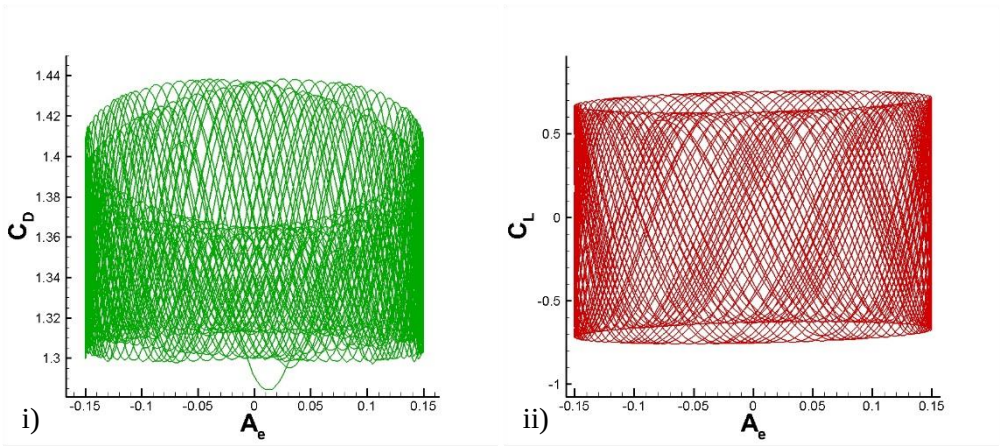

Figure 6-6 (i)C_D (green line) and (ii) C_L (red line) phase portraits with cylinder's harmonic displacement for frequency ratio equal to 0.3

In the Figure (6-6) above the force coefficient-harmonic displacement diagrams can be observed. It is apparent the non-lock-in behaviour of the FSI system since the trajectory path densely covers the region with horizontal boundaries the amplitude of the harmonic motion [-0.15, 0.15] and vertical boundaries the maximum and minimum amplitude of the corresponding force coefficient; this is expected since the resulting force time-series is a non-harmonic signal. The same behaviour is observed for all the non-lock-in cases below the lower limit (-20%St) of the lock-in region and a conclusion cannot be drawn for the relation between the forces and the motion rather than they

are not locked-in. The form of the trajectory radically changes when the f_r is located inside the lock-in region. In the Figure (6-7) below, the drag (i) and the lift (ii) coefficients can be observed for the $A_e = 0.15$ cases and the frequency ratios of: (a) 0.82, (b) 0.83 and (c) 0.85. It is evident that the trajectory is a single curve that repeats over time with a constant phase for both force coefficients. The shape resembles the trajectory as it occurs from the combination of two harmonic signals i.e. the resulting harmonic force coefficient and the cylinder's motion.

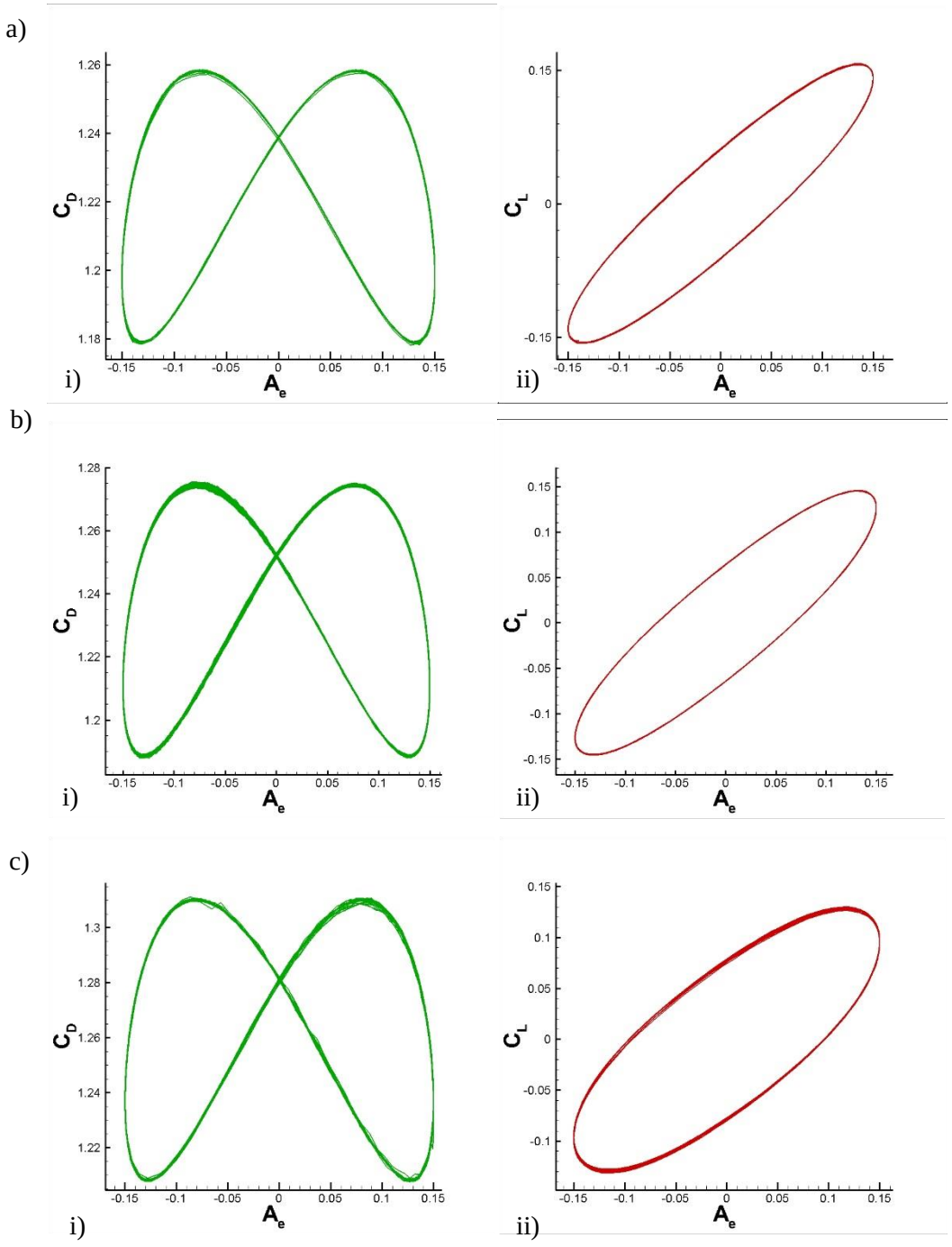

Figure 6-7 (i)C_D (green line) and (ii) C_L (red line) phase portraits with cylinder's harmonic displacement for frequency ratios equal to $a)0.82, b)0.83$ and $c)0.85$.

As it can be observed the shape of the trajectory is common for the cases in the lock-in region. For the drag coefficient the "*butterfly*" shape is defined by the response frequency and amplitude of the resulting force coefficients time-series to the cylinder's motion. The fact that on the upper and the lower region of the amplitude axis of all the f_r cases of the drag a pair of crests and troughs can be observed, signifies that the C_D acquires a frequency that is the double of the value of the excitation frequency while in lift case the ellipsoid signifies that the frequency of the C_L is of the same value as the f_e.

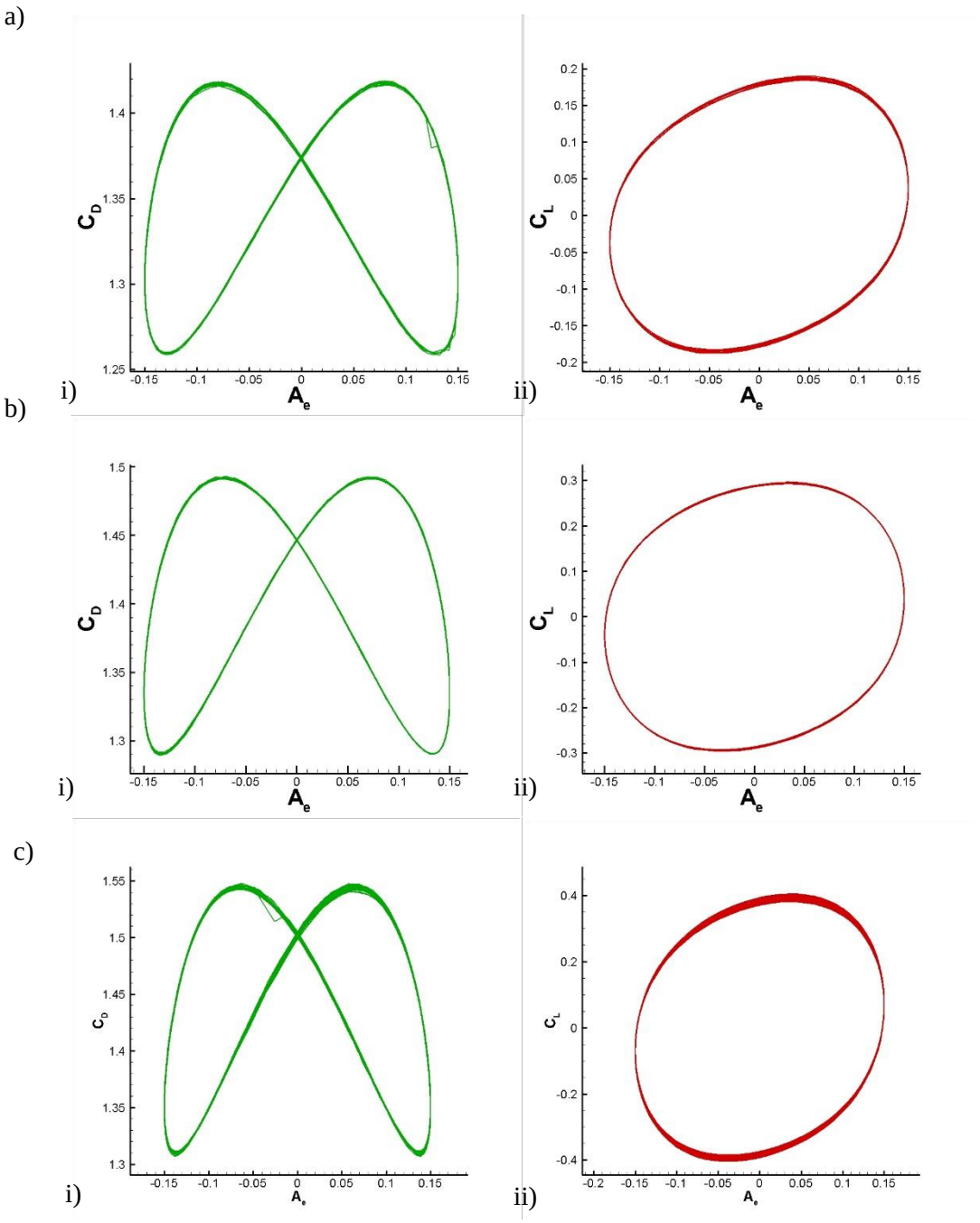

Figure 6-8 (i)C_D (green line) and (ii) C_L (red line) phase portraits with cylinder's harmonic displacement for frequency ratios equal to $a)0.9, b)0.93$ and $c)0.95$.

Furthermore, in the Figure (6-8) (ii) of the previous page it can be observed the circular shape of the lift-displacement diagram in contrast to the Figure (6-7) (ii) of page 118. The phase difference reduces as the shapes is closer to a circle and increases when it has the form of an ellipsoid. Recalling from the results of the previous chapter in paragraph 5.1.1, the drag coefficients amplitude is increasing while for the lift it is decreasing; the same conclusion is more obvious in the figure above when observing the C_D and C_L axis correspondingly. It is also observed that the area enclosed by the trajectory is increasing as the frequency ratio increases; the area enclosed is important as it represents the energy transfer and will be described in the following paragraphs.

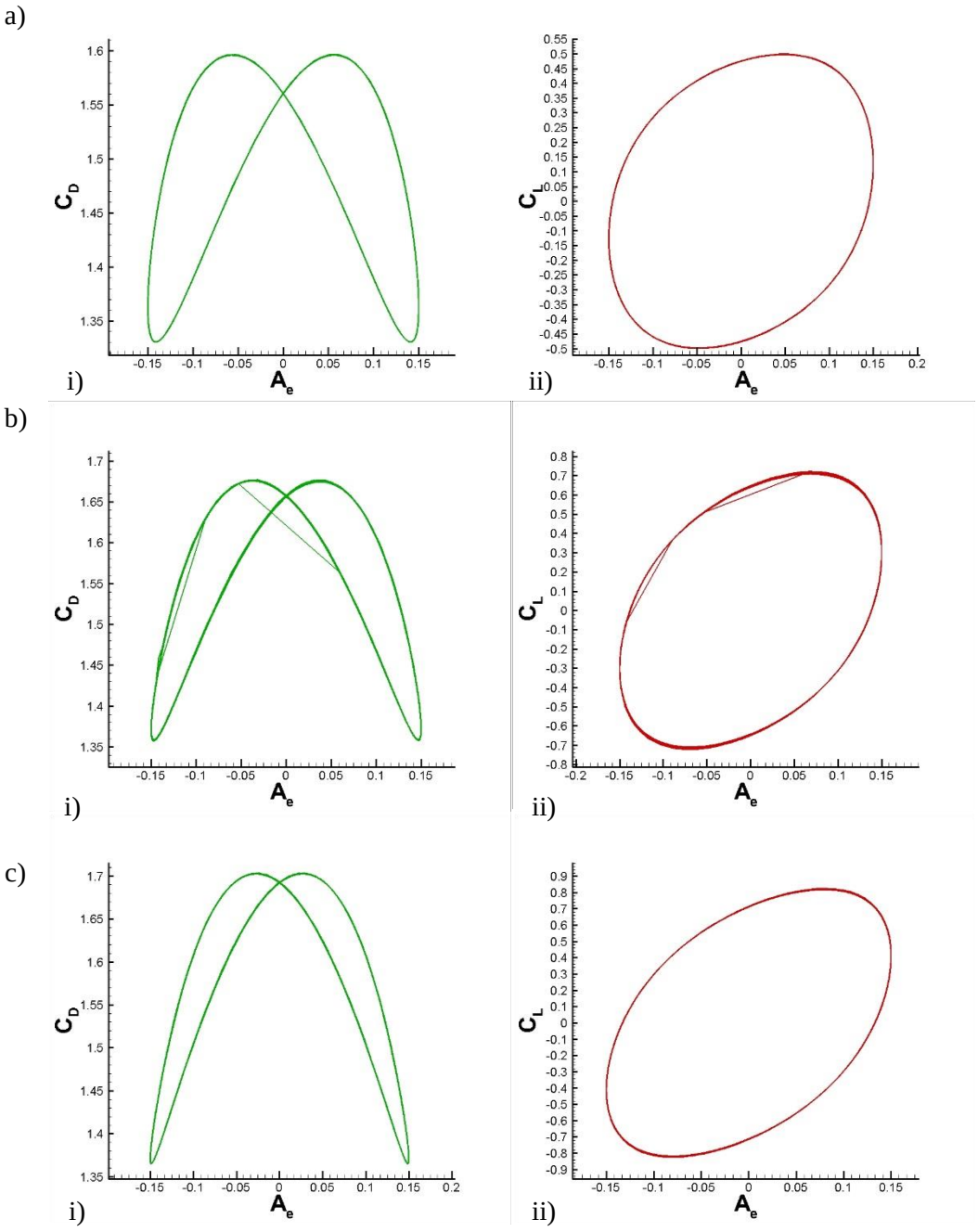

Figure 6-9 (i)C_D (green line) and (ii) C_L (red line) phase portraits with cylinder's harmonic displacement for frequency ratios equal to $a)0.97, b)1$ and $c)1.01$.

The description is similar for the higher frequency ratios cases of the Figure (6-9) of the previous page. The close to circle trajectory of the lift coefficient in (a)(ii)is transforming to an ellipsoid when the unity frequency ratio is crossed , (b) (ii) and (c) (ii) .

So far it is proved that the phase portraits can lead to the same conclusions derived from the observation of the time series and the FFT analysis, but the phase portraits become more useful when the relation between the cylinder oscillation displacement or velocity and the force coefficients is observed. The following paragraph is emphasizing on this relation and examines the concept of energy transfer between the cylinder and the flow.

6.3.2 The phase difference between the lift and the harmonic displacement

The previous paragraph presented the phase portraits as the alternative means to study the interaction of the fluid flow and the cylinder's motion. The previous paragraph description precedes the concept being introduced in the present paragraph that examines the harmonic oscillation velocity and the force coefficients. The Figure (6-10) below, presents the lift coefficient and harmonic displacement phase difference for the lock-in region frequency ratio cases for the excitation amplitudes under study in the present thesis.

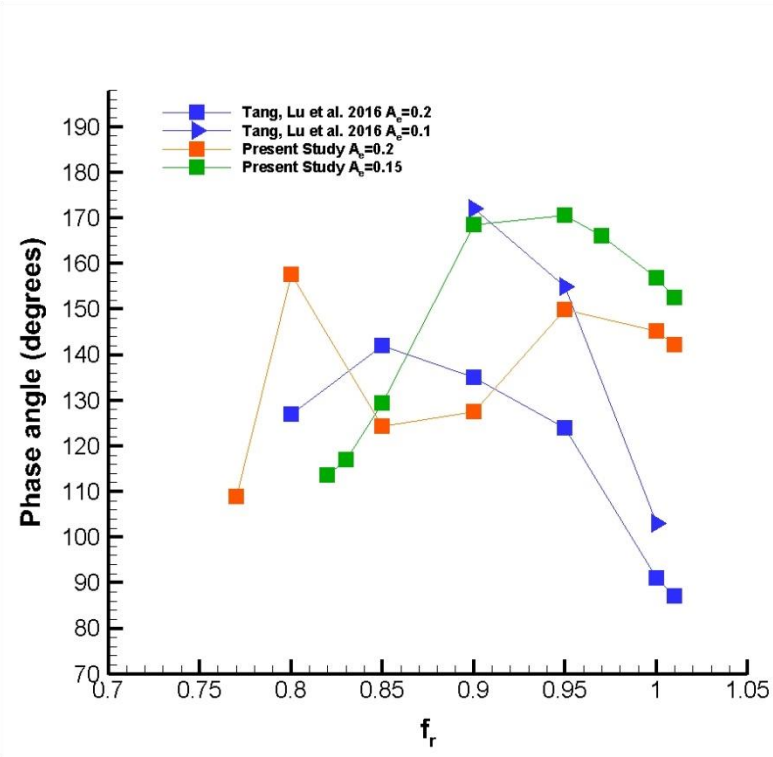

Figure 6-10 phase angle between the lift coefficient and the cylinder's displacement against the (Tang et al. 2016) study (blue line).

It is apparent that the current study does not accurately agree with the trend of phase angle for the different amplitudes study of (Tang et al. 2016); although it agrees with the sign of the phase angle which is positive for all cases as in Tang, et al study. A positive phase difference between $0^o \; and \; 180^o$ represents the energy transfer from the fluid to the cylinder and a phase between $-180^o and \; 0^o$ implies that the energy is transferred from the cylinder to the fluid; recalling from the literature review chapter an FSI study results always in a positive phase angle. The energy transfer coefficient is examined in the following paragraph.

6.3.3 The energy transfer coefficient

The aforementioned energy coefficient formula is valid in the lock-in region and it is adopted for the lock-in region of the present study. Recalling from equation (6-2) in page 115 and employing the equation (6.4) in the page 116, the Figure (6-11) below presents the energy coefficient study cases of $A_e = 0.15, 0.2$ are presented for the lock-in frequency ratio cases.

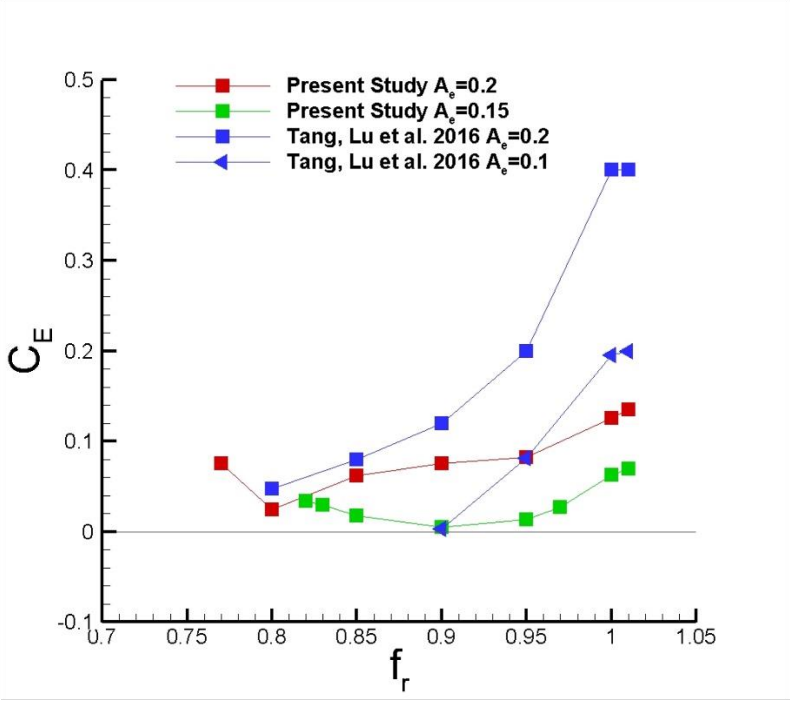

Figure 6-11 energy coefficient vs frequency ratio diagram for the $A_e = 0.15, 0.2$ cases in comparison with (Tang et al. 2016)

As the C_e is dependent on the phase angle from equation (6.4) of page 115, the aforementioned discrepancy of the phase angle of the previous paragraph is inherited into the calculation of the

energy coefficient; nonetheless as the phase angle is positive the C_e is also positive signifying the transfer of energy from the fluid to the cylinder as it would in an FSI study.

An explanation for the discrepancy of the phase angle can be provided it is considered that the St frequency calculated with the present algorithm, that obtains the values of 0.199, has a difference with the St=0.193 for Re=200 of the study of (Tang et al. 2016), the lift coefficient r.m.s. value was also smaller than the Tang et al study The aforementioned numerical discrepancy of the St number, affects the solution of the Navier-Stokes system of equations as it can be observed in the equation 3.15 of page 49 and therefore the results. The author of the present study achieved better results as far as it concerns the stationary characteristics by employing a denser mesh, that could remedy the inconsistency of the Figure 6-11 of the last page but unfortunately the results could not be included in the present thesis.

6.4 The transition to the lock-in region

Recalling from the results of the previous chapter on the FoV cases for constant $A_e = 0.15$ and discretely variable frequency of the cylinder's harmonic motion, the flow adapts to the motion and a periodic pattern of the force coefficients appears for all cases regardless of the case being in or out of the lock-in region.

For the cases of small frequency ratios, see Figure (5-2) (a) of paragraph 5.1 in page 86, the corresponding FFT analysis of Figure (5-21) and (5-22) of page 97 and 98 correspondingly, shows three spectral components for the drag and two spectral components for the lift coefficient. The dominating frequency component for both cases is the St component while the excitation component appears only for the lift coefficient at a very small spectral amplitude. At these frequency ratios it can be speculated that the flow is not crucially affected by the motion rather it can be considered that it is disturbed; the motion alters the vortex shedding procedure that nonetheless leads to a Benard-Karman street, new vorticity regions are not generated.

Increasing the frequency ratio to the value $f_r = 0.8$ close to the lower lock-in region limit (-20%St) leads to a multiple of spectral components, observe Figure (5-23) of page 98, while at the value of $f_r = 0.82$ the lock-in conditions were observed with only one frequency appearing for both force coefficients spectra, see Figure 5-24 (a) of page 99. The region between the last two frequencies was further examined in detail to pinpoint the lower lock-in limit. The table below

presents the aforementioned region cases where the frequency ratio varied with a smaller step than in the cases of Chapter 5.

Table 6-1 lower lock-in limit neighborhood cases

A_e	f_r									
0.15	0.801	0.802	0.803	0.804	0.805	0.806	0.807	0.808	0.809	0.81

For the first two cases of Table (6-1) the results showed similar behaviour to the $f_r = 0.8$ case. Recalling from the description of the previous chapter, the dominant spectral component appears to be a small frequency that is the difference of higher frequencies values, the drag spectra show both excitation and St components while the lift spectra is missing the St component. From the spectra it appears that when the frequency ratio approaches the lock-in limit, the competition of frequencies involves more than the two standard frequencies, namely the St and the excitation frequency.

The study of the transition to the lock-in region revealed that there is an immediate to the lower lock-in limit region, where the competition becomes more intense and the flow characteristics are not conclusive as far as it concerns the distribution of pressure and vorticity around the cylinder; recalling that the forces are calculated by integration of the pressure and the shear stresses around the cylinder, see equations (1.6) and (1.7) of pages 16 and 17 correspondingly, and the fact that many frequencies appear, suggests that before the lower lock-in limit the motion affects radically the flow over the entire surface of the cylinder. On the contrary in the non-lock-in region away from the lower lock-in limit neighbourhood the force coefficients spectral analysis presents only a few components with the St being dominant, as such the motion creates one more component that relates to the motion and one more that relates to the competition of the vortex shedding and the motion, although the two force coefficients do not present the same behaviour which means that the force direction is biased by the harmonic motion direction and there is a different effect on each force coefficient.

From the aforementioned conclusions it is deduced that before the limit of the lock-in region the total lift or drag force is the sum of a multiple of component vectors that are periodic in magnitude and direction due to the multiple of flow changes that occur around the cylinder, although the harmonic characteristic is not present as the frequencies that appear are not related i.e. they are not multiples of one fundamental frequency. Finally the small frequency components are the differences of higher components frequency values.

Moreover, integer multiples of the excitation frequency are also manifesting in contrast to the previous cases, observe the peaks at one, four and five times the oscillation frequency in Figure 5-23(i) of page 98.

6.5 The lock-in region

The lock-in limit is located at $f_r = 0.803$ where the spectra appear a single peak for both force coefficients. The lock-in fluid flow characteristics, for the particular amplitude study of $A_e = 0.15$ and for all the frequency ratio cases, are identical to that of a stationary cylinder i.e. the Benard-Karman street manifests with no significant alterations of the vortex shedding procedure; recalling from the literature review the small oscillation amplitude of the cylinder does not promote the generation of new vorticity regions. Moreover, the study of different oscillation amplitudes leads to the same conclusion for the fluid flow characteristics of higher amplitudes.

The lock-in region can be divided to the resonance and non-resonance mode, in the first case the lock-in occurs with the magnitude of the force coefficients being small while in the second cases the magnitude is magnified with the maximum occurring at the higher than unity frequency ratio of 1.01, see Figure 5-29 of page 102.

As before, the study was extended to locate the upper limit of the lock-in region. In contrast to the lower limit that was located almost exactly on the -20% of the St frequency the upper limit is located at +3% of the St frequency. Recalling from the literature review the upper lock-in region presents discrepancies as far as it concerns the lock-in conditions; despite the excitation frequency being the dominant frequency more frequencies appear as the time-series are not anymore pure sinusoids. In the present cases the upper limit where the last sentence conditions exist is located at the $f_r = 1.05$ while for the higher frequency ratio of 1.1 the dominant frequency ceases to be the excitation frequency.

After the $f_r = 1.05$ and up to $f_r = 2$ the conditions appear to be very similar to the neighbourhood below the lower lock-in limit i.e. very low frequencies that appear to be the differences of higher frequencies appear to be dominant in the drag coefficient spectrum while the lift coefficient spectrum presents neither the St nor the excitation frequency.

6.6 An approximation of the force coefficients in the lock-in region

As mentioned earlier the motion is vertical to the drag force direction thus the trajectory can represent the motion of a mass m as it occurs from the combination of two perpendicular harmonic motion ODEs i.e.

$$m\ddot{y} + k_y y = 0 \tag{6.5}$$

$$m_{cd}\ddot{C_D} + k_{cd}C_D = 0 \tag{6.6}$$

The solutions of the system are

$$y = A_e \cos(\omega_e t + \varphi_e) \tag{6.7}$$

$$C_D = A_{C_D} \cos(\omega_{C_D} t + \varphi_{C_D}) \tag{6.8}$$

The equation (6.1) is imposed through the FoV and the φ_e can be considered to be zero. The equation (6.2) can be concluded with the following relations holding for the lock-in region,

$$\frac{\omega_e}{\omega_{C_D}} = \frac{n_1}{n_2} = r \tag{6.9}$$

The *r* in the equation (6.5) above represents a rational number that as it was observed in the FFT analysis of the drag coefficient obtains the value of two. The phase difference will vary from 15-30 degrees for the drag coefficient.

So far the fluid response to the motion in the lock-in region can be predicted by employing equation (6.4) of page 116, although the amplitude has also to be predicted. A polynomial interpolation between the force frequency values calculated from the solution of the numerical algorithm can provide an approximation function of the frequency and the corresponding drag coefficient amplitude.

Recalling from the FFT analysis of the previous chapter a sample of the drag coefficients amplitudes can be provided and is summarized in the following Table (6-2)

Table 6-2 sample cases for the divided differences interpolation of the A_{CD}

f_r	0.82	0.85	0.9	0.93
A_{CD}	0.013	0.035	0.032	0.045

The corresponding Newton divided differences tableaux for the data of Table (6-2) is given below in Table (6-3) the diagonal elements being the coefficients of the Newton polynomial of equation (6.5) below the table

Table 6-3 Divided differnces interpolation tableaux C_D amplitude approximation

x_n	0^{th} order	1^{st} order	2^{nd} order	3^{rd} order
0.82	0.013			
0.85	0.035	0.73		
0.9	0.032	-0.06	-9.88	
0.93	0.045	0.43	6.125	145

The corresponding Newton interpolation 3^{rd} order polynomial then yields in the next page

$$f(x) = 0.013 + 0.73(x - 0.82) - 9.88(x - 0.82)(x - 0.85) + 145(x - 0.82)(x - 0.85)x \quad (6.10)$$

Applying the polynomial to already existing values as predicted from the solution of the algorithm provides a good approximation of the amplitude of the drag coefficient e.g. for $f_r = 0.83$ the polynomial approximation yields the value of 0.016 that is in very good agreement with the actual calculated value of 0.014 that corresponds to the FFT analysis results. For the lift coefficient the corresponding sample values are presented below in Table (6-4) below,

Table 6-4 sample cases for the divided differences interpolation of the A_{CL}

f_r	0.82	0.85	0.9	0.93
A_{CD}	0.07	0.053	0.073	0.143

The corresponding Newton divided differences tableaux for the data of the Table (6-4) is presented below in the Table (6-5) with the diagonal elements being the coefficients of the Newton polynomial of equation (6.6) below the table.

Table 6-5 Divided differences interpolation tableaux for the C_L amplitude approximation

x_n	0^{th} order	1^{st} order	2^{nd} order	3^{rd} order
0.82	0.07			
0.85	0.053	-0.04		
0.9	0.073	0.04	5.5	
0.93	0.143	2.3	63.3	525.45

The corresponding Newton interpolation 3rd order polynomial then yields

$$f(y) = 0.07 - 0.04(y - 0.82) + 5.5(y - 0.82)(y - 0.85) + 525.45(y - 0.82)(y - 0.85)y \quad (6.11)$$

The approximations of the force coefficient amplitudes of equations 6.5 and 6.6 for the drag and lift correspondingly can be improved if a bigger sample of data is collected and therefore a higher order polynomial approximation can be achieved. The approximations can be employed for the faster prediction of the lift and drag forces without the need for the solution of the Navier-Stokes thus facilitating the studies.

6.7 Summary

The present chapter presented the validation of the algorithm, the induced results of the 5th chapter study and the new findings in the topic of FSI and the FoV studies. Initially, the validation of the algorithm was performed against the past studies. The time-series of the force coefficients, inside and outside the lock-in region are in good agreement with the studies of (MadaniKermani 2014, Tang et al. 2016), see Figures (6-1) and (6-2) of pages 109 and 110 correspondingly. The statistical values of C_{Lrms} and C_{Dmean} follow the same trend as the corresponding values of (Tang et al. 2016), see Figure 6-3 of page 111. Although the C_{Dmean} appears to be reduced in comparison to the values of (Tang et al. 2016); the previous discrepancy is justified if the different stationary characteristics i.e. different St between the present study and the comparison study is taken under consideration.

Secondly the adaptation time was examined. It is observed that the adaptation time T_a is dependent on the frequency ratio. Anagnostopoulos (2000) was the first to make the observation of the adaptation time in the upper part of he lock-in region; the T_a reduces as the f_r is increasing in the upper region. The new findings add to the findings of Anagnostopoulos and present the behaviour of the adaptation time for all the extent of the frequency ratio range in both the upper and lower region. Recalling from Figure 6-5 in page 112, in the lower non-lock-in region the T_a varies from $3T_o$ to $5T_o$. When the f_r enters the lock-in region the T_a starts increasing to values over $10T_o$ and reaches the highest value of $38T_o$ at the unity frequency ratio. Tha T_a starts decreasing when the unity is crossed and after the upper lock-in limit in the upper non-lock-in region acquires again values below $10T_o$.

Furthermore, the upper and lower regions of the unity frequency ratio were described. In the lower region non-lock-in cases the force coefficients presented a combination of sinusoids in their time series that nonetheless were periodic. Approaching the lock-in region the intensity of the competition between the St and the harmonic oscillation frequency of the cylinder becomes more evident as it is observed in the FFT analysis of the force coefficients in the 5th chapter. What is observed for the first time is the partition of the lock-in region to two regions. The first region that belongs to the lower range of the lock-in frequencies presents lock-in conditions but lacks the magnification of the forces that is a characteristic of the lock-in region. The increase of the forces' amplitudes occurs around at the 10% below the unity frequency ratio. Furthermore, the highest resonance amplitude is observed for the value of frequency ratio that is over the unity, although that value is not far from the unity.

The suitability of the algorithm to represent a ViV case was also proved successful; although the results lack of the accuracy when compared to the study of (Tang et al. 2016).

Finally, a linear model is proposed for the lift and drag coefficients inside the lock-in region. it is observed from the force- displacement diagrams of 6.3.1 that the lift coefficient and the harmonic motion behave as a system of parallel combined harmonic motions, while the drag coefficient and the harmonic motion can be represented by a system of perpendicular harmonic motions. The amplitude of the forces coefficients was approximated by a Newton polynomial that allows to predict the forces without performing a full resolution of the fluid domain.

7 Conclusions and future work

One of the first investigations in the FSI field, that is the main topic of the thesis, is the Aeolian Tones produced by the vibrations of a wire in a wind flow performed by Vincenz Strouhal (1878). In 1879 Lord Rayleigh enhanced the observations when he noticed that the wire was vibrating on a plane perpendicular to the flow (1915). Henri Claude Bénard(1926) and Theodore von Karman(1911) revealed that the mechanism of the vortex shedding controls the Aeolian Tones and the vibrations of the wire, thus the acronym ViV. In general, when the frequency of the tone coincides the wires natural frequency the vibrations' sound is greatly reinforced. This phenomenon is called lock-in and is the main investigation topic of the present thesis.

In ocean engineering, various cylindrical structures are utilised to convey fluid from wells on the seabed. These structures are subject to varying intensity flows and oscillatory waves that differ according to the depth and the natural characteristics of the flow. The mathematical modelling and the numerical representation of the interaction of these structures with the flow surrounding them should accurately predict their fatigue life. Sengupta, Low et al (Sengupta et al. 2016) attempt to gather and define design parameters and criteria of these structures. The current thesis attempts to define the lock-in conditions and approximate the forces exerted on a moving circular cylinder.

An FSI system is a coupled system of two different physical components namely the fluid and the structure. According to Felippa et al, the interaction or the coupling between the two physical components can be "*one-way*" or "*two-way*", depending on the characteristic of feedback between the two components. As in a numerical solution of a single physical field, a two-field coupled system needs to be discretized in space and time; space partitioning can be algebraic or differential (Felippa et al. 2001). In the first case, the complete coupled system is spatially discretized first and then decomposed, while in the second case the decomposition is performed first and each field is discretized separately. The time discretization depends on the method chosen for the FSI

representation; to simulate a coupled system there are two major approaches one can follow: the computational methods used to decompose and synchronise the different systems, so a unified model is constructed to simulate the behaviour of the overall system.

- **The monolithic or simultaneous treatment (direct).** The whole problem is treated as a monolithic entity and all components advance simultaneously in time.
- **The partitioned treatment (iterative).** The field models are computationally treated as isolated entities that are separately stepped in time.

According to Le Cunff, Biolley et al (2002), three approaches have been proposed to investigate numerically the FSI phenomena. In the first approach, the modal response of the structure to the vortex shedding is utilised to provide fast a lifetime estimate for the structure fatigue. In the second, the structural equation is resolved in time along with a fluid model, while the third approach is resolving the structural equation along with the full Navier Stokes equations.

The current thesis is examining the "*one-way*" interaction of a coupled system in a monolithic approach. Briefly the cylinder is harmonically displaced, disturbs the fluid at the circumference and the flow responds to the motion. Thus, a fixed motion is prescribed for the cylinder (a structural equation is not resolved) that is stepped in time with the same time-step of the numerical solution of the flow equations and the fluid response through the forces exerted on the cylinder is studied.

The Re number range of the flow investigated is the steady regime, approximately 40<Re<200. In this regime the dominant characteristic is the Benard-Karman street. The simulations results were compared with past studies including the unconfined flow studies of (Singha, Sinhamahapatra 2010) and (Zdravkovich 1997) that were numerical and experimental correspondingly. The algorithm was examined for the fluid flow coefficients of C_{bp}, C_{Dmean}, C_{Lrms}, the St number and the physical characteristics of the wake width and separation angle θ_s.

The numerical study commenced with the attempt of defining an initial mesh size that can predict the basic characteristic of the St number for the Re number equal to 100 flow. The study tested various configurations of the mesh characteristics; these are the number of cells on each direction, $\mathbf{N_i}$ for the circumferential and $\mathbf{N_j}$ for the radial, the stretch factor A and the surface cell size $\boldsymbol{\Delta_S}$. Two configurations were selected, the $(N_i = 286, N_j = 146,\ A = 1.03, \Delta_S = 0.01)$ and the $(N_i = 302, N_j = 126,\ A = 1.03, \Delta_S = 0.01)$. The last configurations were examined for the time independency characteristic and the last of the two was selected to continue with the tuning of the algorithm. A stretch factor study was also performed revealing the dependence of the St number on the A, see Table (4-2) in page 68. It was also observed that the large aspect ratio $A_r$of the cells in the middle of the wake region, is biasing the flow, see Figure (4-2) in page 68. The A_r

study of Table (4-3) in page 69, showed that the St number is an inadequate criterion for the flow, the variation of the aspect ratio maintained the St number but significantly affected the forces. An aspect ratio closer to unity corrected the force coefficients. The aspect ratio is well studied in the past studies and has been proven to be crucial in the solution of PDEs in general. According to the author's knowledge the flow studies are emphasizing on the aspect ratio in the region of the cylinder circumference. The aspect ratio study of the present thesis examined the aspect ratio of a region away from the cylinder's surface and the near wake. Despite the fact that the aspect ratio in the near cylinder region was very close to unity for both cases of the Figure (4-2), the Table (4-3) results signify the effect of the broader region aspect ratio on the calculations and the results. This remark has not been made before.

Secondly, the blockage effect was investigated. The initial mesh was adapted for the B_r cases of the Table (4-4) in page 70. The compression of the wake was observed depicted in the Figure (4-3) and compared with the numerical results of (Anagnostopoulos et al. 1996) in Figure (4-4) of page 72. The wake width for the different B_r cases can be observed in the Table (4-5) of page 72. The variation of the C_{bp}, C_{Dmean}, C_{Lrms}, the St number was also investigated in the blockage ratio study. The effect on the St number is apparent in the Figure (4-5) of page 73, where the St number increases as the B_r increases. The C_{bp} increases as the B_r increases, see Figure (4-6) in page 74, while the force coefficients also increase as the B_r increases, see Figure (4-7) in page 74. The width of the channel should be 100D, so the flow is considered free of the lateral position of the boundaries effect. Although, the mesh configuration chosen was the ($N_i = 300, N_j = 244$, $A = 1.02, \Delta_S = 0.01$) that corresponded to a channel width of 40D. The lower blockage ratios were computationally expensive for the current computational system.

The stationary cases validation study continued with the examination of the algorithm and its appropriateness for different Re numbers in the steady region, namely for the Re numbers of 80,100,120 and 200. The Figure (4-10) of page 78, depicts the vortex shedding for the Re numbers under study. The St number the lift, drag coefficients were compared with other cases in Figure (4-11) of page 79. It is observed that the C_{Lrms} value increases as the Re number increases. It is in a good agreement for the Re numbers of 80 and 100 while there is a difference for the Re numbers of 120 and 200. The $C_{Dmean}$the second part of the same figure is in good agreement with the experimental studies of Tritton for the Re numbers of 80,100 and 120 while it presents differences with other numerical and experimental studies.

In general, the stationary study for the determination of the flow characteristics presented valid results in comparison with other studies. Any differences observed are inside the margins of the differences between numerical methods and these are common between studies; observe the differences for the values of the force coefficients in the Table (4-6) of page 75. The mesh

configuration mentioned earlier in this page, was selected to proceed with the FoV study of the thesis in the fifth chapter.

Briefly, in the present FoV studies the motion of the cylinder is in effect from the start of the FoV simulation. The wake of the cylinder has neither developed any flow structures nor separation has occurred prior to the motion. The force coefficients are the main variables examined for the different excitation amplitudes and frequencies of the cylinder's harmonic motion. The study cases can be observed in the Figure (5-1) and Table (5-1) of page 82 for steady amplitude and variable frequency, while the Table (5-3) in page 83 presents the cases of fixed frequency and variable amplitudes. The FoV results were compared with the stationary cases results, while the results between the different cases were also compared.

The results of the FoV studies were compared with the studies of (MadaniKermani 2014) in Figure (6-1) of page 109, and (Tang et al. 2016) in Figure (6-2) of page 110. The comparison showed a good agreement as far as it concerns the time-series of the force coefficients. In Figure (6-3) of page 111, the C_{Dmean} and the C_{Lrms} are compared with the results of (Tang et al. 2016). TheC_{Lrms} shows a very good agreement, while the C_{Dmean} appears diminished in comparison with the values of (Tang et al. 2016). The behaviour of the C_{Dmean} and the C_{Lrms} was also compared and was found to be in good agreement with the results of (Anagnostopoulos 2000) in Figure (6-4) of page 111.

Morevover, the transient time for the FoV cases was examined. According to the author's knowledge the particular study has been performed only for a part of the lock-in frequency region in the study of (Anagnostopoulos 2000). The FoV study presented a full examination of the transient study for the full extent of the lock-in and the non-lock-in regions as well. The present thesis postulates that the transient period has a dual character numerical and physical. More precisely, the flow suddenly acquires an acceleration due to the forcing term at the cylinder wall that exaggerates the numerical computations in the near wall cells at the beginning of the computational procedure, that justifies the increased values. Furthermore, every timestep the flow is fully resolved thus the different transition periods represent the physical adaptation of the pressure and the shear stresses to the motion. The increased adaptation period suggests that the flow strives into reaching a steady state in the lock-in region, rather in the non-lock-in cases the forces time series are almost immediately acquiring the equivalent repeated pattern values.

The study continued with the examination of the phase between the lift coefficient and the harmonic displacement, that is strongly related to the energy transfer. Employing the method of (Tang et al. 2016), represented by equation (6.3) of page 114, that takes advantage of the orthogonality between sinusoidal functions, the work done by a force during an oscillation cycle

of equation (6.1) of page 113, or the energy transfer of equation (6.2) in the same page, can be calculated by the reduced form of equation (6.4) of page 114.

The results on the phase and the energy coefficient can be observed in the Figures (6-10) of page 119 and (6-11) of page 120 correspondingly. Although the results are not in accurate agreement with the results of Tang et al the major characteristic of the FoV studies, that is to represent a ViV case, is achieved. It can be observed that the phase is positive in the lock-in region and the lift force leads the motion by a constant phase angle. Consequently, the energy transfer is positive, meaning the energy is transferred by the fluid to the cylinder that corresponds to a ViV condition.

Although the cases of the frequency ratio are discrete and a continuous development of the flow for changing excitation frequency and amplitude of the harmonic oscillation of the cylinder cannot be observed, the spectral analysis of the force coefficients showed interesting and new results for the lower/ upper non-lock-in regions and the lock-in region. More precisely the lower non-lock-in region away from the limit of the lock-in region is dominated by the St frequency. In the upper non-lock-in region the St frequency does not appear in the spectral analysis of the force coefficients. The previous fact is an emphasis on the excitation role of an FSI phenomenon that can radically affect the flow, as Sarpkaya underlined, and has not been observed before. The lower lock-in region limit was located at exactly -20% of the St number while the upper limit was located at +5% of the St number. The transition to the lower lock-in limit revealed the competition of the vortex shedding frequency and the excitation frequency of the cylinder, observe the Figure (5-23) of page 96; there appear multiple frequency components apart from the St and the excitation frequency, the small values are the differences of higher values that corresponds to the modulation observed by Bishop and Hassan. In the upper non-lock-in region after the upper lock-in limit, the multiple of frequencies appears again, observe Figure (5-31) of page 101; although the St number is not present in neither of the force coefficients. The St number re-appears in the last case of the upper lock-in region where the excitation frequency is the double of the St number.

This thesis study is concluding with the approximation of the lift and drag coefficients in the lock-in region. The approximation is employing the divided differences method to produce a Netwon polynomial of third degree that can predict the lock-in characteristics of the drag and lift namely their amplitude, since the lock-in condition is dictating their frequency. The phase of the force coefficients is easily calculated from the time-series or the force-displacement diagrams. As such the polynomials are contributing to the calculation of the sinusoidal time-series without the need of performing a full resolution of the Navier-Stokes equations and an FSI algorithm. The polynomial approximation has not been attempted before and it is a new contribution in the FSI field.

The results on the force coefficient of lift agrees with the FoV condition of equations (2.5) and (2.6) of page 26 i.e. the condition of a harmonic displacement results in a sinusoidal fluid force. From the theory of combination of two harmonic motions or waves it is speculated that the force and the harmonic displacement are the solutions of the system of second order linear ordinary differential equations whose combination results in a trajectory that a material point follows under the combination of two springs; that are inline in the case of the lift and perpendicular in the case of the drag.

The extension of the present study will concentrate in the definition of the coefficients of the system of linear ODEs the first corresponds to the lift or the drag, and the second to the harmonic motion of the cylinder. The coefficients should be defined according to the wake characteristics of the flow parameters as occurred from the motion of the cylinder e.g. the St^* of the equation (2.21) in page 35. The definition of the coefficients of such an ordinary differential equation will provide faster results on the forces exerted on the cylinder than resolving the full Navier-Stokes equations. The speculation of treating the harmonic motion and the forces as one system of linear ODEs has not been made before.

Further work will also be performed to define a more accurate polynomial approximation as the one proposed in the paragraph 6.6. The effect of the aspect ratio on the fluid flow quantities will also be thoroughly examined for more cases in order to be established as a necessary condition for the accuracy of the results in the stationary and the moving cylinder cases as well.

8 References

ALAWADHI, E.M., 2013. Numerical simulation of fluid flow past an oscillating triangular cylinder in a channel. *Journal of Fluids Engineering,* **135**(4), pp. 041202.

ALFARRA, A. and DINKLER, D., 2016. Computational bridge aeroelasticity using turbulence models. *PAMM,* **16**(1), pp. 417-418.

ANAGNOSTOPOULOS, P., 2000. Numerical study of the flow past a cylinder excited transversely to the incident stream. Part 1: Lock-in zone, hydrodynamic forces and wake geometry. *Journal of Fluids and Structures,* **14**(6), pp. 819-851.

ANAGNOSTOPOULOS, P. and BEARMAN, P., 1992. Response characteristics of a vortex-excited cylinder at low Reynolds numbers. *Journal of Fluids and Structures,* **6**(1), pp. 39-50.

ANAGNOSTOPOULOS, P., ILIADIS, G. and RICHARDSON, S., 1996. Numerical study of the blockage effects on viscous flow past a circular cylinder. *International Journal for Numerical Methods in Fluids,* **22**(11), pp. 1061-1074.

BARANYI, L., 2013. Simulation of Low-Reynolds Number Flow Around a Circular Cylinder Following a Slender Elliptical Path, *ASME 2013 Pressure Vessels and Piping Conference* 2013, American Society of Mechanical Engineers, pp. V004T04A056-V004T04A056.

BARANYI, L., 2009. Triggering of Vortex Shedding by Cylinder Oscillation for Reynolds Number Under 47, *ASME 2009 Pressure Vessels and Piping Conference* 2009, American Society of Mechanical Engineers, pp. 317-324.

BARANYI, L. and DARÓCZY, L., 2013. Mechanical energy transfer and flow parameter effects for a cylinder in transverse oscillation. *International Journal of Heat and Fluid Flow,* **43**, pp. 251-258.

BARRY, O., ZU, J. and OGUAMANAM, D., 2015. Analytical and experimental investigation of overhead transmission line vibration. *Journal of Vibration and Control,* **21**(14), pp. 2825-2837.

BATHE, K. and ZHANG, H., 2004. Finite element developments for general fluid flows with structural interactions. *International Journal for Numerical Methods in Engineering,* **60**(1), pp. 213-232.

BEARMAN, P.W., 1984. Vortex shedding from oscillating bluff bodies. *Annual Review of Fluid Mechanics,* **16**(1), pp. 195-222.

BEARMAN, P., 1969. On vortex shedding from a circular cylinder in the critical Reynolds number regime. *Journal of Fluid Mechanics,* **37**(03), pp. 577-585.

BEARMAN, P., 1965. Investigation of the flow behind a two-dimensional model with a blunt trailing edge and fitted with splitter plates. *Journal of Fluid Mechanics,* **21**(02), pp. 241-255.

BEHR, M., HASTREITER, D., MITTAL, S. and TEZDUYAR, T., 1995. Incompressible flow past a circular cylinder: dependence of the computed flow field on the location of the lateral boundaries. *Computer Methods in Applied Mechanics and Engineering,* **123**(1), pp. 309-316.

BENARD, H., 1926. On the frequency law of alternate eddies behind an obstacle. *C.R.Acad.Sci.,* **182**, pp. 1375-1377.

BERGER, E., 1988. On a mechanism of vortex excited oscillations of a cylinder. *Journal of Wind Engineering and Industrial Aerodynamics,* **28**(1-3), pp. 301-310.

BERGER, E., 1967. Suppression of vortex shedding and turbulence behind oscillating cylinders. *Physics of Fluids (1958-1988),* **10**(9), pp. S191-S193.

BERGER, E. and WILLE, R., 1972. Periodic flow phenomena. *Annual Review of Fluid Mechanics,* **4**(1), pp. 313-340.

BISHOP, R. and HASSAN, A., 1964. The lift and drag forces on a circular cylinder oscillating in a flowing fluid, *Proceedings of the Royal Society of London A: Mathematical, Physical and Engineering Sciences* 1964, The Royal Society, pp. 51-75.

BLACKBURN, H.M. and HENDERSON, R.D., 1999. A study of two-dimensional flow past an oscillating cylinder. *Journal of Fluid Mechanics,* **385**, pp. 255-286.

BLEVINS, R.D., 2009. Models for vortex-induced vibration of cylinders based on measured forces. *Journal of Fluids Engineering,* **131**(10), pp. 101203.

BLEVINS, R.D., HALKYARD, J.E. and HORTON III, E.E., 2001. *Floating offshore drilling/producing structure,* .

BLOOR, M.S., 1964. The transition to turbulence in the wake of a circular cylinder. *Journal of Fluid Mechanics,* **19**(02), pp. 290-304.

BLOOR, M.S. and GERRARD, J., 1966. Measurements on turbulent vortices in a cylinder wake, *Proceedings of the Royal Society of London A: Mathematical, Physical and Engineering Sciences* 1966, The Royal Society, pp. 319-342.

BOURGUET, R., KARNIADAKIS, G.E. and TRIANTAFYLLOU, M.S., 2011. Vortex-induced vibrations of a long flexible cylinder in shear flow. *Journal of Fluid Mechanics,* **677**, pp. 342-382.

BREUER, M., 1998. Large eddy simulation of the subcritical flow past a circular cylinder: numerical and modeling aspects. *International Journal for Numerical Methods in Fluids,* **28**(9), pp. 1281-1302.

BRIKA, D. and LANEVILLE, A., 1993. Vortex-induced vibrations of a long flexible circular cylinder. *Journal of Fluid Mechanics,* **250**, pp. 481-481.

BROWN, F.N.M., 1959. The Organized Boundary Layer. *University of Texas, Proceedings of the Sixth Midwestern Conference on Fluid Mechanics, September 9-11, ,* pp. 331-349.

CAMICHEL, C., DUPIN, P. and TEISSIÉ-SOLIER, M., 1927. Sur l'application de la loi de similitude aux périodes de formation des tourbillons alternés de Bénard-Kármán. *CR Acad.Sci.Paris,* **185**, pp. 1556-1559.

CANTWELL, B. and COLES, D., 1983. An experimental study of entrainment and transport in the turbulent near wake of a circular cylinder. *Journal of Fluid Mechanics,* **136**, pp. 321-374.

CARBERRY, J., SHERIDAN, J. and ROCKWELL, D., 2005. Controlled oscillations of a cylinder: Forces and wake modes. *Journal of Fluid Mechanics,* **538**, pp. 31-69.

CARBERRY, J., SHERIDAN, J. and ROCKWELL, D., 2003. Controlled oscillations of a cylinder: a new wake state. *Journal of Fluids and Structures,* **17**(2), pp. 337-343.

CARBERRY, J., SHERIDAN, J. and ROCKWELL, D., 2001. FORCES AND WAKE MODES OF AN OSCILLATING CYLINDER. *Journal of Fluids and Structures,* **15**(3), pp. 523-532.

CHAUHAN, M.K., DUTTA, S., GANDHI, B.K. and MORE, B.S., 2016. Experimental Investigation of Flow Over a Transversely Oscillating Square Cylinder at Intermediate Reynolds Number. *Journal of Fluids Engineering,* **138**(5), pp. 051105.

CINCOTTA, J.J., JONES JR, G.W. and WALKER, R.W., 1966. Experimental investigation of wind induced oscillation effects on cylinders in two-dimensional flow at high Reynolds numbers.

COLEMAN, G.N. and SANDBERG, R.D., 2010. A primer on direct numerical simulation of turbulence-methods, procedures and guidelines.

COUREGELONGUE, J., 1929. On the existence of two families of eddies behind immersed solids. *Comptes Rendus Academie Sciences,* **189**, pp. 972-974.

DAY, M.A., 1990. The no-slip condition of fluid dynamics. *Erkenntnis,* **33**(3), pp. 285-296.

DE BOER, A., VAN ZUIJLEN, A. and BIJL, H., 2007. Review of coupling methods for non-matching meshes. *Computer Methods in Applied Mechanics and Engineering,* **196**(8), pp. 1515-1525.

DEGROOTE, J., HAELTERMAN, R., ANNEREL, S., BRUGGEMAN, P. and VIERENDEELS, J., 2010. Performance of partitioned procedures in fluid–structure interaction. *Computers & Structures,* **88**(7), pp. 446-457.

DEMIRDZIC, I.A., 1982. *A finite volume method for computation of fluid flow in complex geometries.*

DEN HARTOG, J., 1932. Transmission line vibration due to sleet. *Transactions of the American Institute of Electrical Engineers,* **4**(51), pp. 1074-1076.

DRIKAKIS, D. and RIDER, W., 2006. *High-resolution methods for incompressible and low-speed flows.* Springer Science & Business Media.

EDMANS, B., 2013. *Non-linear finite element analysis of flexible pipes for deep-water applications,* .

EISNER, F., 1925. Pressure measurements on cylinder surrounded by flowing fluid. *Z.Angew.Math.Mech,* **5**, pp. 486-489.

FAGE, A. and JOHANSEN, F., 1928. XLII. The structure of vortex sheets. *The London, Edinburgh, and Dublin Philosophical Magazine and Journal of Science,* **5**(28), pp. 417-441.

FELIPPA, C.A., PARK, K. and FARHAT, C., 2001. Partitioned analysis of coupled mechanical systems. *Computer Methods in Applied Mechanics and Engineering,* **190**(24), pp. 3247-3270.

FENG, C., 1968. *The measurement of vortex induced effects in flow,* University of British Columbia.

FERGUSON, N. and PARKINSON, G., 1967. Surface and wake flow phenomena of the vortex-excited oscillation of a circular cylinder. *Journal of Engineering for Industry,* **89**(4), pp. 831-838.

FERGUSON, N., 1965. *The measurement of wake and surface effects in the subcritical flow past a circular cylinder at rest and in vortex-excited oscillation,* .

FERNANDES, A., MIRZAEISEFAT, S. and CASCÃO, L., 2014. Fundamental behavior of vortex self induced vibration (VSIV). *Applied Ocean Research,* **47**, pp. 183-191.

FERZIGER, J.H. and PERIC, M., 2012. *Computational methods for fluid dynamics.* Springer Science & Business Media.

GABBAI, R. and BENAROYA, H., 2005. An overview of modeling and experiments of vortex-induced vibration of circular cylinders. *Journal of Sound and Vibration,* **282**(3), pp. 575-616.

GE, L. and SOTIROPOULOS, F., 2007. A numerical method for solving the 3D unsteady incompressible Navier-Stokes equations in curvilinear domains with complex immersed boundaries. *Journal of Computational Physics,* **225**(2), pp. 1782-1809.

GERRARD, J., 1978. The wakes of cylindrical bluff bodies at low Reynolds number. *Philosophical Transactions of the Royal Society of London A: Mathematical, Physical and Engineering Sciences,* **288**(1354), pp. 351-382.

GERRARD, J., 1966. The mechanics of the formation region of vortices behind bluff bodies. *Journal of Fluid Mechanics,* **25**(02), pp. 401-413.

GOUD, T.S.K., KUMAR, A.S. and PRASAD, S.S., 2014. Analysis of Fluid-Structure Interaction on an Aircraft Wing. *Analysis,* **3**(9), pp. 146-152.

GOVARDHAN, R. and WILLIAMSON, C., 2000. Modes of vortex formation and frequency response of a freely vibrating cylinder. *Journal of Fluid Mechanics,* **420**, pp. 85-130.

GOVARDHAN, R. and WILLIAMSON, C., 2006. Defining the 'modified Griffin plot'in vortex-induced vibration: revealing the effect of Reynolds number using controlled damping. *Journal of Fluid Mechanics,* **561**, pp. 147-180.

GREEN, R. and GERRARD, J., 1993. Vorticity measurements in the near wake of a circular cylinder at low Reynolds numbers. *Journal of Fluid Mechanics,* **246**, pp. 675-691.

GRIFFIN, O., 1980. Vortex-excited cross-flow vibrations of a single cylindrical tube. *Journal of Pressure Vessel Technology,* **102**(2), pp. 158-166.

GRIFFIN, O.M., 1971. The unsteady wake of an oscillating cylinder at low Reynolds number. *Journal of Applied Mechanics,* **38**(4), pp. 729-738.

GRIFFIN, O.M. and RAMBERG, S.E., 1976. Vortex shedding from a cylinder vibrating in line with an incident uniform flow. *Journal of Fluid Mechanics,* **75**(02), pp. 257-271.

GRIFFIN, O.M. and RAMBERG, S.E., 1974. The vortex-street wakes of vibrating cylinders. *Journal of Fluid Mechanics,* **66**(03), pp. 553-576.

GRIFFIN, O.M. and VOTAW, C.W., 1972. The vortex street in the wake of a vibrating cylinder. *Journal of Fluid Mechanics,* **55**(1), pp. 31-48.

GROVE, A.S., SHAIR, F. and PETERSEN, E., 1964. An experimental investigation of the steady separated flow past a circular cylinder. *Journal of Fluid Mechanics,* **19**(01), pp. 60-80.

GSELL, S., BOURGUET, R. and BRAZA, M., 2017. Vortex-induced vibrations of a cylinder in planar shear flow. *Journal of Fluid Mechanics,* **825**, pp. 353-384.

GU, W., CHYU, C. and ROCKWELL, D., 1994. Timing of vortex formation from an oscillating cylinder. *Physics of Fluids (1994-present),* **6**(11), pp. 3677-3682.

GUILMINEAU, E. and QUEUTEY, P., 2002. A numerical simulation of vortex shedding from an oscillating circular cylinder. *Journal of Fluids and Structures,* **16**(6), pp. 773-794.

HAMA, F., 1957. 3-DIMENSIONAL VORTEX PATTERN BEHIND A CIRCULAR CYLINDER. *Journal of the Aeronautical Sciences,* **24**(2), pp. 156-158.

HARTLEN, R.T. and CURRIE, I.G., 1970. Lift-oscillator model of vortex-induced vibration. *Journal of the Engineering Mechanics Division,* **96**(5), pp. 577-591.

HENDERSON, R.D., 1995. Details of the drag curve near the onset of vortex shedding. *Physics of Fluids (1994-present),* **7**(9), pp. 2102-2104.

HOMANN, F., 1936. Der Einfluss grosser Zähigkeit bei der Strömung um den Zylinder und um die Kugel. *ZAMM-Journal of Applied Mathematics and Mechanics/Zeitschrift für Angewandte Mathematik und Mechanik,* **16**(3), pp. 153-164.

HONJI, H. and TANEDA, S., 1968. Vortex wakes of oscillating circular cylinders(Vortex wakes behind circular cylinder subject to transverse sinusoidal oscillations in uniform water flow at specific Reynolds numbers, photographing varied frequency flow patterns). *KYUSHU UNIVERSITY, RESEARCH INST.FOR APPLIED MECHANICS, REPORTS*, **16**(54), pp. 211-222.

HOVER, F., TECHET, A. and TRIANTAFYLLOU, M., 1998. Forces on oscillating uniform and tapered cylinders in cross flow. *Journal of Fluid Mechanics*, **363**, pp. 97-114.

HOWE, M., 1989. On unsteady surface forces, and sound produced by the normal chopping of a rectilinear vortex. *Journal of Fluid Mechanics*, **206**, pp. 131-153.

HUANG, K., CHEN, H. and CHEN, C., 2012. Vertical riser VIV simulation in sheared current. *International Journal of Offshore and Polar Engineering*, **22**(02),.

JEON, D. and GHARIB, M., 2001. On circular cylinders undergoing two-degree-of-freedom forced motions. *Journal of Fluids and Structures*, **15**(3), pp. 533-541.

KANG, S., 2006. Uniform-shear flow over a circular cylinder at low Reynolds numbers. *Journal of Fluids and Structures*, **22**(4), pp. 541-555.

KARANTH, D., RANKIN, G. and SRIDHAR, K., 1995. Computational study of flow past a cylinder with combined in-line and transverse oscillation. *Computational Mechanics*, **16**(1), pp. 1-10.

KARNIADAKIS, G.E. and TRIANTAFYLLOU, G.S., 1989. Frequency selection and asymptotic states in laminar wakes. *Journal of Fluid Mechanics*, **199**, pp. 441-469.

KELES, R.S., 2015. Active control of vortex shedding in the far wake of a cylinder. *Astron Space Sci*, **1**(001),.

KHALAK, A. and WILLIAMSON, C., 1999. Motions, forces and mode transitions in vortex-induced vibrations at low mass-damping. *Journal of Fluids and Structures*, **13**(7), pp. 813-851.

KHALAK, A. and WILLIAMSON, C., 1996. Dynamics of a hydroelastic cylinder with very low mass and damping. *Journal of Fluids and Structures*, **10**(5), pp. 455-472.

KING, R., PROSSER, M. and JOHNS, D., 1973. On vortex excitation of model piles in water. *Journal of Sound and Vibration*, **29**(2), pp. 169IN1-188IN2.

KING, R., 1977. A review of vortex shedding research and its application. *Ocean Engineering,* **4**(3), pp. 141-171.

KLAMO, J., LEONARD, A. and ROSHKO, A., 2005. On the maximum amplitude for a freely vibrating cylinder in cross-flow. *Journal of Fluids and Structures,* **21**(4), pp. 429-434.

KOOPMANN, G., 1967. The vortex wakes of vibrating cylinders at low Reynolds numbers. *Journal of Fluid Mechanics,* **28**(03), pp. 501-512.

KOSS, L. and MELBOURNE, W., 1995. Chain dampers for control of wind-induced vibration of tower and mast structures. *Engineering Structures,* **17**(9), pp. 622-625.

KOVASZNAY, L., 1949. Hot-wire investigation of the wake behind cylinders at low Reynolds numbers, *Proceedings of the Royal Society of London A: Mathematical, Physical and Engineering Sciences* 1949, The Royal Society, pp. 174-190.

KRAVCHENKO, A.G., MOIN, P. and SHARIFF, K., 1999. B-spline method and zonal grids for simulations of complex turbulent flows. *Journal of Computational Physics,* **151**(2), pp. 757-789.

KUMAR, B. and MITTAL, S., 2006. Effect of blockage on critical parameters for flow past a circular cylinder. *International Journal for Numerical Methods in Fluids,* **50**(8), pp. 987-1001.

LAM, K. and LIU, P., 2013. A circular cylinder undergoing large-amplitude transverse oscillations in a slow uniform cross flow. *Journal of Fluids and Structures,* **39**, pp. 408-417.

LE CUNFF, C., BIOLLEY, F., FONTAINE, E., ETIENNE, S. and FACCHINETTI, M., 2002. Vortex-induced vibrations of risers: theoretical, numerical and experimental investigation. *Oil & Gas Science and Technology,* **57**(1), pp. 59-69.

LE TALLEC, P. and MOURO, J., 2001. Fluid structure interaction with large structural displacements. *Computer Methods in Applied Mechanics and Engineering,* **190**(24), pp. 3039-3067.

LEONTINI, J.S., STEWART, B.E., THOMPSON, M.C. and HOURIGAN, K., 2006. Predicting vortex-induced vibration from driven oscillation results. *Applied Mathematical Modelling,* **30**(10), pp. 1096-1102.

LI, L., SHERWIN, S. and BEARMAN, P.W., 2002. A moving frame of reference algorithm for fluid/structure interaction of rotating and translating bodies. *International Journal for Numerical Methods in Fluids,* **38**(2), pp. 187-206.

LI, Y., ZHANG, R., SHOCK, R. and CHEN, H., 2009. Prediction of vortex shedding from a circular cylinder using a volumetric Lattice-Boltzmann boundary approach. *The European Physical Journal Special Topics,* **171**(1), pp. 91-97.

LIGHTHILL, J., 1986. Fundamentals concerning wave loading on offshore structures. *Journal of Fluid Mechanics,* **173**, pp. 667-681.

LINKE, W., 1931. New measurements on aerodynamics of cylinders particularly their friction resistance. *Phys.Z,* **32**, pp. 900.

LIU, L., FENG, J., WU, H., XU, W. and TAN, W., 2017. Fluid Excitation Forces on a Tightly Packed Tube Bundle Subjected in Cross-Flow. *Journal of Pressure Vessel Technology,* **139**(3), pp. 031307.

LOISEAU, H. and SZECHENYI, E., 1974. Dynamic lift on a cylinder in high reynolds number flow. *Flow Induced Structural Vibrations,* , pp. 755-761.

LU, X. and DALTON, C., 1996. Calculation of the timing of vortex formation from an oscillating cylinder. *Journal of Fluids and Structures,* **10**(5), pp. 527-541.

LUCOR, D., IMAS, L. and KARNIADAKIS, G.E., 2001. Vortex dislocations and force distribution of long flexible cylinders subjected to sheared flows. *Journal of Fluids and Structures,* **15**(3-4), pp. 641-650.

MADANIKERMANI, S., 2014. *Application of immersed boundary method to rlexible riser problem,* .

MITTAL, S. and SINGH, S., 2005. Vortex-induced vibrations at subcritical Re. *Journal of Fluid Mechanics,* **534**, pp. 185-194.

MOHAMMADI, H., CARTIER, R. and MONGRAIN, R., 2016. Review of numerical methods for simulation of the aortic root: Present and future directions. *International Journal for Computational Methods in Engineering Science and Mechanics,* **17**(3), pp. 182-195.

MORISON, J., JOHNSON, J. and SCHAAF, S., 1950. The force exerted by surface waves on piles. *Journal of Petroleum Technology,* **2**(05), pp. 149-154.

MORSE, T.L., 2009. *Investigating phenomena in vortex-induced vibration of a cylinder using controlled vibration,* .

MORSE, T. and WILLIAMSON, C., 2009. Fluid forcing, wake modes, and transitions for a cylinder undergoing controlled oscillations. *Journal of Fluids and Structures,* **25**(4), pp. 697-712.

MORSE, T.L. and WILLIAMSON, C.H.K., 2006. Employing controlled vibrations to predict fluid forces on a cylinder undergoing vortex-induced vibration. *Journal of Fluids and Structures,* **22**(6-7), pp. 877-884.

NAUDASCHER, E., 1987. Flow-induced streamwise vibrations of structures. *Journal of Fluids and Structures,* **1**(3), pp. 265-298.

NAUDASCHER, E. and ROCKWELL, D., 2012. *Flow-induced vibrations: an engineering guide.* Courier Corporation.

NISHIOKA, M. and SATO, H., 1978. Mechanism of determination of the shedding frequency of vortices behind a cylinder at low Reynolds numbers. *Journal of Fluid Mechanics,* **89**(1), pp. 49-60.

NOBARI, M. and NADERAN, H., 2006. A numerical study of flow past a cylinder with cross flow and inline oscillation. *Computers & Fluids,* **35**(4), pp. 393-415.

NORBERG, C., 1994. An experimental investigation of the flow around a circular cylinder: influence of aspect ratio. *Journal of Fluid Mechanics,* **258**, pp. 287-316.

NORBERG, C., 2003. Fluctuating lift on a circular cylinder: review and new measurements. *Journal of Fluids and Structures,* **17**(1), pp. 57-96.

ONGOREN, A. and ROCKWELL, D., 1988. Flow structure from an oscillating cylinder Part 1. Mechanisms of phase shift and recovery in the near wake. *Journal of Fluid Mechanics,* **191**, pp. 197-223.

OSTASEVICIUS, V., JURENAS, V., BALEVICIUS, G., ZUKAUSKAS, M. and UBARTAS, M., 2015. Vibrational excitation of a work piece for drilling force reduction in brittle materials. *Mechanics,* **20**(6), pp. 596-601.

PARK, J., KWON, K. and CHOI, H., 1998. Numerical solutions of flow past a circular cylinder at Reynolds numbers up to 160. *KSME international Journal,* **12**(6), pp. 1200-1205.

PARKINSON, G., 1989. Phenomena and modelling of flow-induced vibrations of bluff bodies. *Progress in Aerospace Sciences,* **26**(2), pp. 169-224.

PATANKAR, S.V. and SPALDING, D.B., 1972. A calculation procedure for heat, mass and momentum transfer in three-dimensional parabolic flows. *International Journal of Heat and Mass Transfer,* **15**(10), pp. 1787-1806.

PAULEY, L.L., MOIN, P. and REYNOLDS, W.C., 1990. The structure of two-dimensional separation. *Journal of Fluid Mechanics,* **220**, pp. 397-411.

PEARSON, J. and PETRIE, C., 1965. On the melt-flow instability of extruded polymers.

PEPPA, S., KAIKTSIS, L., FROUZAKIS, C. and TRIANTAFYLLOU, G., 2015. A Comparison of Forces in Two-and Three-Dimensional Flow Past an Oscillating Cylinder, *ASME 2015 Pressure Vessels and Piping Conference* 2015, American Society of Mechanical Engineers, pp. V004T04A032-V004T04A032.

PERSILLON, H. and BRAZA, M., 1998. Physical analysis of the transition to turbulence in the wake of a circular cylinder by three-dimensional Navier–Stokes simulation. *Journal of Fluid Mechanics,* **365**, pp. 23-88.

PHILLIPS, O.M., 1956. The intnesity of Aeolian tones. *Journal of Fluid Mechanics,* **1**(6), pp. 607-624.

PONTA, F.L. and AREF, H., 2005. Vortex synchronization regions in shedding from an oscillating cylinder. *Physics of Fluids (1994-present),* **17**(1), pp. 011703-011703-4.

POSDZIECH, O. and GRUNDMANN, R., 2007. A systematic approach to the numerical calculation of fundamental quantities of the two-dimensional flow over a circular cylinder. *Journal of Fluids and Structures,* **23**(3), pp. 479-499.

PRANDTL, L., 1961. Collected Works. *Tollmien, W., Schlicting, H., Go rtler, H.(Eds.).Springer, Berlin,* .

QU, L., NORBERG, C., DAVIDSON, L., PENG, S. and WANG, F., 2013. Quantitative numerical analysis of flow past a circular cylinder at Reynolds number between 50 and 200. *Journal of Fluids and Structures,* **39**, pp. 347-370.

RAJANI, B., KANDASAMY, A. and MAJUMDAR, S., 2009. Numerical simulation of laminar flow past a circular cylinder. *Applied Mathematical Modelling,* **33**(3), pp. 1228-1247.

RAYLEIGH, L., 1915. XLVIII. Æolian tones. *The London, Edinburgh, and Dublin Philosophical Magazine and Journal of Science,* **29**(172), pp. 433-444.

RELF, E. and SIMMONS, L., 1924. The Frequency of Eddies Generated by the Motion of Circular Cylinders through* a Fluid. R. & M. 917. *British ARC, June,* .

RICHARDSON, S., 1973. On the no-slip boundary condition. *Journal of Fluid Mechanics,* **59**(4), pp. 707-719.

ROSHKO, A., 1961. Experiments on the flow past a circular cylinder at very high Reynolds number. *Journal of Fluid Mechanics,* **10**(03), pp. 345-356.

ROSHKO, A., 1954. On the development of turbulent wakes from vortex streets.

ROUSSOPOULOS, K., 1993. Feedback control of vortex shedding at low Reynolds numbers. *Journal of Fluid Mechanics,* **248**, pp. 267-296.

SAINSBURY, R. and KING, D., 1971. THE FLOW INDUCED OSCILLATION OF MARINE STRUCTURES. *Proceedings of the Institution of Civil Engineers,* **49**(3), pp. 269-302.

SARPKAYA, T., 2004. A critical review of the intrinsic nature of vortex-induced vibrations. *Journal of Fluids and Structures,* **19**(4), pp. 389-447.

SARPKAYA, T., 2001. On the force decompositions of Lighthill and Morison. *Journal of Fluids and Structures,* **15**(2), pp. 227-233.

SCHAEFER, J.W. and ESKINAZI, S., 1959. An analysis of the vortex street generated in a viscous fluid. *Journal of Fluid Mechanics,* **6**(02), pp. 241-260.

SCHEWE, G., 1983. On the force fluctuations acting on a circular cylinder in crossflow from subcritical up to transcritical Reynolds numbers. *Journal of Fluid Mechanics,* **133**, pp. 265-285.

SCHLICHTING, H. and GERSTEN, K., 2003. *Boundary-layer theory*. Springer Science & Business Media.

SCRUTON, C. and FLINT, A.R., 1964. WIND-EXCITED OSCILLATIONS OF STRUCTURES. *Proceedings of the Institution of Civil Engineers,* **27**(4), pp. 673-702.

SENGUPTA, P., LOW, Y.M., ZHANG, X., ADAIKALARAJ, P.F.B. and KOH, C.G., 2016. Reliability Assessment of Marine Drilling Risers With Correlated Random Variables, *ASME 2016 35th International Conference on Ocean, Offshore and Arctic Engineering* 2016, American Society of Mechanical Engineers, pp. V003T02A055-V003T02A055.

SHI, J., GERLACH, D., BREUER, M., BISWAS, G. and DURST, F., 2004. Heating effect on steady and unsteady horizontal laminar flow of air past a circular cylinder. *Physics of Fluids (1994-present),* **16**(12), pp. 4331-4345.

SIDARTA, D.E., LAMBRAKOS, K.F., THOMPSON, H.M. and BURKE, R.W., 2006. A methodology for in-line VIV analysis of risers in sheared currents, *25th International Conference on Offshore Mechanics and Arctic Engineering* 2006, American Society of Mechanical Engineers, pp. 819-827.

SINGHA, S. and SINHAMAHAPATRA, K., 2010. Flow past a circular cylinder between parallel walls at low Reynolds numbers. *Ocean Engineering,* **37**(8), pp. 757-769.

SKOP, R. and BALASUBRAMANIAN, S., 1997. A new twist on an old model for vortex-excited vibrations. *Journal of Fluids and Structures,* **11**(4), pp. 395-412.

SLAOUTI, A. and GERRARD, J., 1981. An experimental investigation of the end effects on the wake of a circular cylinder towed through water at low Reynolds numbers. *Journal of Fluid Mechanics,* **112**, pp. 297-314.

SRINIL, N. and ZANGANEH, H., 2012. Modelling of coupled cross-flow/in-line vortex-induced vibrations using double Duffing and van der Pol oscillators. *Ocean Engineering,* **53**, pp. 83-97.

STÅLBERG, E., BRÜGER, A., LÖTSTEDT, P., JOHANSSON, A.V. and HENNINGSON, D.S., 2006. High order accurate solution of flow past a circular cylinder. *Journal of Scientific Computing,* **27**(1-3), pp. 431-441.

STAUBLI, T., 1983. Calculation of the vibration of an elastically mounted cylinder using experimental data from forced oscillation. *Journal of Fluids Engineering,* **105**(2), pp. 225-229.

STEWART, B., LEONTINI, J., HOURIGAN, K. and THOMPSON, M., 2005. A numerical survey of wake modes and energy transfers for an oscillating cylinder at Re= 200, *Fourth Symposium on Bluff Body Wakes and Vortex-Induced Vibrations, Greece (ed. T. Leweke & CHK Williamson)* 2005, Citeseer, pp. 239-242.

STROUHAL, V., 1878. Über eine besondere Art der Tonerregung. *Annalen der Physik,* **241**(10), pp. 216-251.

TANG, G., LU, L., ZHAO, M., LIU, M. and ZONG, Z., 2016. Phase jump and energy transfer of forced oscillating circular cylinder in uniform flow. *Proceedings of the Institution of Mechanical*

Engineers, Part M: Journal of Engineering for the Maritime Environment, , pp. 1475090216656950.

TANIDA, Y., OKAJIMA, A. and WATANABE, Y., 1973. Stability of a circular cylinder oscillating in uniform flow or in a wake. *Journal of Fluid Mechanics,* **61**(04), pp. 769-784.

THOM, A., 1933. The flow past circular cylinders at low speeds. *Proceedings of the Royal Society of London.Series A, Containing Papers of a Mathematical and Physical Character,* **141**(845), pp. 651-669.

TOEBES, G.H., 1968. The unsteady flow and wake near an oscillating cylinder, 1968, ASME.

TRITTON, D., 1959. Experiments on the flow past a circular cylinder at low Reynolds numbers. *Journal of Fluid Mechanics,* **6**(04), pp. 547-567.

TROESCH, A. and KIM, S., 1991. Hydrodynamic forces acting on cylinders oscillating at small amplitudes. *Journal of Fluids and Structures,* **5**(1), pp. 113-126.

TROPEA, C., YARIN, A.L. and FOSS, J.F., 2007. *Springer handbook of experimental fluid mechanics.* Springer Science & Business Media.

TSUI, Y., 1982. Recent advances in engineering science as applied to aeolian vibration: an alternative approach. *Electric Power Systems Research,* **5**(1), pp. 73-85.

TUDBALL-SMITH, D., LEONTINI, J.S., SHERIDAN, J. and JACONO, D.L., 2012. Streamwise forced oscillations of circular and square cylinders. *Physics of Fluids (1994-present),* **24**(11), pp. 111703.

VAN DYKE, M., 1982. *An album of fluid motion.* Parabolic Press Stanford.

VANDIVER J.K. and JONG J.-Y., 1987. The relationship between in-line and cross-flow vortex-induced vibration of cylinders. *Journal of Fluids and Structures,* **1**(4), pp. 381-399.

VANDIVER, J.K., 2012. Damping parameters for flow-induced vibration. *Journal of Fluids and Structures,* **35**, pp. 105-119.

VON KARMAN, T., 1911. Über den Mechanismus des Widerstandes, den ein bewegter Körper in einer Flüssigkeit erfährt. *Nachrichten von der Gesellschaft der Wissenschaften zu Göttingen, Mathematisch-Physikalische Klasse,* **1911**, pp. 509-517.

WEHRMANN, O., 1965. Reduction of Velocity Fluctuations in a K· rm· n Vortex Street by a Vibrating Cylinder. *Physics of Fluids (1958-1988),* **8**(4), pp. 760-761.

WILLIAMSON, C.H., 2011. *Vortex-Induced Vibration: Universal Phenomena in Diverse VIV Systems,* .

WILLIAMSON, C., 1989. Oblique and parallel modes of vortex shedding in the wake of a circular cylinder at low Reynolds numbers. *Journal of Fluid Mechanics,* **206**, pp. 579-627.

WILLIAMSON, C. and BROWN, G., 1998. A series in 1/√ Re to represent the Strouhal–Reynolds number relationship of the cylinder wake. *Journal of Fluids and Structures,* **12**(8), pp. 1073-1085.

WILLIAMSON, C. and GOVARDHAN, R., 2008. A brief review of recent results in vortex-induced vibrations. *Journal of Wind Engineering and Industrial Aerodynamics,* **96**(6), pp. 713-735.

WILLIAMSON, C. and ROSHKO, A., 1990. Measurements of base pressure in the wake of a cylinder at low Reynolds numbers. *Zeitschrift fur Flugwissenschaften und Weltraumforschung,* **14**, pp. 38-46.

WILLIAMSON, C.H.K. and ROSHKO, A., 1988. *Vortex formation in the wake of an oscillating cylinder.*

WONG, H. and HEATHCOCK, C., 1985. Design against wind-induced vibration of multi-flue chimney stacks. *Engineering Structures,* **7**(1), pp. 2-9.

WOOTON, L., WARNER, M., SAINSBURY, R. and COOPER, D., 1972. Oscillations of piles in marine structures. A resume of full-scale experiments at Immingham. *Construction Industry Research and Information Association (CIRIA).*

WU, J.C., 1981. Theory for Aerodynamic Force and Moment in Viscous Flows. **04**(01), pp. 432-441.

WU, M., WEN, C., YEN, R., WENG, M. and WANG, A., 2004. Experimental and numerical study of the separation angle for flow around a circular cylinder at low Reynolds number. *Journal of Fluid Mechanics,* **515**, pp. 233-260.

ZDRAVKOVICH, M., 1997. Flow around Circular Cylinders; Vol. I Fundamentals. *Journal of Fluid Mechanics,* **350**(1), pp. 377-378.

ZDRAVKOVICH, M., 1982. Modification of vortex shedding in the synchronization range. *Journal of Fluids Engineering*, **104**(4), pp. 513-517.